Eberhard Karls University of Tübingen

Department of Geoscience

Institute of Geography

# Assessment of agricultural drought over Africa and its relation to El Niño–Southern Oscillation using remote sensing-based time series

Thesis

submitted in partial fulfilment of the degree requirements

**Master of Science**

*Author:*

Karina Winkler

Matriculation Nr. 3903638

*Supervisors:*

Prof. Dr. Volker Hochschild

Physical Geography/ Geoinformatics,
Department of Geoscience,
University of Tübingen

Dr. Ursula Geßner

German Remote Sensing Data Center (DFD),
German Aerospace Center (DLR)

31st January 2017

# Abstract

Ranked amongst the most destructive natural disasters of the world, droughts may have severe impacts on ecosystems and society. Particularly in Africa, where water is a limiting factor and countries strongly rely on rain-fed agriculture, droughts have constantly led to widespread crop failure, food shortages and even humanitarian crises. In regions over eastern and southern Africa, such dry conditions have been attributed to the effect of El Niño–Southern Oscillation (ENSO). Given the recent El Niño episode of 2015/16 and the associated severe droughts that occurred in many parts of Africa, this interconnection has once again become an issue of importance. In this regard, remote sensing data and image analysis provide new opportunities for generating substantial information on the evolution of droughts at large spatial and temporal scales.

This thesis focusses on monitoring agricultural droughts over Africa during 2000-2016 and their relation to ENSO by means of remote sensing time series. The used continental-scale approach is based on drought indices. In particular, TRMM-based Standardized Precipitation Index (SPI) and MODIS-derived Vegetation Condition Index (VCI) were used for analysing the spatio-temporal patterns of agricultural droughts. All in all, a comprehensive insight into the evolution of agricultural droughts in Africa was gained. The applicability of SPI and VCI as indices for continental-scale drought monitoring was proven. Observed discrepancies were linked with variabilities in sensitivity of vegetation to rainfall over Africa, which in turn merits further research. Moreover, the relation between droughts and ENSO was examined by applying a correlation analysis between time series of drought indices and Multivariate ENSO Index (MEI). This complex relationship could be described in its fundamentals. Based on revealed correlation patterns, droughts tend to occur during El Niño over large parts of southern Africa. In contrast, a divided pattern was observed in eastern Africa, where areas with bimodal annual rainfall cycles tend to be affected by droughts during La Niña and, in zones of unimodal rainfall regimes, droughts tend to arise during the onset of El Niño. However, no universal El Niño- or La Niña-related response pattern of droughts could be deduced. In this regard, multi-year atmospheric fluctuations and characteristics of ENSO variants were discussed as possible influencing factors. Regional impacts of the drought episodes during El Niño 2002/03 and La Niña 2010/11 were illuminated by comparing observed regional drought patterns with statistics on national crop production. Focus is laid on each southern and eastern Africa, where decreases in production numbers were observed for major drought-affected countries.

In order to achieve improvements in quality and reliability of the output, the incorporation of more accurate cropland information, adaptions of the correlation analysis as well as an uncertainty assessment and a validation are proposed. Using remote sensing data as a toolset for drought monitoring, this thesis represents an attempt to contribute to a better understanding of spatio-temporal patterns of agricultural droughts in Africa and their dependencies. Such knowledge is essential as it forms the basis for implementing strategies of drought hazard mitigation in the affected regions.

# Contents

# List of Acronyms

| | |
|---|---|
| **AFDM** | African Flood and Drought Monitor |
| **AVHRR** | Advanced Very-High-Resolution Radiometer |
| **CDF** | Cumulative density function |
| **CMI** | Crop Moisture Index |
| **CMDI** | Soil Moisture Deficit Index |
| **CSDI** | Crop Specific Drought Index |
| **DOY** | Day Of Year |
| **EDO** | European Drought Observatory |
| **EDI** | Effective Drought Index |
| **ENSO** | El Niño–Southern Oscillation |
| **EOS** | End Of Season |
| **EVI** | Enhanced Vegetation Index |
| **FAO** | Food and Agricultural Organization of the United Nations |
| **FEWS NET** | Famine Early Warning Systems Network |
| **GADM** | Global Administrative Areas |
| **GADMFS** | Global Agricultural Drought Monitoring and Forecasting System |
| **GDAL** | Geospatial Data Abstraction Library |
| **GIS** | Geographic Information System |
| **GIDMaPS** | Global Integrated Monitoring and Prediction System |
| **GPCC** | Global Precipitation Climatology Center |
| **HDF** | Hierarchical Data Format |
| **IDL** | Interactive Data Language |
| **ITCZ** | Intertropical Convergence Zone |
| **LST** | Land Surface Temperature |
| **MEI** | Multivariate ENSO Index |
| **MODIS** | Moderate-resolution Imaging Spectroradiometer |
| **NASA** | National Aeronautics and Space Administration |
| **NDWI** | Normalized Difference Water Index |
| **NDVI** | Normalized Difference Vegetation Index |

| | |
|---|---|
| **NIR** | Near infrared |
| **NASDA** | National Space Development Agency |
| **netCDF** | Network Common Data Format |
| **OLR** | Outgoing Longwave Radiation |
| **ONI** | Oceanic Niño Index |
| **PCA** | Principal Components Analysis |
| **PDI** | Perpendicular Drought Index |
| **PDSI** | Palmer Drought Severity Index |
| **PHDI** | Palmer Hydrological Drought Index |
| **RAI** | Rainfall Anomaly Index |
| **RDI** | Reconnaissance Drought Index |
| **RED** | Visible red |
| **RSDI** | Regional Streamflow Deficiency Index |
| **RSR** | Relative Spectral Responses |
| **SPOT** | Satellite Pour l'Observation de la Terre |
| **SAVI** | Soil-Adjusted Vegetation Index |
| **SMA** | Soil Moisture Anomaly |
| **SMDI** | Soil Moisture Deficit Index |
| **SOI** | Southern Oscillation Index |
| **SOS** | Start Of Season |
| **SPEI** | Standardized Precipitation Evapotranspiration Index |
| **SPI** | Standardized Precipitation Index |
| **SST** | Sea Surface Temperatures |
| **SWIR** | Short-wave infrared |
| **SWSI** | Surface Water Supply Index |
| **TCI** | Temperature Condition Index |
| **TIR** | Thermal infrared |
| **TMPA** | TRMM Multisatellite Precipitation Analysis |
| **TRMM** | Tropical Rainfall Measuring Mission |
| **USAID** | U.S. Agency for International Development |
| **USDM** | U. S. Drought Monitor |
| **VCI** | Vegetation Condition Index |
| **VHI** | Vegetation Health Index |
| **VIRS** | Visible and Infrared Radiometer System |
| **VPI** | Vegetation Productivity Index |
| **WMO** | World Meteorological Organization |
| **WRB** | World Reference Base for Soil Resources |

# List of Figures

# List of Tables

# Chapter 1

# Introduction

## 1.1 Motivation and research questions

Droughts are amongst the most destructive natural hazards and can arise virtually everywhere on the globe (Schubert et al., 2016). These periods of abnormally dry conditions can affect both ecosystems and society in multiple ways. On the one hand, droughts are main drivers for land degradation and desertification. On the other hand, socio-economic impacts of droughts may involve deaths, crop failure, food shortages, famine, malnutrition and mass migration (Masih et al., 2014). In regard to a growing population and the ongoing climate change, water and food security are major challenges facing humanity (Hao et al., 2014).

In many regions, observed recurrent droughts are linked with the phenomenon of El Niño–Southern Oscillation (ENSO) in the tropical Pacific, since the involved interplay of atmospheric and oceanic circulation leads to regional precipitation and temperature anomalies around the globe (Propastin et al., 2010). In this context, ENSO is related with regional rainfall variability and associated droughts over large parts of the African continent.

In general, Africa is the hottest and most water-scarce continent on earth (Gan et al., 2016). With rainfall as the limiting factor for farming and many countries strongly relying on rain-fed agriculture, droughts affect not only natural ecosystems but also crop production and food supply and, thus, may have severe socio-economic impacts (Rosenzweig and Hillel, 2008). Droughts have become and are likely to remain an increasing threat to many African countries. In total, drought events have caused more than 800,000 deaths and affected about 262 million people in Africa during 1900-2013 (Guha-Sapir et al., 2016). Regarding the recent El Niño episode of 2015/16, one of the strongest events of the recorded history, and its devastating effects on agriculture and food security over large parts of Africa (FAO, 2016a), understanding and monitoring the effects of ENSO on regional rainfall patterns and vegetation condition are of major concern for implementing measures of early warning and adaption to drought hazards. This has become more important than ever, especially when agricultural crop failure threatens food security and may lead to famine and economic crises.

In this connection, remote sensing data and methods are critical tools for studying the spatio-temporal evolution and the underlying drivers of droughts. In particular, earth observation

provides the unique opportunity to obtain continuous, consistent and timely information over large areas where ground observations are unreliable. With recent advances in techniques and an increased data availability, remote sensing-based time series analysis is highly relevant for environmental monitoring (Eerens et al., 2014; Meroni et al., 2014).

This thesis focuses on the detection of agricultural droughts over Africa and the analysis of the associated relation to ENSO by means of remote sensing time series for the period of 2000-2016. This continental-scale approach is based on drought indices derived from remotely sensed data. In particular, Tropical Rainfall Measuring Mission (TRMM) precipitation estimates are used for calculating the Standardized Precipitation Index (SPI) as a first drought index. Secondly, Moderate-resolution Imaging Spectroradiometer (MODIS) images of surface reflectance are utilized to derive the Vegetation Condition Index (VCI). Both drought indices are used in order to analyse the spatio-temporal pattern of agricultural droughts. Through index-based time series analyses, the thesis at hand addresses the following research questions:

- When and where were agricultural areas in Africa mainly affected by droughts during the growing seasons from 2000 to 2016?

- Where and how are observed agricultural droughts in Africa related to ENSO? Which spatio-temporal patterns can be revealed from responses of rainfall- and vegetation-related droughts to ENSO events?

- What is the impact of observed ENSO-related droughts on agricultural production in the two particularly affected regions of eastern and southern Africa?

The thesis aims to give an insight into the spatio-temporal evolution of agricultural droughts over Africa during the study period. It intends to contribute to a better understanding of the interconnection between ENSO and regional drought patterns. This in turn can provide the basis for implementing strategies and building capacities in order to cope with drought-related challenges in the affected regions.

## 1.2 Thesis framework

Firstly, the underlying theory of this thesis is illuminated in chapter 2. This involves drought in its concept and typology as well as the fundamentals of ENSO. Additionally, an overview on state-of-the-art drought and ENSO indices is given. Recent remote sensing-based studies of drought monitoring and research on the relation between ENSO and droughts in Africa are reviewed. Following a brief description of the characteristics of the study area in chapter 3, data and methods used in this thesis are described in chapter 4. Here, workflows are presented for the derivation of indices, drought detection and correlation analysis. Subsequently, the results of the thesis are shown in chapter 5, including the spatio-temporal pattern of droughts in Africa, their relation to ENSO as well as the regional impacts of selected drought years on agricultural production. The major findings are discussed in chapter 6, in which focus is laid on the integration of the results in scientific research. Further, potential and limitations of this work are outlined. Lastly, concluding remarks are given (see chapter 7).

# Chapter 2

# Theoretical background

## 2.1 Drought

### 2.1.1 Concept and influencing factors

Perceived as a natural disaster, droughts are characterized as an extreme climate feature triggered by below-normal precipitation during a period of several months to years. They are defined as dry temporal aberrations in relation to the normal local condition. Droughts are featured by a slow onset, while associated effects may accumulate over a considerable time span and affect various economic sectors depending on water. In particular, no single, universally accepted definition of drought exists, which constrains the identification of key characteristics like duration, severity, and spatial extent (Dai, 2011; Hayes et al., 2012; Mishra and Singh, 2010; Wilhite et al., 2007).

Generally, conceptual and operational drought definitions are found in literature. Conceptual definitions are stated in relative terms in order to form an overall understanding for implementing drought policies, whereas operational concepts identify criteria for onset, end and severity of drought for particular applications. The latter are used to specify frequency, strength and duration of drought events for given periods (Mishra and Singh, 2010; Zargar et al., 2011).

As an example of a conceptual definition, drought is specified as an "extended period, a season, a year, or several years of deficient rainfall relative to the statistical multi-year mean for a region" according to the Encyclopedia of Climate and Weather (Schneider et al., 2011). Further, the UNCCD (1994) defines drought as the "naturally occurring phenomenon that exists when precipitation has been significantly below normal recorded levels, causing serious hydrological imbalances that adversely affect land resource production systems".

Since the deficiency of water arises from regional variabilities in the global water cycle, droughts are strongly related to climatic circulation patterns and therefore not confined to a specific climate zone (AghaKouchak et al., 2015; Van Loon, 2015). The exclusive focus on precipitation, however, is not sufficient for describing the phenomenon of drought, as the importance of soil moisture losses like evaporation and transpiration as well as the role of additional water sources from lateral inflows is neglected. Further, temporal aspects of precip-

itation deficits are not considered. In respect to the local water balance, a universal drought concept needs reference to water supply, demand and management. Thus, its quantification is difficult (Lloyd-Hughes, 2014). Likewise, drought impacts vary significantly from one region to another and can be seen as a result of the interaction between drought as a natural event and the demand society assigns to water supply (National Drought Mitigation Center, 2016). As a result, both the quantity of water shortage and the susceptibility on ground conditions are decisive factors of drought impacts, since a drought event manifests itself through deficient water availability for humans, plants and animals. Differences in hydro-meteorological parameters, socio-economic aspects and the stochastic nature of water demand in various regions around the globe have become a barrier to precisely and universally define drought (Mishra and Singh, 2010; Smakhtin and Schipper, 2008; Zargar et al., 2011).

### 2.1.2 Types of drought

Regarding the operational drought definition, three main types of physical drought and one associated with human activity were established (Wilhite and Buchanan-Smith, 2005; Zargar et al., 2011). An overview of drought types and their order of occurrence is displayed in Figure 2.1, showing respective main driving factors and effects.
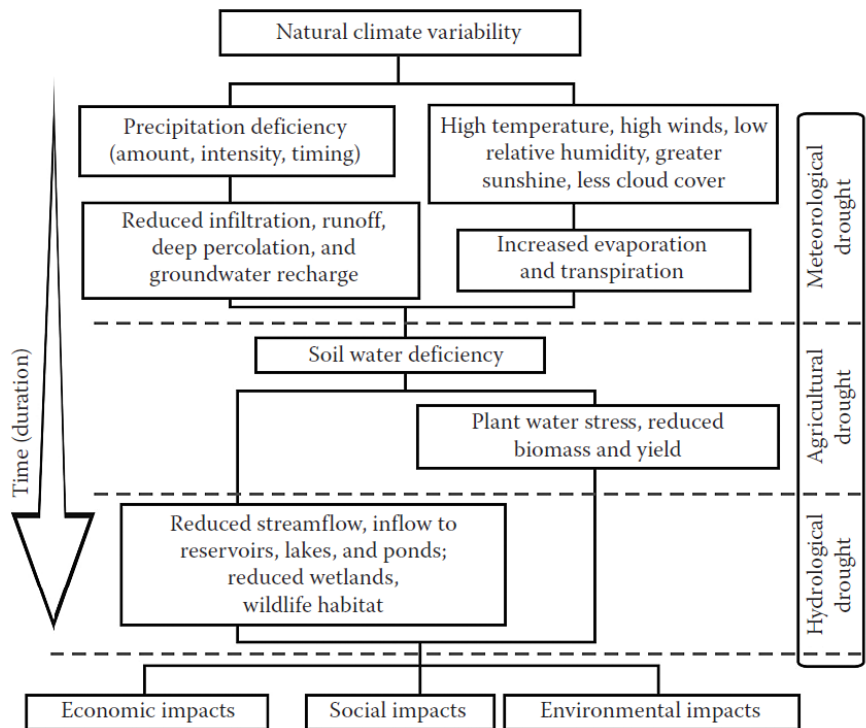


**Figure 2.1:** Physically based types of drought, effects and interconnections (adapted from Hayes et al., 2012)

Meteorological drought is characterized by precipitation deficiency and a possible elevated potential evapotranspiration, occurring over large areas and prevailing through a considerable time span. Hence, it is defined as a temporary period of abnormal dryness and can be measured according to its intensity (level of dryness compared to normal amount) and duration (Smakhtin and Schipper, 2008; Van Loon, 2015; Wilhite, 2000). Agricultural drought

is triggered by a deficit of soil moisture, which occurs mostly in the root zone and, as a consequence, leads to the reduction of water supply to vegetation. In this case, precipitation shortage is sufficient to cause reduced plant growth and crop production. Hence, soil moisture content can be seen as the main indicator for agricultural drought. However, the relationship between precipitation and infiltration is controlled by multiple parameters such as antecedent soil moisture conditions, slope, soil type (esp. water holding capacity) and the intensity of precipitation events (Dai, 2011; Van Loon, 2015; Wilhite and Buchanan-Smith, 2005). Hydrological drought is related to a below-average water content in surface and sub-surface water such as streams, reservoirs, groundwater aquifers, lakes and soil. Usually, there exists a larger time lag between an event of meteorological drought and the occurrence of hydrological drought. Likewise, recovery of these water cycle components is slow due to long recharge periods (Smakhtin and Schipper, 2008; Van Loon, 2015; Wilhite, 2000; Wilhite and Buchanan-Smith, 2005).

All in all, these types of drought represent different stages of the same naturally indicated process. A drought event is mainly driven by the deficiency of rainfall and/or an increased evapotranspiration (Seneviratne et al., 2012). The more spatially and temporally extensive this period of precipitation deficiency, the more likely other drought types will occur as a consequence. Finally, it can propagate through economic sectors and society. In this regard, socio-economic drought links the supply and demand of some economic commodity or service with components of physical drought. Accordingly, a drought event occurs when the demand of an economic good like water or hydroelectric power exceeds supply, resulting from weather-related shortfall. Hence, this concept demonstrates the strong symbiosis between physical drought and human activity. The frequency of droughts can increase on account of an alteration of physical parameters as well as a varying societal vulnerability to water shortages (Smakhtin and Schipper, 2008; Wilhite, 2000).

## 2.2 El Niño–Southern Oscillation (ENSO)

### 2.2.1 Definition and driving forces

Representing the most important year-to-year climate variation on the planet, El Niño-Southern Oscillation (ENSO) describes the irregularly periodical fluctuation between abnormally warm (El Niño) and cold (La Niña) Sea Surface Temperatures (SST) in the tropical Pacific, coupled with a variation in air pressure of the overlaying atmosphere (Southern Oscillation). Recurring in the range of 2-7 years, this phenomenon arises from large-scale interactions between ocean and atmosphere (Allan, 2000; McPhaden et al., 2006).

The Southern Oscillation refers to changes in the atmospheric pressure pattern connecting the Indian and Pacific Oceans and represents the atmospheric component of the combined oceanic-atmospheric ENSO phenomenon. This in turn is closely tied to the strength of Pacific trade winds. In this regard, the positive feedback between trade wind intensity and zonal SST is recognized as the Bjerknes feedback (Bjerknes, 1969) and considered a core feature of ocean-

atmosphere interaction (McPhaden et al., 2006). ENSO exhibits three phases: warm SST in the equatorial Pacific (El Niño), cold SST in the equatorial Pacific (La Niña), and near-neutral conditions (Hanley et al., 2003). Under normal conditions, the easterly trade winds pile up warm surface water in the western equatorial Pacific, whereas colder subsurface water wells up in the east along the equator and off the west coast of South America. With the overburden of warm water decreased in the eastern Pacific, the thermocline tilts upward towards the coast of South America (see Figure 2.2, left). The east-west contrast of surface temperatures hereupon increases the difference in pressure and again drives the trade winds (Cai et al., 2015; McPhaden et al., 2006; Rosenzweig and Hillel, 2008).
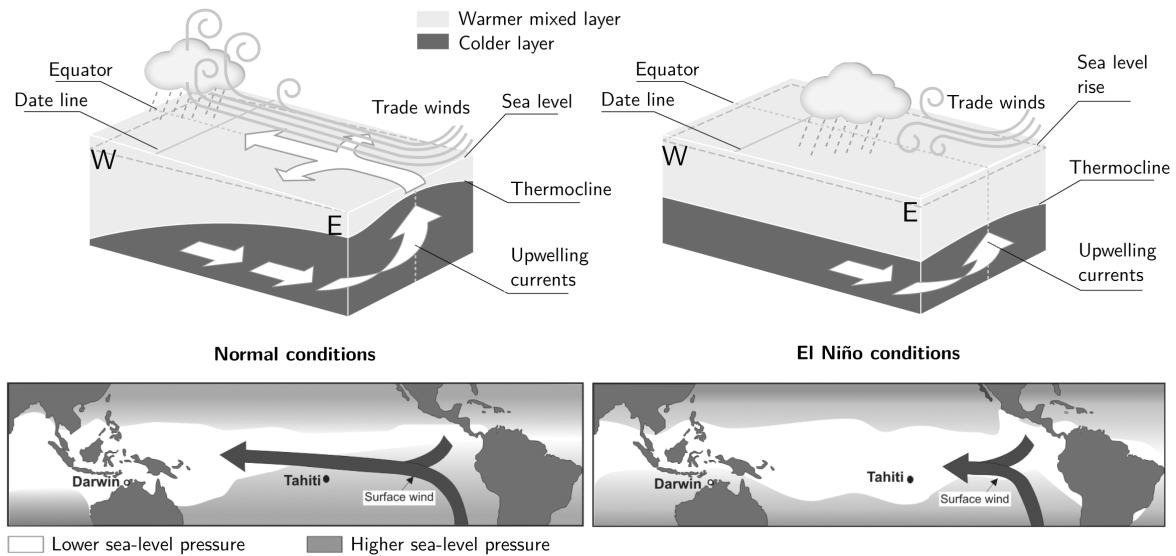


**Figure 2.2:** Schematics of normal (left) and El Niño (right) conditions in the equatorial Pacific Ocean and atmosphere to illustrate the Bjerknes feedback in the course of ENSO (modified after Rojas et al., 2014; Rosenzweig and Hillel, 2008)

El Niño (literally "the little boy") refers to "the Christ child". Peruvian and Ecuadorian fishermen gave this name to the occasional presence of warm ocean currents around Christmas time, displacing the normal cool coastal surface water and leading to a decreased amount of fish (Rosenzweig and Hillel, 2008). El Niño is also known as the warm phase of ENSO. This warming of the eastern Pacific is a result of the relaxation of westward trade winds, which respond to the falling air pressure in the eastern compared to rising pressure in the western Pacific (McPhaden et al., 2006). If the trades are weaker than normal, less warm surface water is piled up in the west and the thermocline is not as tilted (see Figure 2.2, right). Consequently, upwelling in the east brings warmer water to the surface than under normal conditions. Since the eastern Pacific becomes less cold, the precipitation pattern changes so that persistent rainfall located over the warmer sea surface expands eastward into the central Pacific (Sarachnik and Cane, 2010). This change in atmospheric conditions goes along with a lowered air pressure in the eastern Pacific. Hence, the Bjerknes feedback now runs reversely with weakened trade winds and SST warming trends reinforcing each other in the course of a developing El Niño (McPhaden et al., 2006). Figure 2.2 demonstrates the outlined ENSO mechanisms in the equatorial Pacific under both normal and El Niño conditions.

La Niña (literally "the little girl") describes the cool phase of ENSO and is characterized by abnormally cold SST in the eastern equatorial Pacific. Here, the positive feedback mechanisms of normal ENSO conditions are enhanced. Thus, a stronger than normal zonal asymmetry in SST, precipitation and thermocline exists in the tropical Pacific (Vecchi and Wittenberg, 2010). Accordingly, an unusually strong flow of cold water moves up on the west coast of South America. Due to strong upwelling, more cold water is transported to the sea surface and carried in a western direction (Strahler, 2011).

### 2.2.2 Global effects

Cold and warm ENSO events affect not only the seasonal weather of adjacent regions in the equatorial Pacific but have also an impact on precipitation and temperature variability around the world.
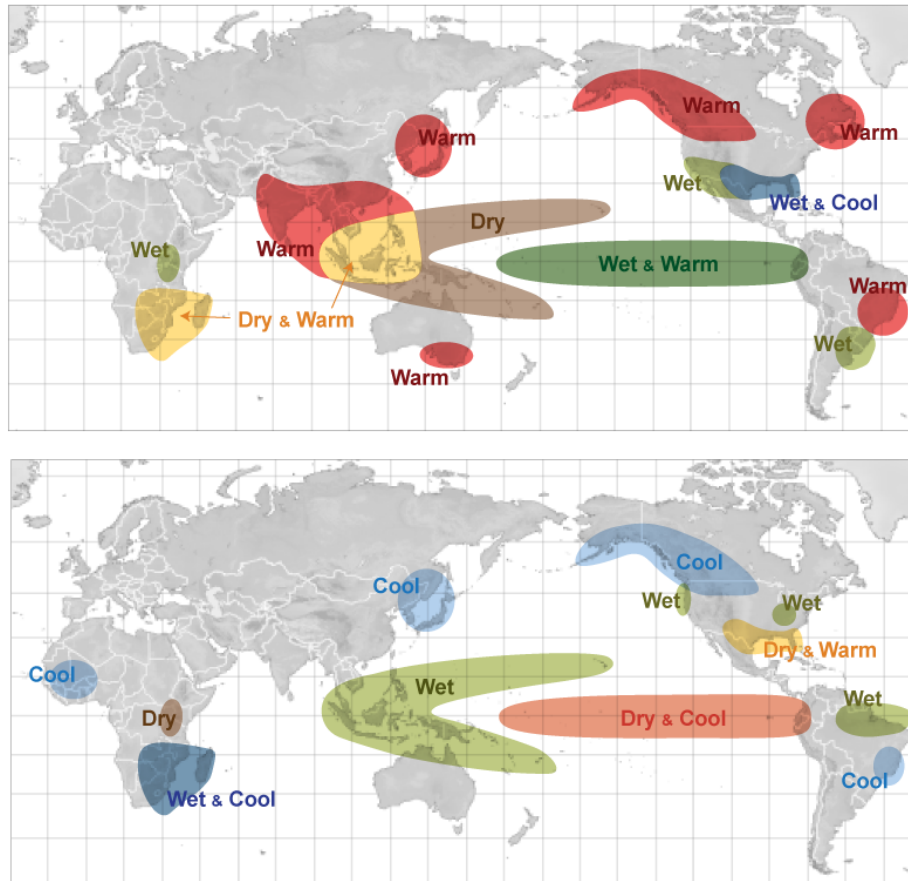


**Figure 2.3:** Regions of significant changes from normal weather related to El Niño (top) and La Niña (bottom) during December to February (NOAA, 2014)

ENSO influences large-scale circulations including the Hadley and Ferrel cell as well as the jet streams. These teleconnections have been studied by analysing climatic historical record and, more recently, by using satellite data. In a series of publications, Ropelewski and Halpert (1987, 1989, 1996) investigated and documented large-scale patterns of precipitation and surface temperatures associated with both the warm and the cold phase of ENSO around the globe. Revealed significant teleconnections were presented in a schematic map, which

is frequently used to arrange the current understanding of ENSO relations with seasonal weather variables (Yang and DelSole, 2012). These maps have been revised and reviewed by means of remotely sensed time series analyses (e.g. Kogan, 2000; Kuenzer et al., 2009). Figure 2.3 displays maps of the typical global pattern of precipitation and temperature anomalies in relation to El Niño and La Niña, respectively. The registered weather anomalies are induced by a shift in the global jet stream caused by ENSO.

Regarding Africa, per trend drier effects can be identified over south-eastern Africa during El Niño and over the southern part of eastern Africa during La Niña events for the period between December and February. During these months, ENSO dynamics generally reach its minimum or maximum. Since ENSO-related drought stands in the focal point of this thesis, southern and eastern Africa are selected as core regions of the presented analysis.

## 2.3   State of the art

### 2.3.1   Drought indices

Drought indicators or indices, typically based on meteorological, pedological, hydrological and vegetation-related parameters, are used in order to characterize strength, duration, and spatial extent of drought (Steinemann et al., 2005). With the aim of drought identification and the given constrains of a slow onset, gradual recovery as well as the existence of different drought categories and several influenced sectors, multiple indices have been developed. However, according to the scientific consensus, no leading indicator exists. Every type of index addresses another part of the hydrological cycle and has therefore its benefits for distinct specific applications. Thus, the multitude of indices itself resembles the diversity of drought impacts (Van Loon, 2015).

Prevalently, drought indices are classified depending on the type of associated impact or the variables they relate to. As a result, three popular categories are meteorological, soil moisture (agricultural) and hydrological drought indices (Zargar et al., 2011). Table 2.1 gives an overview of the most prominent drought indices including their types and main characteristics.

#### 2.3.1.1   Meteorological drought indices

Meteorological drought indices are related to climatological parameters such as precipitation, temperature, and evapotranspiration. Here, precipitation is regarded the most important variable (Dai, 2011; Steinemann et al., 2005). Examples for common meteorological drought indices and their main characteristics, benefits and limitations are given in Table 2.1.

The most widely applied meteorological index is the Standardized Precipitation Index (SPI) (McKee et al., 1993), which is utilized in this thesis. It comprises fitting and transforming a long-term rainfall time series into a normal distribution with zero mean and unit standard deviation. Further, the SPI compares actual precipitation with its multi-year average and can be computed for different time scales and, thus, indirectly considers the impact of accumulated precipitation deficits from an agricultural and hydrological perspective. The SPI can

**Table 2.1:** Selection of prominent drought indices listed by drought type (M: Meteorological, A: Agricultural, H: Hydrological)

| Index | Publication | Type | Description |
|---|---|---|---|
| Rainfall Anomaly Index (RAI) | Van Rooy (1965) | M | Average precipitation ranked to long-term record: Relative drought (Wanders et al., 2010) |
| Palmer Drought Severity Index (PDSI) | Palmer (1965) | M (A) | Departure of moisture balance from normal conditions, concept of water supply and demand, based on a bucket-type soil model |
| | | | ⊕ Comprehensive index: precipitation and air temperature; More complete understanding of water balance |
| | | | ⊖ Fixed temporal scale; Tested for the U.S., limited application in other regions |
| | | | (Seneviratne et al., 2012; Vicente-Serrano et al., 2012; Wanders et al., 2010; Zargar et al., 2011) |
| Standardized Precipitation Index (SPI) | McKee et al. (1993) | M (A,H) | Normalization, comparison of actual precipitation with multi-year average |
| | | | ⊕ Simplicity: independence from soil moisture, seasonality and topography; Application on different time scales → drought dynamics: M, A, H; Comparability across regions due to normalization |
| | | | ⊖ Neglecting evapotranspiration; Dependence on theoretical probability distribution |
| | | | (Lloyd-Hughes and Saunders, 2002; Val Loon, 2015; WMO, 2012; Zargar et al., 2011) |
| Effective Drought Index (EDI) | Byun and Wilhite (1999) | M | Standardized deviation of effective precipitation (Zargar et al., 2011) |
| Reconnaissance Drought Index (RDI) | Tsakiris and Vangelis (2005) | M | Extension of SPI, relation of precipitation to potential evapotranspiration (physically based approach) (Niemeyer, 2008; Zargar et al., 2011) |
| Standardized Precipitation Evapotranspiration Index (SPEI) | Vicente-Serrano et al. (2010) | M | Combination of simplicity and multi-temporal quality of SPI with sensitivity of PDSI to evaporation (Vicente-Serrano et al., 2012; WMO, 2012) |
| Palmer Moisture Anomaly Index (Z-index) | Palmer (1965) | A | Deduction from PDSI calculation, Moisture anomaly of current month in Palmer model without consideration antecedent conditions (Keyantash and Dracup, 2002) |
| Crop Moisture Index (CMI) | Palmer (1968) | A | Sum of an evapotranspiration deficit based on precipitation and soil moisture infiltration, computed with PDSI parameters (Keyantash and Dracup, 2002; Wanders et al., 2010) |
| Crop Specific Drought Index (CSDI) | Meyer et al. (1993) | A | Estimated soil water availability based on climatological data, soil and crop phenology information (Zargar et al., 2011) |
| Soil Moisture Deficit Index (SMDI) | Narasimhan and Srinivasan (2005) | A | Weekly soil moisture deficits at varying depths within modelled soil profile based on simulated or observed soil moisture content (Wanders et al., 2010) |
| Palmer Hydrological Drought Index (PHDI) | Palmer (1965) | H | Computed with PDSI model, more stringent criterion of drought termination (Dai, 2011) |
| Drought severity (S)/ Total water deficit | Dracup et al. (1980) | H | Duration of below-normal discharge and average departure from long-term mean (Zargar et al., 2011) |
| Surface Water Supply Index (SWSI) | Shafer and Dezman (1982) | H | Weighted averages of standardized anomalies in surface water component, extension of PHDI, inclusion of snow accumulation (Keyantash and Dracup, 2002; Zargar et al., 2011) |
| Regional Streamflow Deficiency Index (RSDI) | Stahl (2001) | H | Clustering deficiency values of discharge compared with historic measurements (Wanders et al., 2010) |

be computed on seasonal scales and, thus, used in order to quantify agricultural drought. Its value equals the number of standard deviations the cumulative precipitation deficit deviates from the normalized average (Seneviratne et al., 2012; Zargar et al., 2011). Other meteorological drought indices additionally incorporate surface air temperature to account for the effect of actual or potential evapotranspiration. In this regard, the Palmer Drought Severity Index (PDSI) introduced by Palmer (1965) is to mention as an early landmark in the development of drought indices. This index is founded on the concept of water supply and demand instead of precipitation anomaly and is based on a generic two-layer bucket-type soil model (Seneviratne et al., 2012; Vicente-Serrano et al., 2012; Wanders et al., 2010). One of the more recent developments in the field of meteorological indices is the Reconnaissance Drought Index (RDI) proposed by Tsakiris and Vangelis (2005). Another recent SPI-related index is the Standardized Precipitation Evapotranspiration Index (SPEI) developed by Vicente-Serrano et al. (2010). This index intents to combine the sensitivity of PDSI with the simplicity and multi-temporal quality of SPI (Vicente-Serrano et al., 2012; WMO, 2012).

### 2.3.1.2  Soil moisture (agricultural) drought indices

With the PDSI and focus directed on soil moisture and actual evapotranspiration, explicit agricultural drought indices were established (Niemeyer, 2008). These are also known as soil moisture indices, since soil moisture content is used as the indicating variable for agricultural drought. Thus, drought situations are detected on the basis of water amount stored in the unsaturated zone. Values of soil water balance can either originate from observed data (e.g. in-situ measurements, remote sensing-based data) or can be simulated by means of soil moisture models (Keyantash and Dracup, 2002; Zargar et al., 2011). These indicators aim to quantify agricultural drought by means of soil moisture. Again, the most frequently used drought indices based on soil moisture are summarized in Table 2.1. However, monitoring agricultural drought is not only restricted to indices relying on soil moisture. Likewise, agricultural drought can be analysed based on seasonally accumulated rainfall anomalies or vegetative stress, which is presented in this thesis.

### 2.3.1.3  Hydrological drought indices

Indices for hydrological drought are based on parameters describing the bulk water supply such as water levels in streams and lakes, reservoir storage, groundwater levels and snowpack. They aim to provide a comprehensive picture of delayed hydrological drought impacts. Generally, discharge or streamflow is the most prominent variable for indicating hydrological drought (Keyantash and Dracup, 2002; Zargar et al., 2011). Commonly used hydrological drought indices are listed in Table 2.1.

### 2.3.1.4 Remote sensing-based drought indices

The development of earth observation satellites with new sensors and algorithms has constantly led to the incorporation of additional remotely sensed information to drought assessment. Remote sensing opens up new possibilities for drought detection and monitoring (Niemeyer, 2008; Zargar et al., 2011). Amongst others, the advantages of remote sensing methods lie in the availability of consistent data at high repetition rates, allowing the derivation of information at large spatial scales (Niemeyer, 2008).

**Table 2.2:** Selection of prominent remote sensing-based (RS) drought indices

| Index | Publication | Type | Description |
|---|---|---|---|
| Normalized Difference Vegetation Index (NDVI) | Tucker (1979) | RS | Normalized difference between maximum absorption of radiation of RED and NIR |
| | | | ⊕ Simplicity; Applicable over large areas (depending on spatial resolution of satellite imagery); Distinction between vegetation and other surfaces; Measurement rather than interpolation |
| | | | ⊖ Sensitivity to soil moisture; Saturation tendency with large biomass, Non-linear behaviour, scaling influences |
| | | | (Zargar et al., 2011) |
| Soil-Adjusted Vegetation Index (SAVI) | Huete (1988) | RS | Ratio based on RED and NIR, additional soil adjustment factor |
| Vegetation Condition Index (VCI) | Kogan (1990) | RS | Relative normalization to absolute maximum and minimum NDVI in data record for given period |
| | | | ⊕ See NDVI; Suitability to monitor drought impact on vegetation (agricultural drought) |
| | | | ⊖ See NDVI; Limited application to northern hemisphere; Indirect measure of moisture conditions (vegetation stress due to insects, lack of nutrients, diseases) |
| | | | (Domenikiotis et al., 2004; Du et al., 2013; Kogan et al., 2005) |
| Temperature Condition Index (TCI) | Kogan (1995) | RS | VCI approach applied on surface temperature |
| Vegetation Health Index (VHI) | Kogan (1995) | RS | Combination of VCI and TCI |
| Normalized Difference Water Index (NDWI) | Gao (1996) | RS | Ratio of NIR and SWIR |
| Enhanced Vegetation Index (EVI) | Huete et al. (2002) | RS | NDVI with feedback loops to minimize atmospheric and soil bias (Zargar et al., 2011) |
| Perpendicular Drought Index (PDI) | Ghulam et al. (2007) | RS | Ratio based on RED and NIR with perpendicular geometrical construction on reflectance space (Niemeyer, 2008) |

On the one hand, remote sensing data has been used to monitor drought-related variables from a climatological and hydrological point of view by using multispectral data with optical/near-infrared and/or thermal wavelengths or radar sensors. Retrieved variables include precipitation, soil moisture or evapotranspiration. On the other hand, satellite observations can be

used to quantify drought impacts from an ecosystem perspective, which comprises vegetation health and growth. Since drought can lead to reduced photosynthetic capacity and variations in absorption of solar radiation at photosynthetically active wavelengths by plants, many remote sensing-based drought indices are focused on vegetation (AghaKouchak et al., 2015). Table 2.2 presents a list of selected remote sensing-based drought indices.

Most of these vegetation-related drought indices rely on the difference between the absorption of radiation in the visible red (RED) spectral domain, indicating chlorophyll density, and the reflectance in the near infrared (NIR) electromagnetic spectrum, which results from scattering effects within the canopy and, thus, is sensitive to green leaf structure. As a consequence, this difference can be utilized to estimate the intercepted fraction of photosynthetically active radiation (Anyamba and Tucker, 2012; Karnieli et al., 2010; Tucker and Choudhury, 1987). Figure 2.4 shows the typical spectral signature of vegetation and the spectral domains of bands from commonly used earth observation sensors for large-scale vegetation monitoring, the Advanced Very-High-Resolution Radiometer (AVHRR) and Moderate-resolution Imaging Spectroradiometer (MODIS). The first bands cover the visible magnetic spectrum with 0.58 to 0.68 $\mu$m for AVHRR and 0.62 to 0.67 $\mu$m for MODIS, whereas the second bands show reflectance in the NIR domain with 0.73 to 1.10 $\mu$m and 0.84 to 0.87 $\mu$m, respectively (Anyamba and Tucker, 2012; NASA, 2016a).
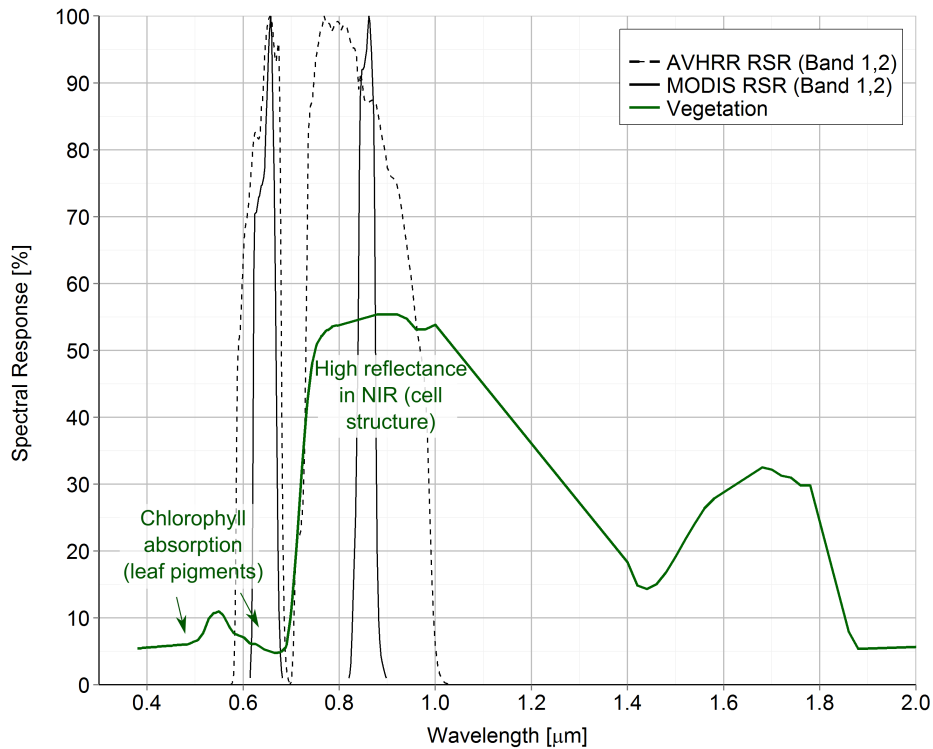


**Figure 2.4:** Spectral signature of vegetation based on deciduous forest from ASTER spectral library 2.0 (Baldridge et al., 2009) with the RSR of AVHRR bands 1 and 2 (STAR, 2008) and MODIS Terra bands 1 and 2 (NASA, 2016b)

The Normalized Difference Vegetation Index (NDVI), which was first applied by Rouse et al. (1973) and further developed by Tucker (1979), makes use of the spectral signature of vegetation, showing a low reflectance in the visible domain and high values in the NIR spectrum

(see Figure 2.4. It is described as the most prominent remote sensing-based vegetation index, which subsequently has given rise to numerous NDVI-based and refined indices for drought monitoring (Niemeyer, 2008). The NDVI is defined as follows:

$$\text{NDVI} = \frac{(\rho_{NIR} - \rho_{RED})}{(\rho_{NIR} + \rho_{RED})} \tag{2.1}$$

where $\rho$ denotes the spectral reflectance within respective bands of multispectral remote sensing data (Karnieli et al., 2010).

The NDVI laid the foundation for the development of several drought indices such as the Vegetation Condition Index (VCI), which is used in this thesis. Kogan (1990) introduced the VCI as a modification of the NDVI computed from AVHRR radiance. A relative normalization of the NDVI to its absolute maximum and minimum is undertaken in order to assess changes in the NDVI through time. In doing so, influences of local parameters and spatial variability in phenology between different land cover types and climate conditions are lowered. The VCI aims to separate short-term weather dynamics from the long-term ecological signal for drought monitoring. This is achieved by scaling the NDVI values in relation to the amplitude of their range during the available time period. The signal is further amplified by ranking it on a linear scale where the minimum value equals 0 and the maximum 100 (Karnieli et al., 2010; Kogan and Sullivan, 1993). The VCI is calculated as follows.

$$VCI = \frac{(NDVI_j - NDVI_{min}) * 100}{NDVI_{max} - NDVI_{min}}, \tag{2.2}$$

where $NDVI_j$ is the average NDVI over a composite period of interest (week, decade, month etc.), $NDVI_{min}$ and $NDVI_{max}$ are the corresponding multi-year minimum and maximum NDVI values in the available data record for the specific analysed period (Kogan and Sullivan, 1993; Zargar et al., 2011).

The relationship between reflectance characteristics in the RED and NIR spectral domains is also used by other indices such as Soil-Adjusted Vegetation Index (SAVI), Perpendicular Drought Index (PDI) and Enhanced Vegetation Index (EVI) (see Table 2.2). Further, re-motely sensed surface temperature, which is derived from thermal channels of various satellite instruments, can successfully contribute to the quantification of drought conditions. For this purpose, Land Surface Temperature (LST) is computed from bands representing the thermal infrared (TIR) spectrum. Prominent indicators based on TIR data are the Temperature Condition Index (TCI) and the Vegetation Health Index (VHI) (AghaKouchak et al., 2015; Karnieli et al., 2010). Another complementary to the NDVI is the Normalized Difference Water Index (NDWI), making use of the relation between NIR and short-wave infrared (SWIR) spectral domains.

All in all, diverse enhanced, modified and combined remote sensing-based drought indices can be found and new indicators are frequently proposed. For a more detailed insight into the high amount of remote sensing-based drought indices, the interested reader is referred to AghaKouchak et al. (2015), Niemeyer (2008) and Zargar et al. (2011).

### 2.3.2 ENSO indices

In order to quantify the strength and monitor the temporal sequence of ENSO warm and cold phases, several operationally used ENSO proxies have been developed based on oceanic and/or atmospheric parameters. These indices define the strength and phase of ENSO events on a monthly scale and rely on variables measured over various parts of the Pacific ocean (Propastin et al., 2010). In the following, some frequently used ENSO indices will be presented.

On the one hand, temperature-based indices depend on SST anomalies within different defined regions of the equatorial Pacific, located between 5°N and 5 or 10°S. The so-called Niño-1 and Niño-2 regions are located off the coast of Peru and Ecuador and near the Galapagos Islands, respectively, whereas the Niño-3 region extends in the central and Niño-4 in the western part of the tropical Pacific. Niño-3.4 overlaps portions of the latter regions. Its SST anomalies have been regarded the best SST-based proxy for the core ENSO phenomenon (Barnston et al., 1997; Hanley et al., 2003). A common quantitative definition and standard measure of El Niño and La Niña events is based on Niño-3.4 SST anomalies regarding the reference period of 1971-2000. The 3-month running mean of SST anomalies in this region is represented in the Oceanic Niño Index (ONI), which is displayed in Figure 2.5 (bottom right) for the period of 2000-2016. For an El Niño event, five consecutive monthly ONI values have to be above the threshold of 0.5°C (below -0.5°C for La Niña; NOAA, 2016d). Based on ONI, the intensities of El Niño and La Niña can be measured. Accordingly, weak (SST anomaly: 0.5 to 0.9°C), moderate (1.0 to 1.4°C), strong (1.5 to 1.9°C) and very strong (≥2.0°C) events can be distinguished (Golden Gate Weather Service, 2016). In this regard, Table 2.3 lists the ENSO warm and cold events having occurred since 2000 according to their ONI-based intensities.

**Table 2.3:** El Niño and La Niña years categorized by intensity (ONI values) between 2000 and 2016 (Golden Gate Weather Service, 2016)

| | El Niño | | La Niña | |
|---|---|---|---|---|
| Weak | Moderate | Very Strong | Weak | Moderate |
| 2004-05 | 2002-03 | 2015-16 | 2000-01 | 1999-00 |
| 2006-07 | 2009-10 | | 2011-12 | 2007-08 |
| | | | | 2010-11 |

On the other hand, the Southern Oscillation Index (SOI) measures the normalized difference in sea level pressure between Papeete, Tahiti, and Darwin, Australia. It illustrates the large-scale fluctuations in air pressure between the western and eastern equatorial Pacific during El Niño and La Niña events. The negative phase implies below-normal pressure at Tahiti and higher-than-average pressure at Darwin, which coincides with abnormally warm SST in the eastern Pacific typical for El Niño. Vice versa, La Niña is associated with a positive SOI value (NOAA, 2016f). Another ENSO index is Outgoing Longwave Radiation (OLR) which is measured by AVHRR across equatorial areas from 160°E to 160°W and then converted into

a standardized anomaly index. Negative values represent conditions of enhanced convection and hence are associated with El Niño (NOAA, 2016e).

What is more, a combined index is provided in form of the MEI, which is predicated on six observed variables over the tropical Pacific: Sea level pressure, zonal and meridional surface winds, SST, surface air temperature, and total cloudiness fraction of the sky. These parameters are combined via Principal Component Analysis (NOAA, 2016b). Figure 2.5 shows the temporal evolution of ENSO from March 2000 to April 2016 (the study period used in this thesis) by means of different ENSO indices.
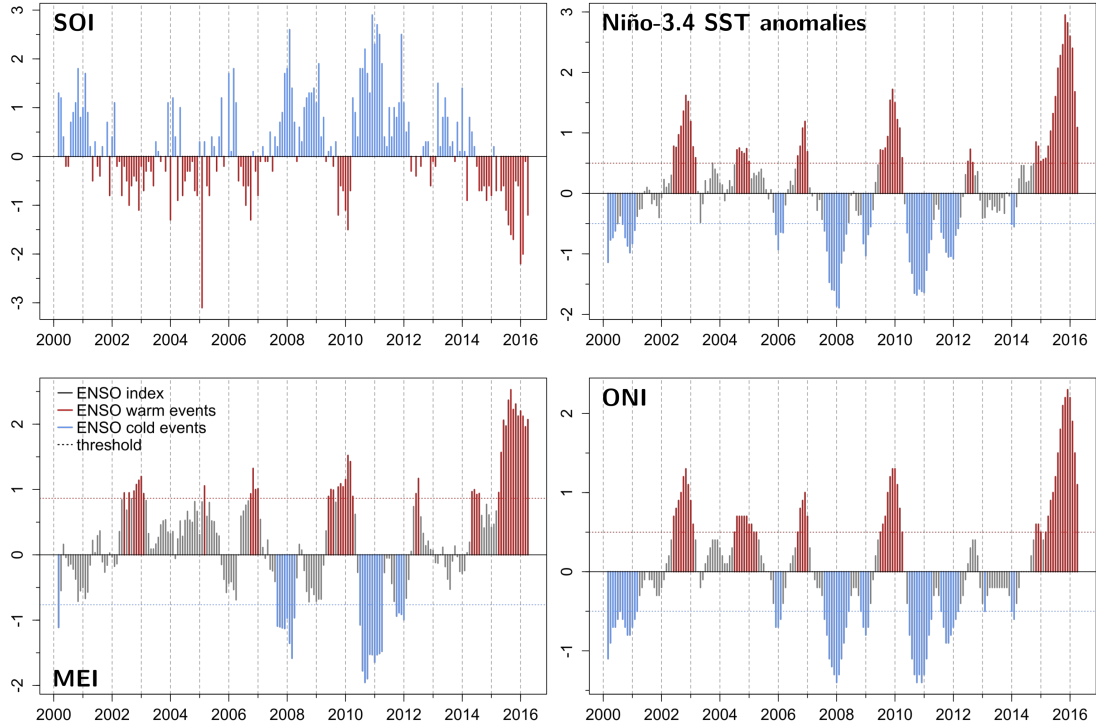


**Figure 2.5:** Time series of different ENSO indices for 2000 - 2016: Values associated with El Niño phases are displayed in red, La Niña is shown in blue. For Niño-3.4 SST anomalies and ONI, $\pm 0.5°$C is used as threshold, whereas the $\pm 0.2$ percentiles threshold is applied for MEI (Data source: NOAA, 2016a; NOAA, 2016c; NOAA, 2016f; NOAA, 2016g).

### 2.3.3 Remote sensing-based drought monitoring

#### 2.3.3.1 Operational drought information platforms

In order to operationally provide broad-scale information on droughts for the public, various drought-related data and information platforms emerged both at regional and global level. In this framework, the U. S. Drought Monitor (USDM) integrates different indices from a meteorological, agricultural and hydrological perspective into final maps with coarse spatial resolution of several kilometres, displaying the magnitude and extent of drought over the United States (Deng et al., 2013; Svoboda et al., 2002). Another regional-scale example is the European Drought Observatory (EDO), which consists of drought-relevant information derived from meteorological, agricultural and remote sensing-based drought indices at a spatial resolution of about 9 km (Sepulcre-Canto et al., 2012).

In a global context, the Global Integrated Monitoring and Prediction System (GIDMaPS) provides meteorological and agricultural drought information derived from multiple remote sensing- and model-based precipitation and soil moisture data with spatial resolutions of up to 14 km (Hao et al., 2014). Further, a platform for drought detection and early warning focused on food security is provided by the Famine Early Warning Systems Network (FEWS NET), which, amongst others, is maintained by the U.S. Agency for International Development (USAID). This information system was established in 1985 and combines rainfall-, vegetation index-based and model-based indicators such as the SPI and NDVI at different spatial resolutions (250 m to 10 km). Regional focus is laid on Sub-Saharan Africa, Afghanistan and Central America (Senay et al., 2015). A more recent global monitoring system in terms of agricultural drought is the Global Agricultural Drought Monitoring and Forecasting System (GADMFS) presented by Deng et al. (2013). It mainly relies on NDVI-based drought indicators such as VCI as well as other agricultural drought-related variables like soil moisture and land cover type. Thereby, the spatial resolution was remarkably improved by using MODIS-derived NDVI imagery (250 m).

Probably, the most consistent and comprehensive drought information system focussed exclusively on Africa represents the African Flood and Drought Monitor (AFDM) developed by Princeton University. The web-based platform provides an estimate of drought conditions by integrating hydrological models, remote sensing data and seasonal climate forecasts. Thereby, different drought indices are derived: SPI, modelled soil moisture, stream flow and vegetation-related indices (Sheffield et al., 2014).

### 2.3.3.2   Remote sensing-based drought monitoring studies over Africa

Considering regional drought monitoring within Africa, numerous remote sensing-based studies, dedicated to desertification in the Sahel zone, have been published (e.g. Anyamba and Tucker, 2005; Brandt et al., 2014; Herrmann et al., 2005; Heumann et al., 2007). A comprehensive summary of related research including the ongoing debate on the Sahelian "greening" is given by Karlson and Ostwald (2016), Mbow et al. (2015) and Knauer et al. (2014).

Eastern Africa, including the Horn of Africa, represents another focal region of remote sensing-based studies on drought conditions. Awange et al. (2016a), for example, studied the relation between meteorological and hydrological drought dynamics by relating satellite-derived SPI with total water storage deficits. Ntale and Gan (2003) proved the suitability of SPI to monitor eastern African droughts compared to PDSI variations. Further, Dutra et al. (2013) analysed the 2010-2011 drought in the Horn of Africa by means of precipitation, soil moisture data and NDVI. A rainfall deficit in both rainy seasons was revealed, leading to protracted negative soil moisture anomalies and vegetation stress. The 2010-2011 drought was further studied by Anderson et al. (2012), Meroni et al. (2014) and AghaKouchak (2015). A study carried out by Viste et al. (2013) revealed 2009 as a year of exceptional large-scale drought in Ethiopia based on a SPI time series (1972-2011). Southern Ethiopia shows a general precipitation decline during the main rainy season. Taking into account the vague nature of vegetative

drought in a model, Rulinda et al. (2012) carried out a study using NDVI images of eastern Africa from 2005 to 2006. Thereby, a severe drought was detected, affecting about 60 % of the vegetated study area. Studying the impacts of drought on vegetation, Rulinda et al. (2013) applied an object-based approach on NDVI and rainfall estimates in order to quantify the spatio-temporal movement of vegetative droughts in eastern Africa during the drought year 1999. Based on observed similar trajectories, a relation between vegetative drought and rainfall deficit was revealed.

With a focus on southern Africa, Rouault and Richard (2005) investigated droughts by means of the SPI. An overall increase of droughts at a 2-year scale since the 1970's was revealed. Further, a prolonged rainfall-induced drought was indicated for 2002/2003 over southern Africa. This severe drought period was additionally revealed from a study focussed on meteorological and hydrological droughts in the South African Crocodile River catchment (Mussá et al., 2015). What is more, Unganai and Kogan (1998) investigated the ability of the AVHRR-derived drought indices VCI and TCI to detect temporal and spatial characteristics of droughts in southern Africa. A validation with ground truth data revealed a good performance for the prediction of corn yields. In this regard, Sannier et al. (1998) developed a Vegetation Productivity Index (VPI) based on AVHRR-derived NDVI from 1981 to 1991 for southern Africa. In Zambia, the VPI was correlated with maize production, which indicates the possibility to quantitatively assess drought impacts on agriculture (Sannier et al., 1998). Mutowo and Chikodzi (2014) applied the VCI in order to study the spatial variation of drought in Zimbabwe from 2005 to 2010. Among multiple agricultural seasons under drought, 2007/08 was found to be the most affected one. In this context, Brown and Funk (2010) demonstrated the use of MODIS NDVI imagery as an accurate estimate of corn production, which enabled early food aid in Zimbabwe. Based on the analysis of NDVI time series carried out by Chisadza et al. (2015), drought seasons were identified in a catchment area within the Limpopo River Basin of Zimbabwe in 2002/03, 2005/06 and 2006/07. For southern Malawi, a pronounced agricultural drought was registered in 2004/05 by analysing maize yield data from 2000 to 2009 (Jayanthi et al., 2013). Thereby, significant links between maize yield losses and SPI were revealed.

As a continental scale approach, Rojas et al. (2011) analysed the probability of droughts affecting agricultural areas at the sub-national level in Africa from 1981 to 2009. The methodology was based on Vegetation Health Index (VHI) and phenological information derived from NDVI based on AVHRR data at 8 km resolution. Seasonal averages of VHI proved to be a valid drought indicator for the African continent and revealed results that mirror recorded major drought events during the study period. Furthermore, Naumann et al. (2012) evaluated the uncertainties with calculating the SPI and the corresponding effect on the level of confidence in drought monitoring over Africa. In another study, Naumann et al. (2014) compared different drought indicators, the SPI, SPEI and Soil Moisture Anomaly (SMA), according to their capability of drought detection across Africa. This was accomplished using different precipitation data sets. In both studies, Tropical Rainfall Measuring Mission (TRMM) data were proven most suitable to reliably monitor drought over Africa due to its high spatial

resolution. A remote sensing-based time series analysis carried out by Vicente-Serrano et al. (2015) investigated land degradation in semiarid regions on the globe and revealed essential information on the vegetation response to drought in the African Sahel, southern Africa and the Horn of Africa during 1982-2011. The drought indices used are SPEI and AVHRR-derived NDVI. As a result, the availability of water measured by SPEI mainly explains the variability of NDVI for South Africa, Namibia and areas of the Sahel. Nevertheless, no universal vegetation response to drought could be found, since land degradation in semiarid areas is controlled by numerous factors.
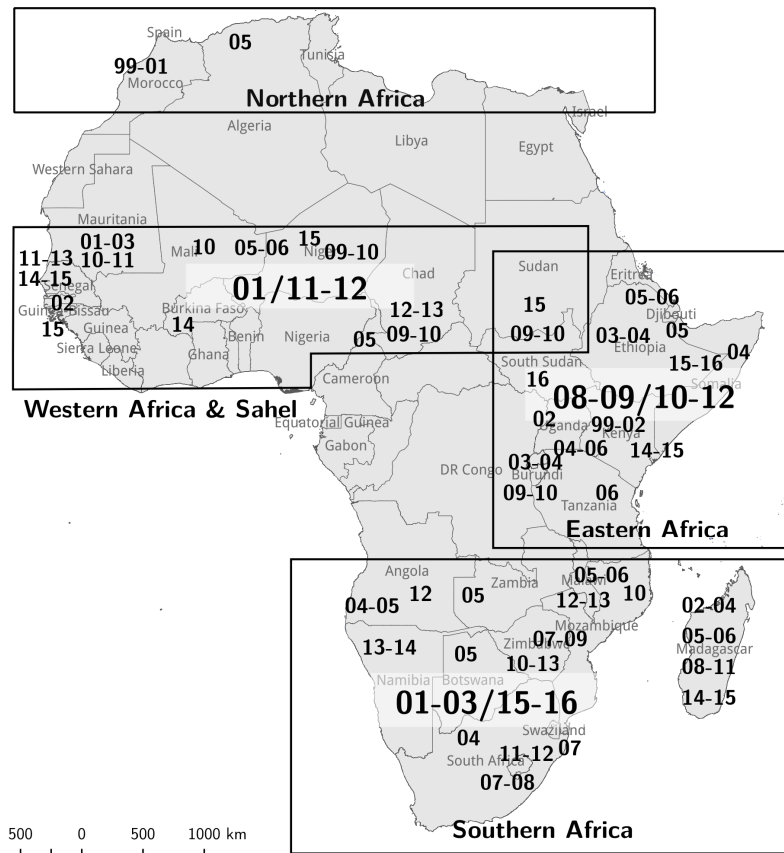


**Figure 2.6:** Years and African countries affected by droughts between 2000 and 2016 (information based on Guha-Sapir et al., 2016; Masih et al., 2014). Depicted years may refer to any area within respective countries.

In Figure 2.6, recorded years of drought events in Africa between 2000 and 2016 are distributed within a map. Underlying information is extracted from a comprehensive literature review on droughts in Africa (Masih et al., 2014) and the International Disaster Database EM-DAT (Guha-Sapir et al., 2016). Here, years of spatially wide-ranging droughts with effects on numerous adjacent countries are displayed in enlarged size. Positions of years indicate the affected country but not the specific sub-national region. Rectangular boxes roughly mark the extent of grouped regions. For this thesis, analyses are focussed on eastern and southern Africa, since these regions hold a particularly large record of droughts for the selected period.

### 2.3.4 Relation of ENSO and droughts in Africa

Numerous publications can be found regarding the relation between ENSO and drought conditions in Africa. These studies mostly rely on drought indices derived from observed, simulated or remotely sensed data. Above all, rainfall data and derived indices are commonly used. In this regard, remote sensing-based approaches mostly rely on AVHRR-based NDVI time series.

By correlating the ENSO index MEI with the drought indicator SPEI based on both observed and simulated climate model data, a strong link between ENSO and droughts over southern Africa was revealed for the rainy seasons (December to February) between 1989 and 2008 (Meque and Abiodun, 2015). What is more, 8 of the 12 major SPI-derived drought years in southern Africa during the 20$^{th}$ century coincide with El Niño, which indicates a given relation between ENSO and southern African rainfall (Rouault and Richard, 2005). Stige et al. (2006) exhibited the linkage between ENSO and the productivity of crops, livestocks, and pastures in Africa using national records and remote sensing data on pasture greenness from 1982-2003. Accordingly, overall African food production is reduced during El Niño conditions. However, the strongest effect is seen in southern African maize production. Further, Anyamba and Eastman (1996) studied changes in vegetation greenness in Africa between 1986 and 1990 and its relation to ENSO. Strong spatial and temporal teleconnection patterns between ENSO indices (SOI, OLR, SST anomalies) and NDVI variation were depicted by means of Principal Components Analysis (PCA). For southern Africa, NDVI resulted low during warm phase and high during cold phase events. Anyamba et al. (2001) also assessed the NDVI anomaly patterns over Africa during the specific El Niño event of 1997/98 and revealed two dominant clusters. Equatorial eastern Africa exhibits positive NDVI anomalies representing a lagged response to eastern Pacific warming. Concerning southern Africa, slightly greener than normal conditions were revealed from October to November, whereas the later season (January - May) showed abnormally dry conditions. Drought response in southern Africa was not as severe as in previous El Niño years, which can probably be explained by dampening influences of the western Indian and the equatorial Atlantic Ocean. Another study was carried out by Propastin et al. (2010) who analysed the vulnerability of vegetation over Africa to ENSO warm events via statistical correlation between AVHRR-derived NDVI and MEI as an ENSO index for the period 1982-2006. Accordingly, an El-Niño-driven vegetation decrease occurs most frequently in large areas of southern Africa including South Africa, Zimbabwe, Zambia, and Tanzania. What is more, vulnerability of vegetated areas to ENSO highly depends on the vegetation type. This revealed connection between warm phases of ENSO and drought conditions in southern Africa is further confirmed by Lyon (2004), Crétat et al. (2012), Kogan (2000), Richard et al. (2000) and Anyamba et al. (2002).

Plisnier et al. (2000) measured the teleconnection patterns between an ENSO index and several ecosystem variables in eastern Africa based on both remote sensing and climate data during 1982-1994. Although the effect of ENSO on climatic and ecological variability was confirmed, the impact pattern is complex and highly differentiated in space due to the contri-

bution of local climate systems, effects of large lakes, the proximity to the coast, topography and land cover. According to Philippon et al. (2014), who carried out a correlation analysis between long-term time series of Niño-3.4 SST index and AVHRR-derived NDVI, an asymmetrical vegetation signal in the rainy seasons over eastern Africa was uncovered. Observed teleconnection patterns of ENSO comprise an emerging dipole between negative correlation over the western part and positive correlations in the eastern part from October to November. For the long rains (March to May), only a weak impact of ENSO was revealed. Indeje et al. (2000) studied the rainfall patterns between 1961 and 1990 and their relation to ENSO. During El Niño years, relatively wet conditions were observed in both rainy seasons, whereas dry conditions dominated the rainy seasons of the following year. Contrary to southern Africa, eastern Africa faces droughts during La Niña (Masih et al., 2014). Lott et al. (2013) analysed the failure of the short rains during the eastern African drought of 2011 and attributed them to the consequences of the cold phase of ENSO.

On a continental scale, Philippon et al. (2014) revealed a strong dipole pattern in vegetation response during the peak phase of ENSO. Accordingly, areas south of 18°S are negatively correlated with ENSO, showing reduced photosynthetic activity during El Niño, whereas the North is positively correlated, showing enhanced NDVI north of 18°S. Hence, regional-scale dipoles and spatio-temporally propagative patterns were revealed as features of ENSO teleconnections over Africa. However, the Sahel exhibited a weak sensitivity of vegetation to ENSO, which could be explained by the small rain use efficiency of this area, the timing of rainy season in relation to ENSO and a closer linkage of precipitation to SST over the Mediterranean and Indian Ocean (Fontaine et al., 2011; Philippon et al., 2014).

Frequently, ENSO-related droughts have led to reduced agricultural yield, crop failure and even food insecurity in some parts of Africa (amongst others Funk et al., 2008; Stige et al., 2006). In particular, significant drought effects of ENSO on growing seasons were revealed for eastern and southern Africa (Brown et al., 2010). In this context, the 2010/11 drought in eastern Africa, which occurred during La Niña, caused food crises and famine in multiple countries with about 9 million people affected. It was considered one of the most extreme drought events of the region (Funk, 2011; OCHA, 2011). In addition, severe impacts on agriculture and food security have been registered for the recent drought period over southern Africa, which evolved in the context of the very strong El Niño in 2015/16. Because of extensive crop failures and an associated insecure food supply, humanitarian assistance is required for millions of people in Zimbabwe, Malawi, Mozambique and Madagascar until 2017 (GEOGLAM, 2016). Since severe ENSO-related drought impacts have been observed over eastern and southern Africa, these areas are selected as focal regions for this thesis.

# Chapter 3

# Study area

## 3.1 Geographical setting

The study area of this thesis covers the African continent, which is located between approximately 37°N and 34°S and about 17°W and 51°E. Being the second largest continent on earth, Africa extents to about 30 million km² and borders on the Mediterranean Sea in the north, the Atlantic Ocean in the west, the Indian Ocean in the east and the Red Sea in the northeast. On the whole, the relatively smooth coastline has a length of approximately 28,000 km (Du Bois and Gates, 2014; Jones et al., 2013).



**Figure 3.1:** Major geographical features of Africa (Jones et al., 2013)

Geographically, striking features are the extensive Sahara Desert, the Atlas Mountains in the northwest, the Sahel, which stretches south of the Sahara from Senegal to the Red Sea,

the West African Coast, the Congo Basin, the Great East African Rift Valley and the South African Plateau (see Figure 3.1). Topographically, Africa is divided into a northwestern part tending to lower elevations and a southeastern area dominated by plains and plateaus at about 1000 to 2000 m a.s.l. (Jones et al., 2013).

Since agricultural drought stands in the focal point of this thesis, the following description of the study area is restricted to information on climate conditions, soils, vegetation and land cover.

## 3.2 Climate

Africa is primarily situated between the Tropics of Cancer and Capricorn and, thus, mainly lies within the intertropical zone. Its climate is dominated by the Intertropical Convergence Zone (ITCZ) associated with subtropical high pressure cells on each of the northern and southern sides. As a consequence of the shifting ITCZ, associated convective rainfalls and air transportation from the subtropics to the ITCZ via the Hadley cell, precipitation can be considered a key factor of African climate. Due to its location at the equator, solar radiation over Africa is generally high. Climate conditions across the continent are further influenced by the effect of cool ocean currents, the difference in shape between the north and south as well as the absence of mountain chains as climatic barriers (Jones et al., 2013; Lydolph, 1985).

All in all, Africa consists of areas under arid (57.2 % of surface area), tropical (31.0 %) and temperate (11.8 %) climate. Figure 3.2 displays different climate zones occurring on the continent of Africa according to the Köppen-Geiger classification. The arid climate zone comprises an extensive area under warm desert climate (BWh), smaller regions under cold desert (BWk) as well as warm (BSh) and cold (BSk) semi-arid steppe climate. Major arid regions can be found in the Sahara, the Sahel, the Horn of Africa and south-western Africa (Kalahari Desert). In the dry desert zone, which occupies nearly half of the continent, annual rainfall is erratic with less than 100 mm and temperature shows large daily and seasonal extremes. Semi-arid steppe zones are characterized by an annual rainfall of less than 600 mm, falling exclusively in the summer months. Tropical conditions are located around the equator and are subdivided into equatorial (Af), monsoon (Am) and tropical savannah (As) climate. In this humid to sub-humid zones, annual rainfall ranges from 600 to over 1500 mm. Finally, most of the temperate regions show a dry season either in summer (Mediterranean climate Csa, Csb) or winter (humid subtropical climate Cwa, Cwb) and are mainly located in the northern- and the southernmost areas of Africa (Jones et al., 2013; Peel et al., 2007).

## 3.3 Soils

The distribution of soil types across the African continent is directly linked to its climate zones. Since crop production requires arable land, fertile soils are essential for food security. However, areas meeting this precondition are limited and not distributed evenly across Africa.
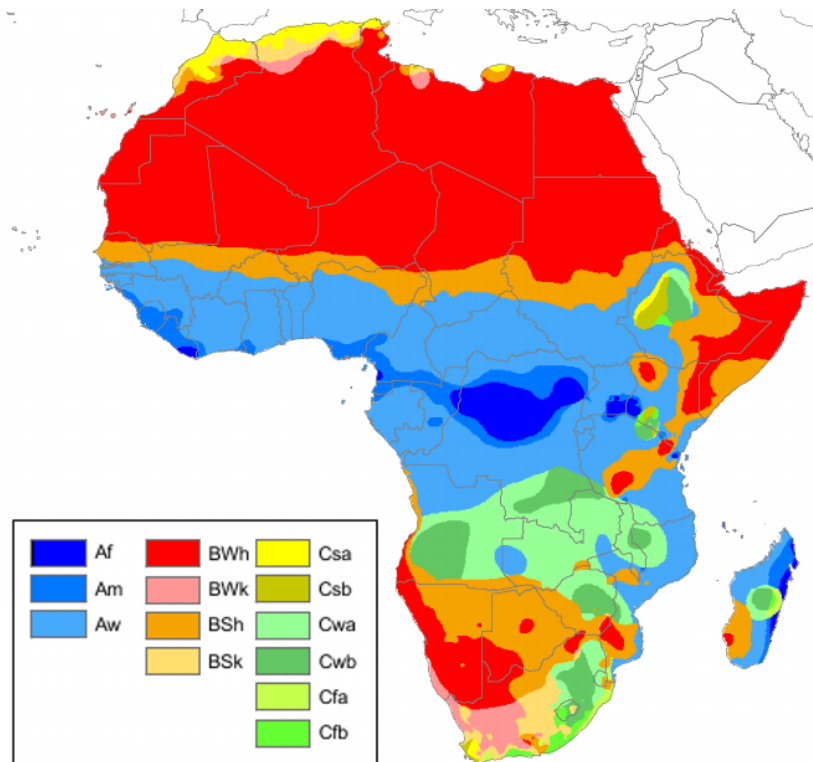
**Figure 3.2:** Köppen-Geiger climate zones of Africa (Peel et al., 2007)
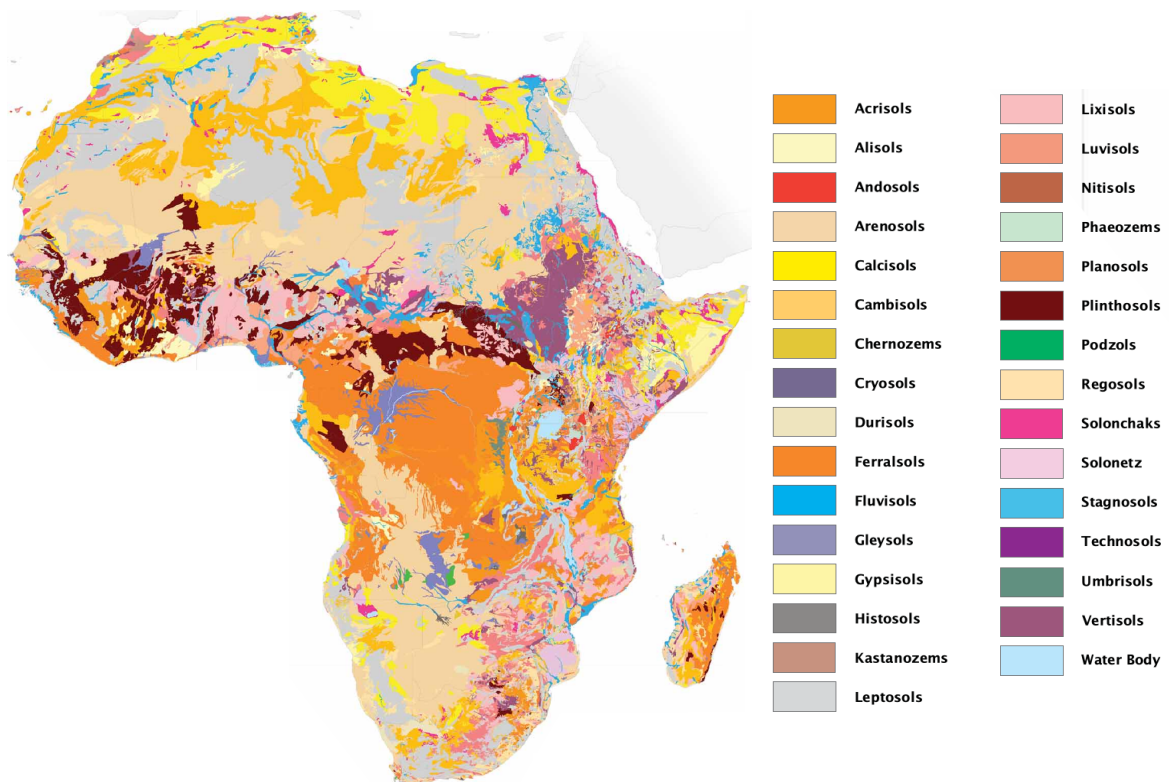


**Figure 3.3:** Major soil types in Africa (Jones et al., 2013)

About 55 % of the African surface area is considered unsuitable for rain-fed agriculture other than nomadic grazing, since climate conditions are too hot and dry, areas are dominated by sandy, weakly developed soils or necessary nutrients are lacking (Jones et al., 2013).

The map in Figure 3.3 shows the zonal arrangement of dominant soil groups in Africa according to World Reference Base for Soil Resources (WRB) of the Food and Agricultural Organization of the United Nations (FAO). Central, wetter regions are mostly covered with Ferralsols, which are further associated with Acrisols. These weathered laterite soils are leached of minerals and generally nutrient-poor. Here, the dominant agricultural land use practice is shifting cultivation, which involves the burning of natural vegetation for nutrient supply. Further, Calcisols, Arenosols and Leptosols dominate the dry desert regions. These soil types exhibit low water-holding capacity and nutrients and, thus, soils around the margins of deserts are often characterized by physical characteristics of acidity, alkalinity, salinity, or erosion and hold low agricultural potential (Jones et al., 2013; UNEP, 2008). Among the most productive soils for agriculture in Africa are Luvisols, Vertisols, Chernozems, Kastanozems and Fluvisols, which possess deep permeable horizons of clayey and loamy texture, provide an adequate nutrient supply and a sufficient water-holding capacity. These soils are ideally suited for agriculture and represent about 10 % of the African farmland, mainly situated south of the Sahel (Senegal, Mali, Burkina Faso, Ghana, Togo, Benin, Nigeria, Chad) and over southern Africa, e.g. in Mozambique, Zambia, Zimbabwe and South Africa (Jones et al., 2013; UNEP, 2008).

## 3.4   Vegetation and land cover

Biomes are characterized as large areas with ecologically similar plant and animal communities and are used for describing Africa's vegetation at a continental scale. In general, forests, savannah, grassland and deserts can be found as major vegetation zones (Jones et al., 2013; UNEP, 2008). The distribution of biomes is determined by rainfall pattern and climate zones. Accordingly, the highest primary productivity and biodiversity is generally found in zones of high annual rainfall, making the equatorial climate zone (Af) the most species-rich region (UNEP, 2008).

Figure 3.4 displays the distribution of biomes over Africa according to UNEP (2008). The Mediterranean biome is situated in northern Africa and along the south-western coast of South Africa. Here, characteristic drought-tolerant and xerophytic plant communities can be found. Within the semi-desert biome, which is regarded a transition zone between savannah and desert areas, short grasses and typical iconic acacias are predominant. Further, plants have developed different strategies in order to conserve moisture during the dry season.

The savannah biomes are the characteristic ecosystem of the African continent. Seasonal precipitation is the dominant climatic force, shaping a vegetation structure that consists of more or less continuous grass cover and trees without closed canopies. Here, frequent fires are important recurrent phenomena during the dry season.

Tropical rain forests are characterized by a layered vegetation, which is dominated by tall trees rising above a very dense canopy of shorter trees, vines and lianes as well as a rather open plant cover nearest the ground. These biome holds the highest biodiversity of all terrestrial ecoregions.
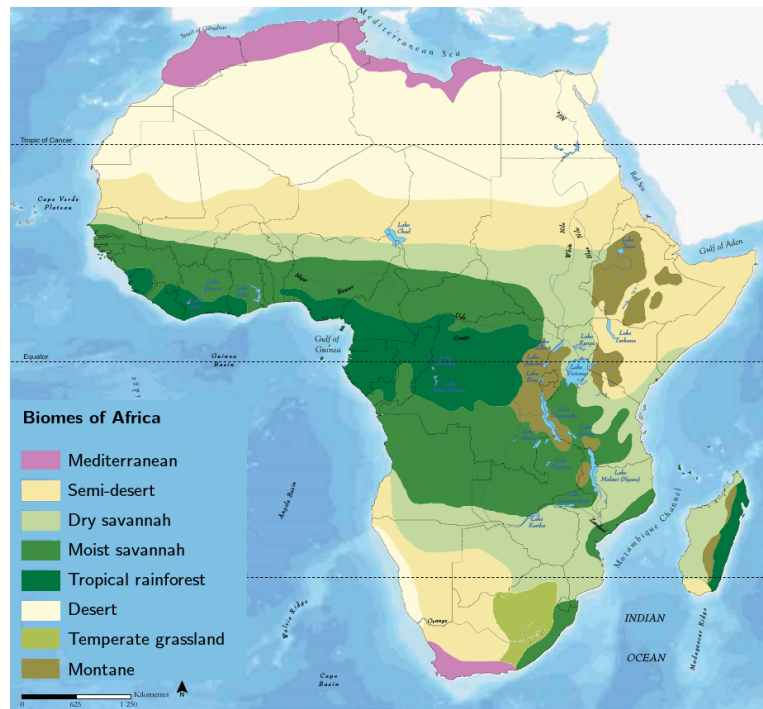
**Figure 3.4:** Biomes of Africa (UNEP, 2008)
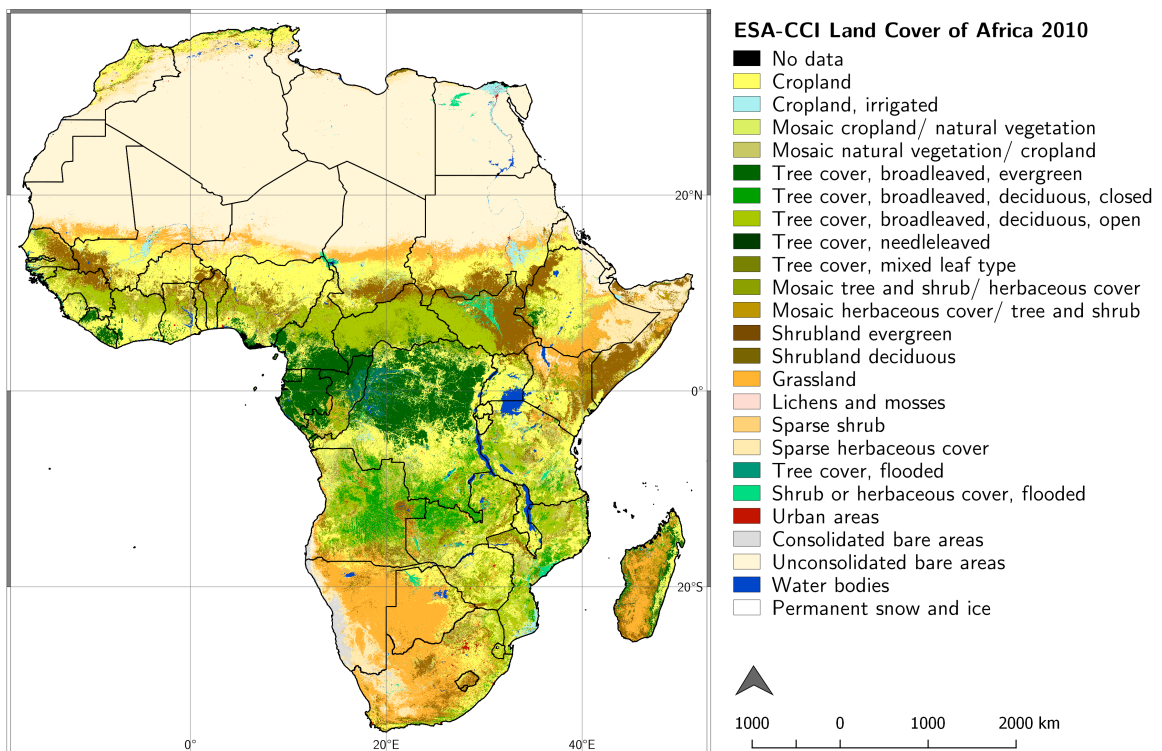


**Figure 3.5:** Land cover of Africa for 2008-2012 (Data source: ESA Climate Change Initiative, 2011)

What is more, the desert biome consists of vegetation highly adapted to precipitation deficits and extreme temperatures. However, biomass is generally very low. A zone of temperate grassland is located in southern Africa, where grasses and scattered trees are prevalent. Montane vegetation is mainly located in the Ethiopian Highlands, the Albertine Rift and the Arc Mountains of eastern Africa. Here, montane forest, bamboo, heather and alpine

tundra can be found from lower to higher elevations (UNEP, 2008).

A more detailed overview of vegetation distribution in Africa provides the land cover map of ESA Climate Change Initiative (2011) for the 5-year period of 2008-2012. Forests within the tropical rainforest and moist savannah biomes are further divided into broadleaved, evergreen and mixed leaf types. Dry savannah areas exhibit grassland and shrubland as major classes of land cover. Further, cropland areas can be found in different biomes, especially in the Mediterranean biome, moist and dry savannah as well as in semi-desert areas.

Land resources of Africa are rapidly changing. This involves human activity, especially transformations of land cover, changes in land use and productivity. This is of high relevance, since a majority of the population of sub-Saharan Africa lives in rural areas and, thus, depends strongly on natural resources (UNEP, 2008).

# Chapter 4

# Data and methods

## 4.1 Methodological overview

In the following sections, the underlying methodology of this thesis is presented, consisting of data acquisition, preprocessing and drought detection based on remote sensing time series analysis.
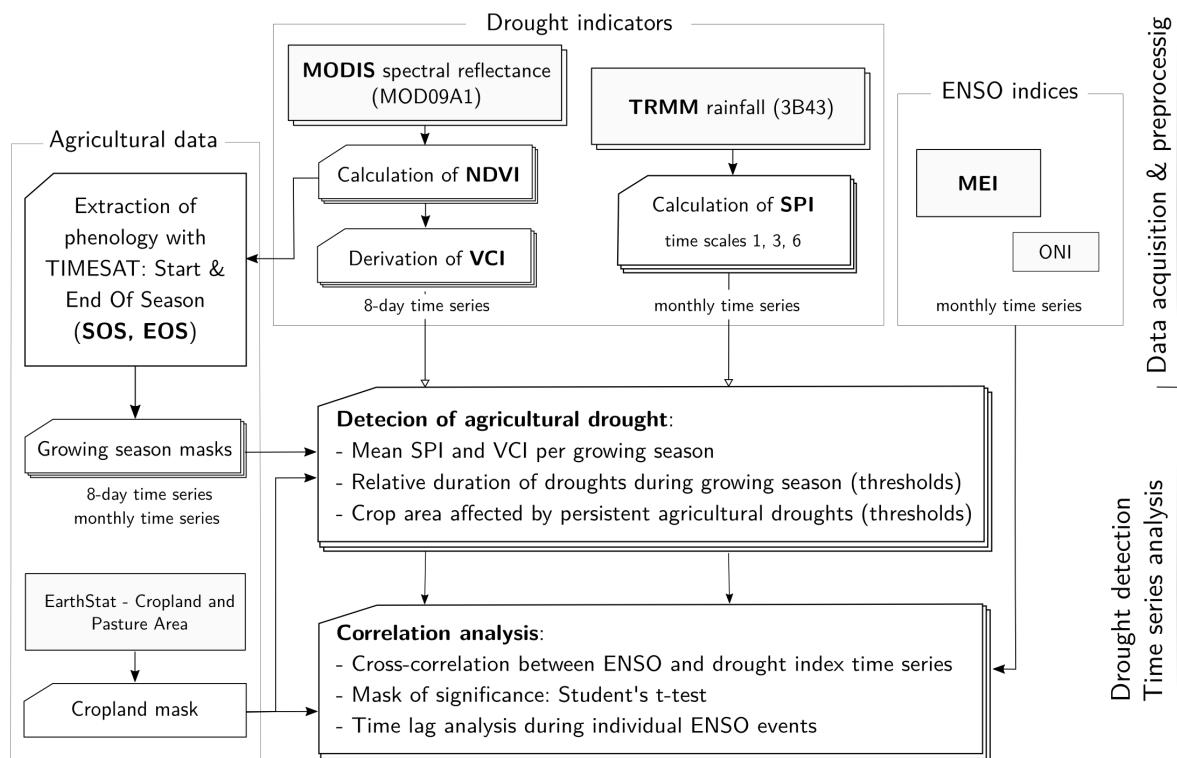


**Figure 4.1:** Schematic overview of methodological approach

Figure 4.1 gives a schematic overview of the major methodological steps. Firstly, remote sensing-based data sets are used in order to derive meteorological and vegetation-based indicators for agricultural drought. Secondly, phenological information is extracted from the temporal vegetation profiles. This is used in order to characterize the average timing and duration of the growing season, which is focussed during subsequent time series processing. Finally, extent, temporal pattern and magnitude of detected droughts are analysed. Drought

index time series are further examined with regard to their relation to ENSO. Hereby, corresponding correlation pattern and the respective time lags are analysed for African agricultural areas.

## 4.2 Data

An overview of used remote sensing-based data sets and the respective specifications is given in Table 4.1.

**Table 4.1:** Used remote sensing-based data sets and its general characteristics

| Dataset | TRMM 3B43 (V7) | MODIS MOD09A1 (V6) | EarthStat Cropland |
|---------|----------------|---------------------|---------------------|
| Variable | Precipitation rate (mm/h) | Surface reflectance | Cropland area fraction |
| Source | TRMM, gauge analysis | MODIS | MODIS, SPOT Vegetation, inventory data |
| Temporal coverage | 1998-01-01 to present | 2000-02-26 to present | 2000 |
| Spatial coverage | 50°S to 50°N | Global | Global |
| Temporal resolution | 1 month | 8 days (composite) | no time series |
| Spatial resolution | 0.25° × 0.25° | 500 m | 5 min |
| Data format | netCDF | HDF | GeoTIFF |

### 4.2.1 Precipitation data

In the present thesis, the TRMM Multisatellite Precipitation Analysis (TMPA) is used in order to assess meteorological drought based on precipitation. This product was chosen due to its successful implementation in numerous Africa-related studies (e.g. Dinku et al., 2007; Herrmann et al., 2005; Naumann et al., 2012, 2014).

Tropical Rainfall Measuring Mission (TRMM) is a joint mission of the National Aeronautics and Space Administration (NASA) of the United States and the National Space Development Agency (NASDA) of Japan with the aim of measuring tropical and subtropical precipitation. Therefore, several precipitation-related sensors, such as the precipitation radar, the TRMM microwave imager and the Visible and Infrared Radiometer System (VIRS) are applied on board (Du et al., 2013). TMPA combines these remotely sensed precipitation estimates with land surface gauge analyses (Huffman et al., 2007). Based on the TMPA algorithm, a level 3 product, 3B43, was generated by Global Precipitation Climatology Center (GPCC) by means of a Huffman's algorithm. It consists of monthly precipitation rates (mm/h) at a spatial resolution of 0.25°×0.25°. Global coverage spans the latitudes from 50°S to 50°N (Du et al., 2013; Huffman et al., 2007).

For this thesis, TRMM 3B43 (Version 7) data from 2000 (March) to 2016 (April) is retrieved in netCDF format (TRMM, 2011). Images are converted to GeoTIFF format (Code SPI-0 in

Table 1 of appendix) and cut to the extent of the study area using the language and software environment R (R Core Team, 2013).

### 4.2.2 Surface reflectance data

Although numerous studies dealing with drought monitoring over large areas are based on AVHRR data, which hold a relatively long temporal record beginning in 1981, this thesis is based on Moderate-resolution Imaging Spectroradiometer (MODIS) data, which is available since February/March 2000. MODIS provides acquisitions with higher spatial resolutions, more spectral channels, geolocation of higher accuracy, and improved atmospheric correction than AVHRR (Townshend and Justice, 2002; Wu et al., 2015).
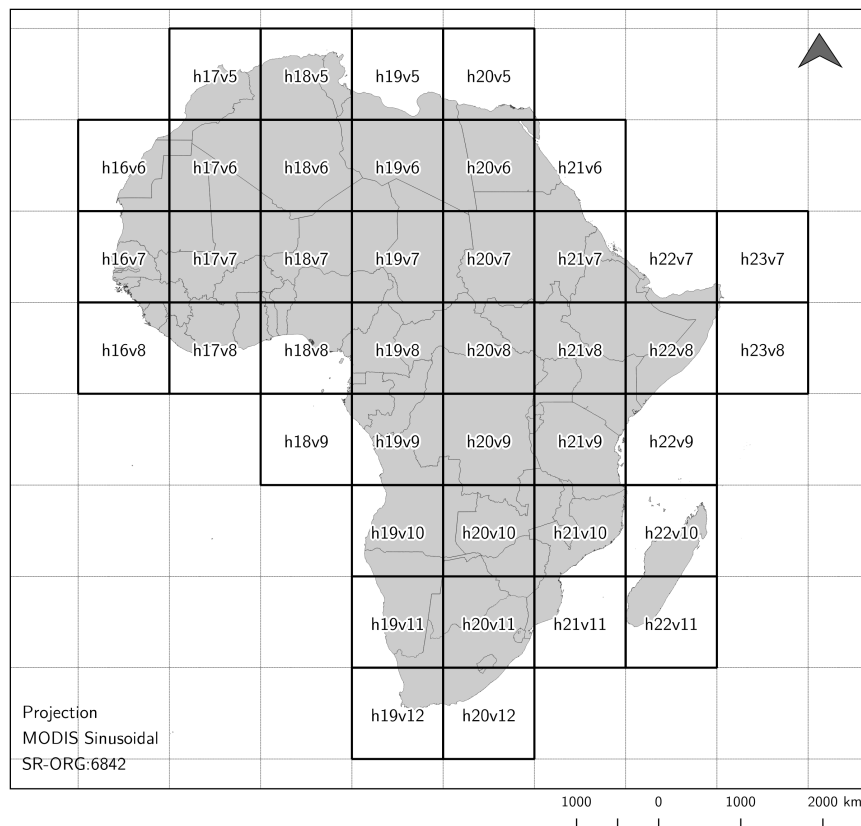


**Figure 4.2:** MODIS granules over Africa

MODIS is a scientific instrument aboard the research satellites Terra and Aqua operated by NASA. It comprises 36 spectral bands with wavelengths ranging from 0.4 to 14.4 $\mu$m (NASA, 2016a). The MOD09A1 Surface Reflectance product from Terra (Vermote, 2015) provides estimates of spectral reflectance of 7 spectral bands with a spatial resolution of 500 m per pixel. Hereby, values are already corrected for the effects of atmospheric scattering and absorption. Terra is an near-polar orbiting satellite, crossing the equator at approximately 10:30 am/pm each day. Data acquired in intervals of 8 days are combined to composites. From all acquisitions within the 8-day composite period, one value is assigned for each pixel as the best possible observation based on several criteria, comprising high coverage, low view angle, the absence of clouds and aerosol loading (Choi et al., 2013; Sánchez et al., 2016).

29

In the present thesis, MOD09A1 Surface Reflectance data are retrieved for 41 granules covering the African continent (see Figure 4.2). The 8-daily images with a spatial resolution of 500 m are downloaded for the study period of 2000 (February 26) to 2016 (April 30) in HDF format, which provided a data base of $748 \times 41$ image files.

### 4.2.3    ENSO indices

Multivariate ENSO Index (MEI) is used as primary ENSO index in this thesis, since it integrates more information than other indices and incorporates multiple parameters of the coupled ocean-atmosphere system (see Section 2.3.2). The data set is retrieved in form of a table containing bimonthly values. Hereby, each value is assigned to its last corresponding month (NOAA, 2016b). In order to identify months within categorized El Niño or La Niña periods, the standard definition based on Oceanic Niño Index (ONI) is used. Accordingly, an ENSO warm (cold) phase is characterized by five consecutive months showing ONI values above 0.5°C (below -0.5°). For further information on ONI, see Section 2.3.2.

### 4.2.4    Ancillary data

With regard to agricultural areas, the EarthStat data set on global crop and pasture areas 2000 is used in this thesis (EarthStat, 2008). This data product is based on a combination of satellite-based land cover classifications, a MODIS-derived global land cover product from Boston University and Satellite Pour l'Observation de la Terre (SPOT) VEGETATION-based Global Land Cover 2000 (GLC2000) with additional agricultural inventory data. Gridded cropland and pasture area fraction data are available at spatial resolutions of 5 min (about 10 km; Ramankutty et al., 2008). The 10 km grids contain information on sub-pixel fractions of cropland and pasture, respectively. In this thesis, only cropland information is used for the detection of agricultural droughts. Data is downloaded in GeoTIFF format and cut to the extent of the study area. Image pixels where the fraction of cropland area exceeds zero are included into the applied drought analysis, whereas pixels without cropland are masked. This represents a rather broad crop mask, since it includes all areas where cropland is present at any percentage. Thus, mixtures of cropland with other land use types and possible land use changes may influence the detection of agricultural droughts.

Further, for mapping drought-related results and regional analysis, an openly available data set of administrative boundaries is acquired from the database of Global Administrative Areas (GADM, 2015) in shapefile format. Only those GADM lying within the study area are extracted, containing administrative divisions of level 0 and level 1.

In order to examine the effect of detected droughts on national agricultural production within the focal regions, yearly crop statistics from the FAOSTAT database (FAO, 2016b) are acquired. The FAOSTAT data set aims to comprehensively cover production of primary crops for all countries and regions in the world (FAO, 2016b). Here, focus is laid on primary crops containing vegetables, fruits, treenuts, cereals, pulses, roots and tubers, fibre crops and oil crops. Respective production quantity data are retrieved for 2000-2013 (Table 2 in appendix).

## 4.3 Derivation of drought indices

### 4.3.1 Standardized Precipitation Index (SPI)

As a meteorological drought indicator, Standardized Precipitation Index (SPI) is used in this thesis, since it has been selected as a key indicator for global drought monitoring by the World Meteorological Organization (WMO) and successfully implemented into multiple drought monitoring approaches (e.g. Awange et al., 2016b; Naumann et al., 2012, 2014; Ntale and Gan, 2003). Monthly SPI is derived for 1-, 3-, and 6-monthly aggregated TRMM precipitation data using R (Code SPI-1 in Table 1 of appendix).

Firstly, based on gridded monthly TRMM rainfall images, sums are calculated over each of the accumulation periods of 1, 3 and 6 months for each pixel in order to provide a monthly SPI output that corresponds to different temporal scales of drought. As a first step of the SPI algorithm, accumulated rainfall data are analysed for each pixel in order to estimate the two key coefficients for a subsequent transformation of the observed frequency distribution to a gamma distribution via maximum likelihood estimation. For instance, the transformation of the 3-monthly accumulated precipitation value of June 2000 into SPI values relies on the available data record for the periods containing the same three months (16 observations from 2000 to 2015 ). The gamma distribution is chosen in order to reliably respond to the known asymmetrical frequency distribution of precipitation, since, in a typical record of rainfall totals, most of the occurrences are found at low values, whereas larger values occur with rapidly decreasing likelihoods (Keyantash and NCAR, 2016).
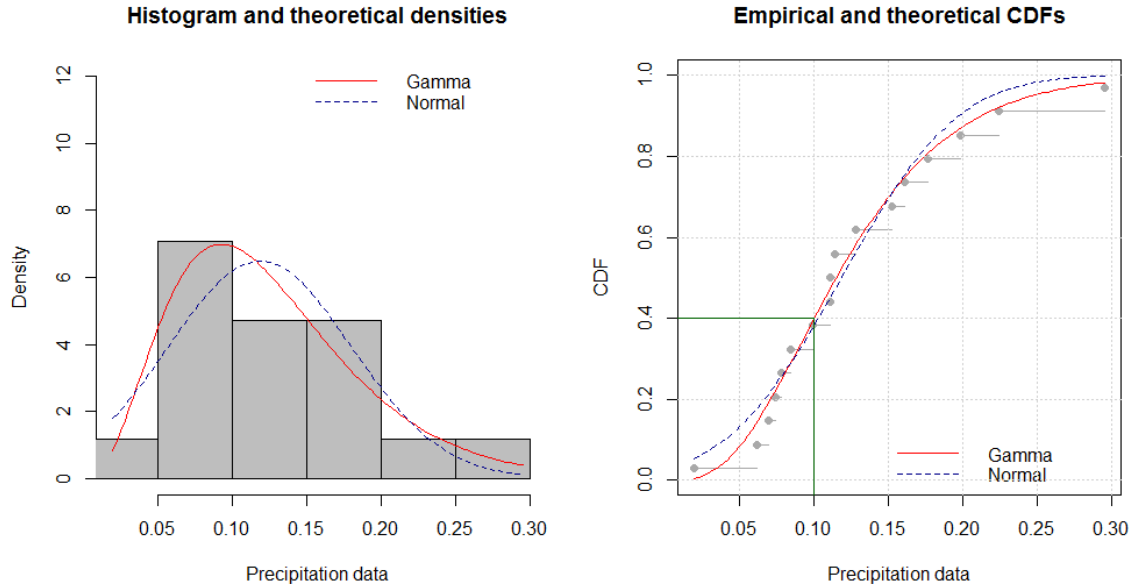


**Figure 4.3:** Comparison of empirical distribution with fitted gamma and normal distribution for TRMM 3B43 precipitation values for March (1-monthly aggregation) 2000-2016 of an exemplary pixel at 16.36°S 34.05°E. Left: Histogram and density functions, right: Cumulative density function

This is shown in Figure 4.3, which displays the distribution of an exemplary precipitation record for a randomly chosen pixel (16.36°S 34.05°E: Moatize, Mozambique) within the used

data set and compares its empirical density with two theoretical density functions. Accordingly, gamma distribution provides a better fit than normal distribution. Fitting the data to gamma distribution

$$g(x_k) = \frac{1}{\beta^\alpha \Gamma(\alpha)} x_k^{\alpha-1} e^{-x_k/\beta} \, for: \; x_k > 0 \tag{4.1}$$

with $\alpha > 0$ as shape and $\beta$ as scale factor, $x_k > 0$ as the amount of precipitation over $k$ consecutive months and $\Gamma(\alpha)$ as the gamma function

$$\Gamma(\alpha) = \int_0^\infty y^{\alpha-1} e^{-y} dy \tag{4.2}$$

includes the estimation of $\alpha$ and $\beta$ via Maximum Likelihood Estimation (Asadi Zarch et al., 2015). Afterwards, precipitation values are transformed to normally distributed SPI values via the respective cumulative probability value (i.e. green lines in Figures 4.3 and 4.4).
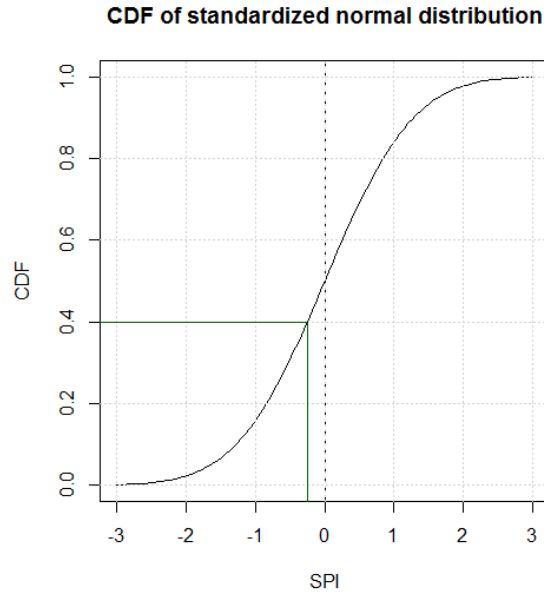


**Figure 4.4:** CDF of normal distribution for the range of SPI values. CDF values of gamma (see Figure 4.3) and normal distribution are matched in order to derive SPI values from given precipitation.

Finally, the SPI is described as follows:

$$SPI = \frac{P - P^*}{\sigma_P} \tag{4.3}$$

where $P$ is the aggregated precipitation for a certain time interval, $P^*$ is the respective mean and $\sigma_P$ represents the standard deviation over the available data record for the studied interval (Keyantash and NCAR, 2016). Accordingly, the resulting dimensionless SPI has its mean at 0 and represents the anomaly of observed rainfall relative to the recorded precipitation time series, which is expressed in standard deviation units. This calculation procedure is carried out for each pixel and all layers of the precipitation raster stack, where each layer represents the aggregated rainfall value for a certain month. For each of the aggregation intervals, monthly SPI images are generated (SPI-1, SPI-3, SPI-6). Although three different aggregation levels

were produced, focus was lain on 3-monthly aggregated SPI (SPI-3) for further analyses, since it represents a seasonal-scale precipitation deficit. The latter is regarded a direct cause for agricultural drought and, thus, reflects soil moisture conditions essential for agricultural activities (WMO, 2012). For selected locations of the focal regions, SPI additionally was computed as a function of both time and aggregation level (1- to 12-monthly time scales) to give an insight into the propagating patterns of droughts on different time scales (see appendix, Figure 2).

### 4.3.2 Vegetation Condition Index (VCI)

NDVI and VCI are derived from 8-days composites of MODIS spectral reflectance using Interactive Data Language (IDL) (Code VCI-0 in Table 1 of appendix). Spectral reflectance values of bands 1 and 2 are extracted by iterating through all available raw MODIS images. These bands cover the RED and NIR spectral domain, respectively, and are needed for calculating the NDVI (see Section 2.3.1.4). Subsequently, NDVI values are computed according to equation 2.1.
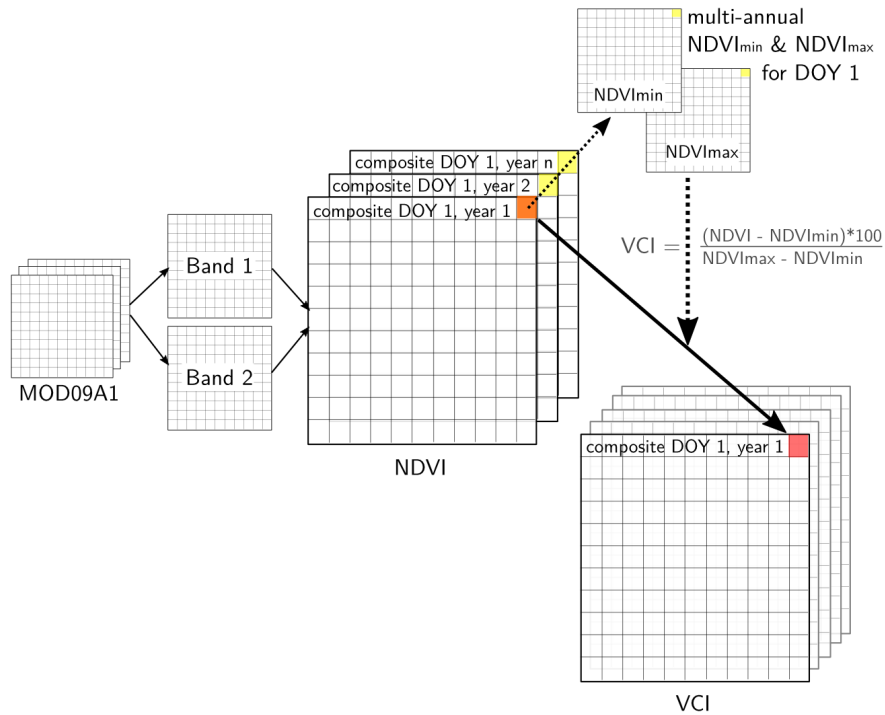


**Figure 4.5:** Workflow of the performed derivation of VCI for an example composite. Coloured cell values are incorporated into the calculation: orange = current NDVI value, yellow = values of NDVI time series with respective maximum and minimum, red = resulting VCI value

Based on the generated 8-daily NDVI time series, VCI is derived. The methodology depends on computed minimum and maximum NDVI for each of the 46 composites within a year. As an example, NDVI extrema for Day Of Year (DOY) 1 refer to all acquisitions on the first day of year during the studied time period (16 observations between Feb/March 2000 and April 2016). Thereupon, the VCI is derived according to equation 2.2. Figure 4.5 contains an illustration of the necessary steps for calculating NDVI and VCI from MODIS spectral reflectance time series. Hereby, the current NDVI value is scaled against the difference between maximum

and minimum NDVI for the considered time of acquisition (here: DOY 1). Consequently, a time series of both NDVI and VCI images is derived from MODIS spectral reflectance data.

## 4.4 Detection of agricultural drought

### 4.4.1 Extraction of average growing season

In order to assess agricultural droughts, phenological information is retrieved from the previously generated NDVI time series. For this purpose, the software package TIMESAT 3.2 is used (Eklundh and Jönsson, 2015). The timing of growing season is determined for each pixel based on an average NDVI time series during the course of the year, which is retrieved from the available data record.
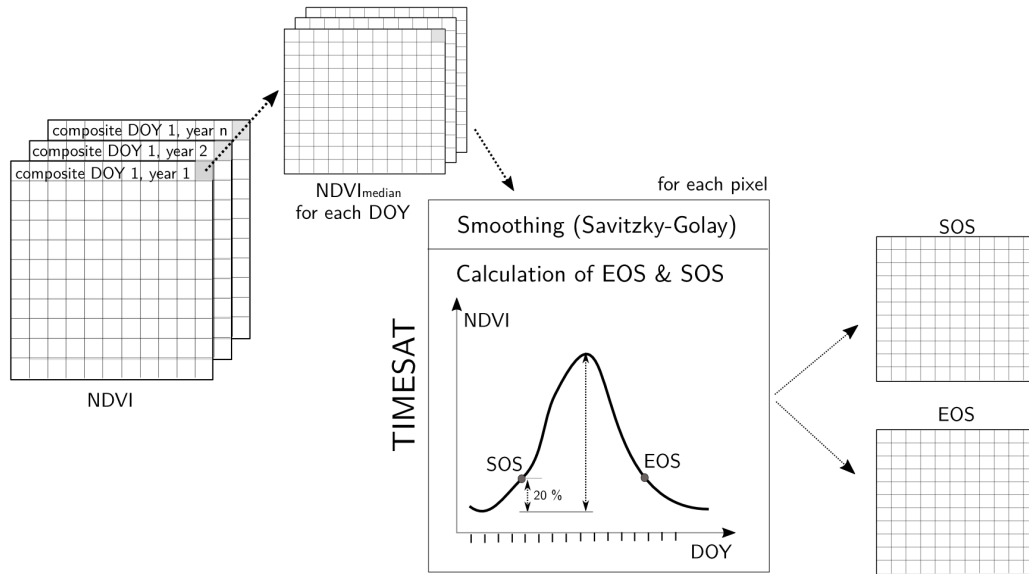


**Figure 4.6:** Schematical flowchart of the extraction of the average growing season from MODIS-derived NDVI time series by means of TIMESAT (SOS: Start of Season, EOS: End of Season, DOY: Day of Year)

As a first step, the median is derived for each DOY through the available NDVI time series from 2000 to 2016 (Code PH-1 in Table 1 of appendix). The resulting 46 raster images of median NDVI resemble the average distribution of NDVI throughout the year and are thereupon used as input data for the TIMESAT procedure. Because of special processing requirements, the input median NDVI files are copied twice so that an artificial time series is generated, spanning 3 years. Subsequently, this median NDVI time series is smoothed for each pixel applying the Savitzky-Golay filter with a window size of 4 (Savitzky and Golay, 1964). A seasonal parameter of 0 is defined in order to include areas with bimodal rainy seasons. For deriving the timing of the growing season, a temporal window is specified. This time span was set from DOY 241 of the first year to the end (DOY 361) of the second year of the artificial 3-year time series in order to include growing seasons which start before and end after the turn of the year. The detection captures up to two growing seasons, lying completely within the time window. Dates of Start Of Season (SOS) and End Of Season (EOS) are extracted.

Hereby, SOS and EOS are defined as 0.2 of the amplitude (see example in Figure 4.6). The output files of SOS and EOS indices are transformed from binary values into both months and days of year, which are used for the detection of agricultural droughts (Code DD-0 in Table 1 of appendix). Dates lying within the previous year, are stored as negative values (e.g. SOS of months -2 refers to November of previous year).

### 4.4.2 Drought detection during average growing season

#### 4.4.2.1 Continental-scale drought detection

In order to quantify the strength and duration of agricultural droughts over Africa for each seasonal year, statistical and threshold-based parameters are derived from time series of 3-monthly accumulated SPI (SPI-3) and VCI . Hereby, a seasonal year starts at DOY 241 of the corresponding previous year (see Section 4.4.1). In this case, the meteorologically originated SPI-3 is regarded an index for agricultural drought, since the accumulation period of 3 months can be associated with soil moisture response to rainfall.

First of all, SPI images are reprojected and resampled to the same spatial grid as MODIS-derived SOS and EOS images using Python and Geospatial Data Abstraction Library (GDAL) for reprojecting and IDL for adapting the spatial grid (Codes PR-1 and PR-2 in Table 1 of appendix).
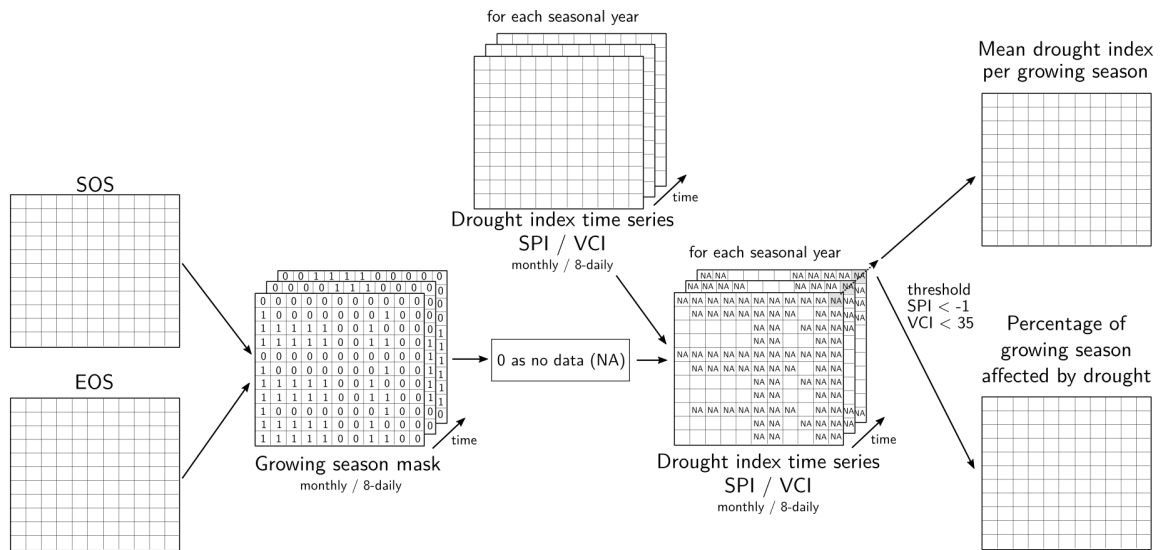


**Figure 4.7:** Schematical flowchart of the detection of agricultural droughts for each seasonal year based on drought index time series (SOS: Start Of Season, EOS: End Of Season)

The SOS and EOS data set indicates for each pixel the average timing and duration of the growing season. Based on this information, the number of observations under drought conditions is extracted by using defined thresholds for both drought indices. This was done using IDL procedures (Codes DD-1 and DD-2 in Table 1 of appendix).

In this thesis, SPI is categorized based on the classification of WMO, 2012, which is outlined in Table 4.2. Accordingly, a threshold of -1 was used for SPI, with values below the threshold representing moderate to extreme drought conditions. With respect to VCI , Kogan (1995)

**Table 4.2:** Drought categories based on SPI (WMO, 2012) and VCI (Klisch and Atzberger, 2016)

| Drought category | SPI range | VCI range [%] |
|---|---|---|
| Extreme drought | $SPI \leq -2$ | $VCI < 10$ |
| Severe drought | $-2 < SPI \leq -1.5$ | $10 \leq VCI \leq 20$ |
| Moderate drought | $-1.5 < SPI \leq -1$ | $20 < VCI < 35$ |
| No drought | $SPI > -1$ | $VCI \geq 35$ |

proposed a threshold of 35 % for classifying drought. This classification is widely adopted by the drought monitoring community (Deng et al., 2013; Gebrehiwot et al., 2011). Accordingly, a drought classification stated by Klisch and Atzberger (2016) is applied for VCI (see Table 4.2). The 35 % threshold was used, including moderate to extreme drought conditions. Consequently, all observations below the mentioned thresholds are counted and related to the average duration of the growing season for each pixel. A parameter of relative duration of drought conditions during each seasonal year is produced, representing the percental duration of growing season affected by drought (see Figure 4.7). This procedure is applied for each of the drought indices separately.

#### 4.4.2.2   Regional-scale drought detection

Duration and extent of agricultural droughts in the selected focal regions of southern and eastern Africa are further assessed by means of statistical analyses in QGIS. For each region, one drought-affected seasonal year is specified: 2002/03 for southern Africa and 2010/11 for eastern Africa. Figure 4.8 gives an overview of applied GIS analyses including vector-based intersections and the derivation of statistics.
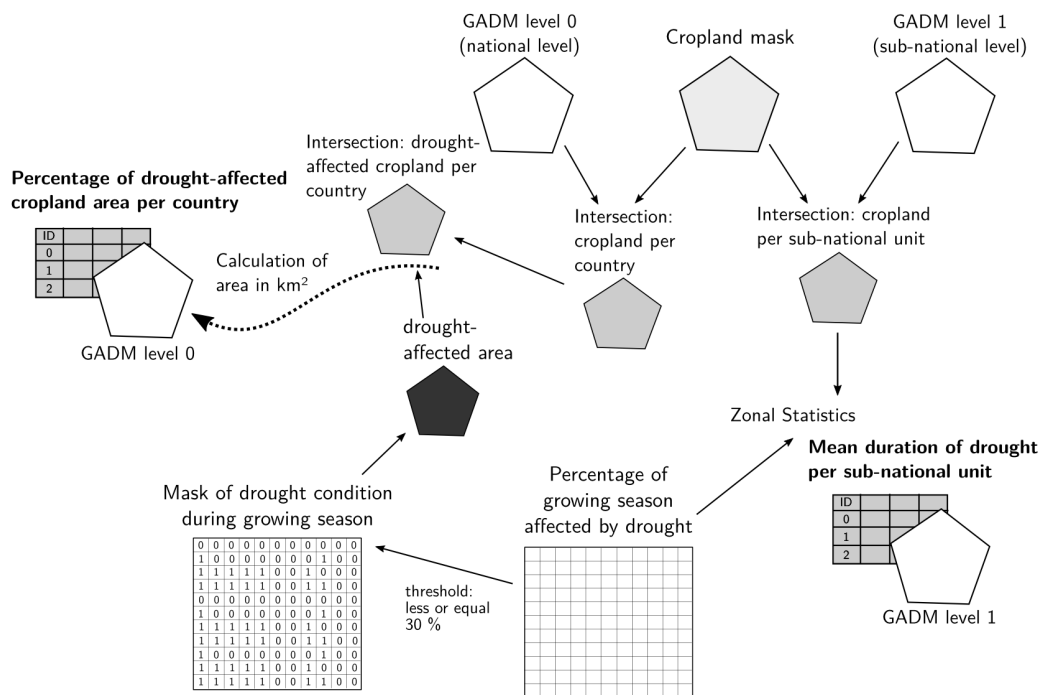


**Figure 4.8:** Schematic flowchart of regional-scale drought detection and vector-based GIS analysis

Relative duration of agricultural droughts is derived for administrative units at sub-national level (level 1 of GADM). Hereby, GADM level 1 polygons are intersected with the used Earth-Stat (2008)-derived crop mask. Based on the resulting areas, which comprise the cropland area per administrative unit, the mean relative drought duration for the selected seasonal year is derived (see Section 4.4.2.1). For this purpose, zonal statistics plugin for QGIS is used. The resulting values represent the mean relative duration of drought related to the growing season over all cropland areas within the corresponding administrative unit.

What is more, the percentage of drought-affected cropland is assessed at national level both of the selected regions and seasonal years. As a first step, the crop mask layer is intersected with GADM level 0 (national level) polygons and, subsequently, the area of cropland (in $km^2$) is calculated for each country. Secondly, drought-affected areas are defined on a pixel bases when droughts were detected for at least 30 % of the growing season. These drought-affected pixels are intersected with cropland area per country and, thereupon, the area of drought-affected cropland (in $km^2$) is calculated for each country. Finally, for each country, the percentage of total cropland areas affected by drought during the focus years is calculated.

## 4.5 Correlation analysis

### 4.5.1 Cross-correlation of drought indices and ENSO index

For assessing the general relation between ENSO and agricultural drought over Africa, cross-correlations are applied between MEI as an ENSO index and each of the drought indices SPI and VCI . For this analysis, monthly means are derived for the complete time series of 8-daily VCI images using Python (Code CC-01 in Table 1 of appendix).

The cross-correlation analysis is implemented in IDL procedures (Codes CC-02, CC-1 and CC-2 in Table 1 of appendix) and was carried out with varying temporal lags. Hereby, all lags between -6 to +6 months are tested. The drought index time series is shifted against the MEI time series by the respective amount of months. Subsequently, the cross-correlation $P_{xy}(L)$ of two sample populations (time series) $X$ and $Y$ is calculated as a function of the lag $L$:

$$P_{xy}(L) = \begin{cases} \dfrac{\sum\limits_{k=0}^{N-|L|-1}(x_{k+|L|}-\bar{x})(y_k-\bar{y})}{\sqrt{\left[\sum\limits_{k=0}^{N-1}(x_k-\bar{x})^2\right]\left[\sum\limits_{k=0}^{N-1}(y_k-\bar{y})^2\right]}} & for\ L < 0 \\[30pt] \dfrac{\sum\limits_{k=0}^{N-|L|-1}(x_k-\bar{x})(y_{k+L}-\bar{y})}{\sqrt{\left[\sum\limits_{k=0}^{N-1}(x_k-\bar{x})^2\right]\left[\sum\limits_{k=0}^{N-1}(y_k-\bar{y})^2\right]}} & for\ L \geq 0 \end{cases} \qquad (4.4)$$

where $\bar{x}$ and $\bar{y}$ denote the means of the sample populations $x = (x_0, x_1, x_2, ..., x_{N-1})$ and $y = (y_0, y_1, y_2, ..., y_{N-1})$, respectively (Exelis Visual Information Solutions, 2016). This procedure is applied for correlating 3-monthly aggregated SPI-3 with MEI as well as VCI with MEI. Figure 4.9 displays the positions of shifted time series for one exemplary month 0 with no time lag (center), a lag of -3 (left) and +3 (right).

37
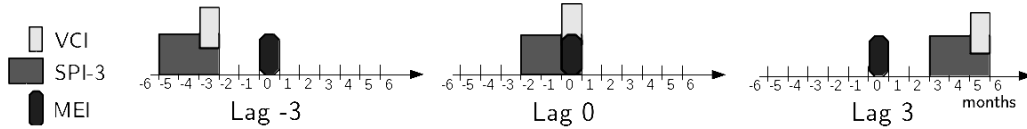
**Figure 4.9:** Set-up for correlation analysis with shifted time lags (left: negative shift, middle: no shift, right: positive shift)

Apart from calculating the correlation coefficients between the two time series, a student's t-test is carried out in order to test for significance. Critical values for the correlation were calculated at the 95 % level of significance. Accordingly, for each time lag, a significance mask is derived, indicating if a pixel yields significant (value 1) or unsignificant (value 0) cross-correlation between the time series of the respective drought index and MEI. Finally, the lag and the value of the maximum correlation coefficients per pixel are extracted by using Python (Code CC-3 in Table 1 of appendix).

### 4.5.2 Time lag analysis for selected ENSO events

What is more, with the aim of studying the relation between drought and ENSO, temporal response times between minima of drought indices and peaks (El Niño) or minima (La Niña) of MEI are analysed for each of the major ENSO events within the studied time period (Codes TR-1 and TR-2 in Table 1 of appendix). ENSO warm and cold phases are selected from MEI time series based on the standard ONI thresholds (see Section 2.3.2). MEI values are compared with SPI-3 and monthly means of VCI, respectively. Firstly, the month with maximum or minimum MEI is identified according to the studied ENSO event. Months of drought index minima are extracted for up to 6 months after the MEI extremum. Finally, the temporal difference and, additionally, corresponding minimum drought index value are retrieved for each pixel. Figure 4.10 visualizes this procedure for an exemplary pixel in the case of El Niño.
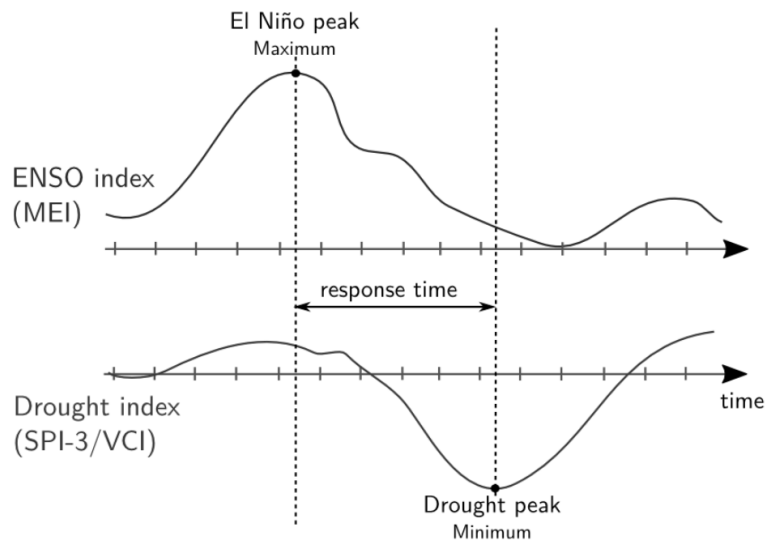


**Figure 4.10:** Example of response time analysis for El Niño: Difference between months of ENSO peak and drought peak (minimum of drought index)

# Chapter 5

# Results

## 5.1 Timing of average growing season

As a first result, the start (SOS) and end (EOS) of the average growing season was derived from multi-annual (2000-2016) MODIS-based median NDVI time series. Months of SOS and EOS are displayed in Figure 5.1. The derived timing of the growing season provides the basis for further analyses of agricultural drought.
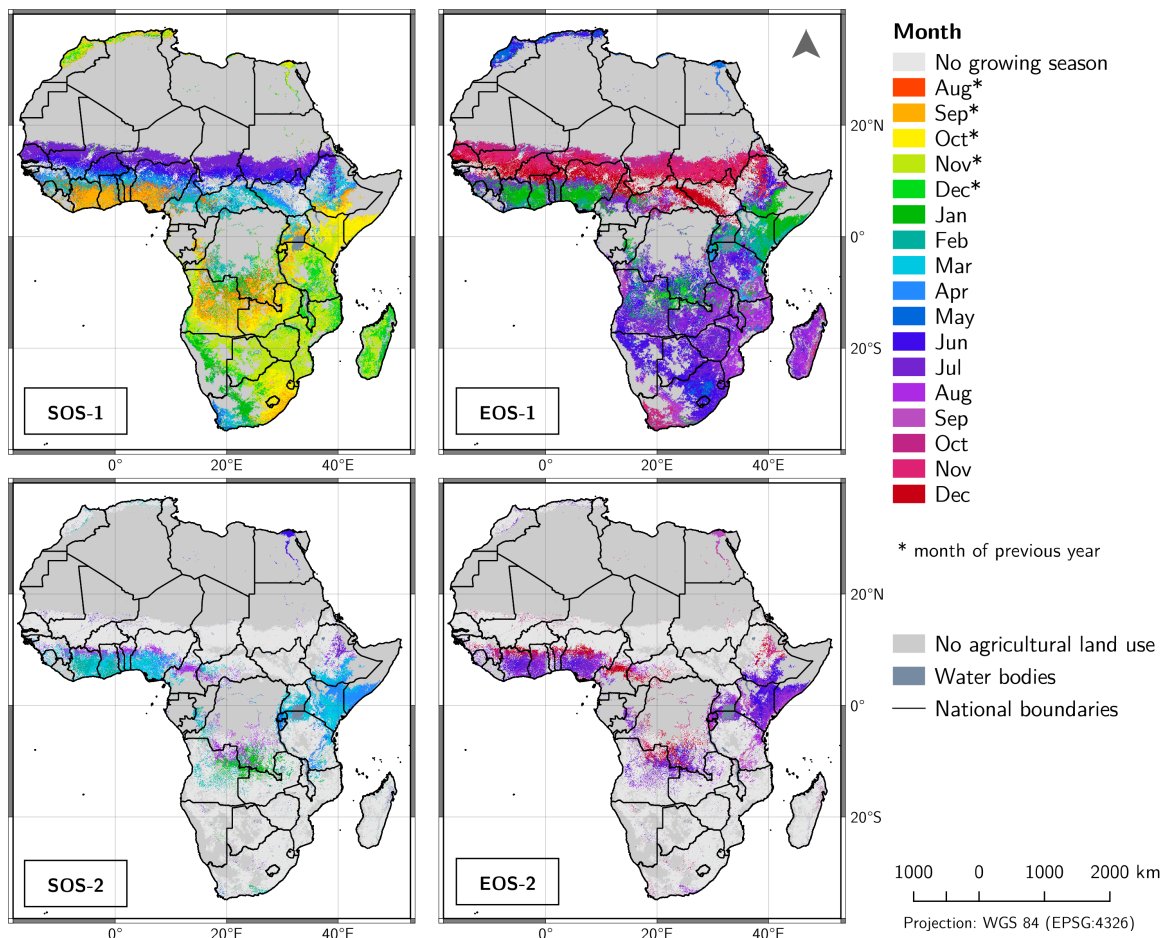


**Figure 5.1:** Start and end of detected growing seasons within the average seasonal year (SOS-1/SOS-2: start of first/second growing season; EOS-1/EOS-2: end of first/second growing season)
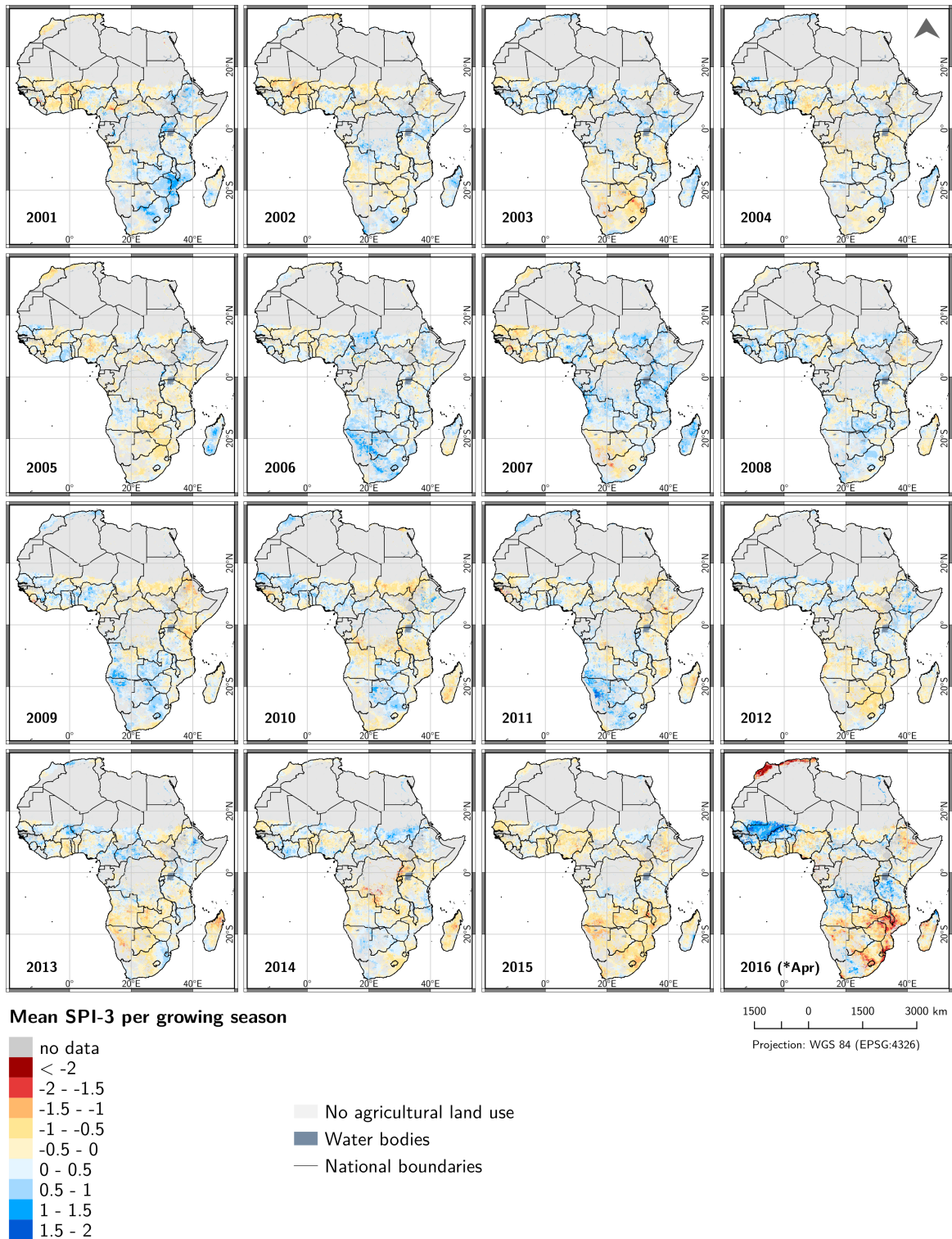
**Figure 5.2:** Mean SPI-3 during growing seasons from 2001 to 2016 (seasonal years)

Due to the zonally graduated distribution of precipitation and climate zones across the African continent, growing seasons show spatially varying lengths and differing timing within the average seasonal year. Whereas the Sahel region exhibits a rather short growing season of about 3-5 months, some regions under tropical climatic conditions show growing seasons spanning more than 10 months, e.g. parts of Zambia, Zimbabwe and Mozambique. Further, a bimodal distribution, where two growing seasons occur within one seasonal year, can be

**Mean VCI per growing season [%]**

| | |
|---|---|
| | no data |
| | 0 - 10 |
| | 10 - 20 |
| | 20 - 30 |
| | 30 - 40 |
| | 40 - 50 |
| | 50 - 60 |
| | 60 - 70 |
| | 70 - 80 |
| | 80 - 90 |
| | 90 - 100 |

No agricultural land use

Water bodies

National boundaries

Projection: WGS 84 (EPSG 4326)

**Figure 5.3:** Mean VCI during growing seasons from 2001 to 2016 (seasonal years)

identified in the Nile delta, parts of West Africa (e.g. Ivory Coast, Ghana, Togo, Benin, southern Nigeria) and eastern Africa, especially in south-western Ethiopia, Kenya, Somalia, Uganda, Rwanda and Burundi (see figure 5.1, bottom).

**Percentage of growing season affected by drought**

Drought conditions are defined as SPI below -1.

no growing season
0 - 10
10 - 20
20 - 30
30 - 40
40 - 50
50 - 60
60 - 70
70 - 80
80 - 90
90 - 100

No agricultural land use
Water bodies
National boundaries

1500    0    1500    3000 km

Projection: WGS 84 (EPSG:4326)
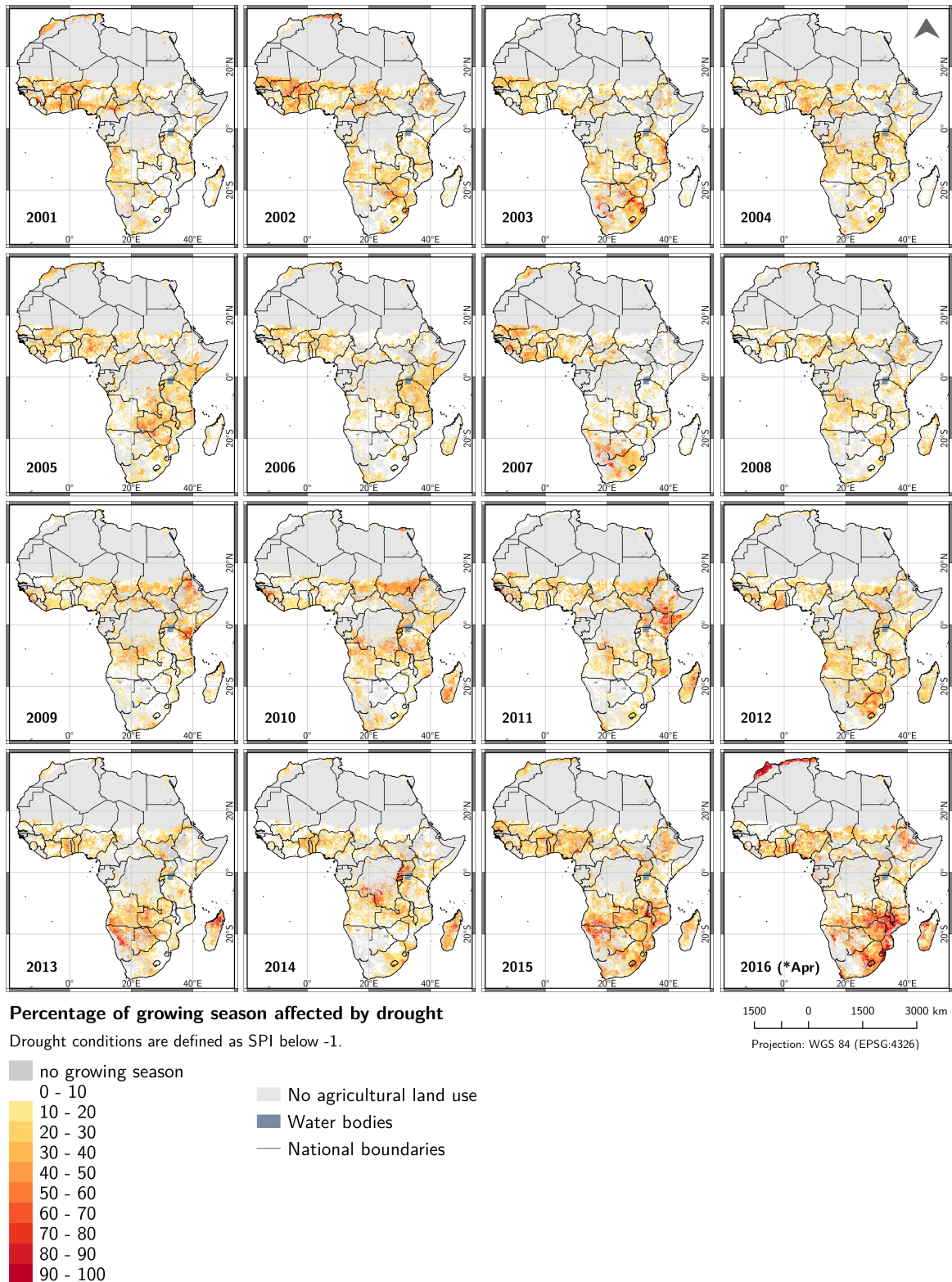
**Figure 5.4:** Relative duration of drought: Percentage of growing season affected by drought events (SPI-3 below -1) from 2001 to 2016 (seasonal years)

## 5.2   Spatio-temporal pattern of agricultural drought

The spatio-temporal pattern of agricultural drought events over Africa is displayed through the means of the drought indices SPI-3 and VCI (referred to as drought severity) as well as the relative duration of drought conditions defined by SPI-3- and VCI-based thresholds
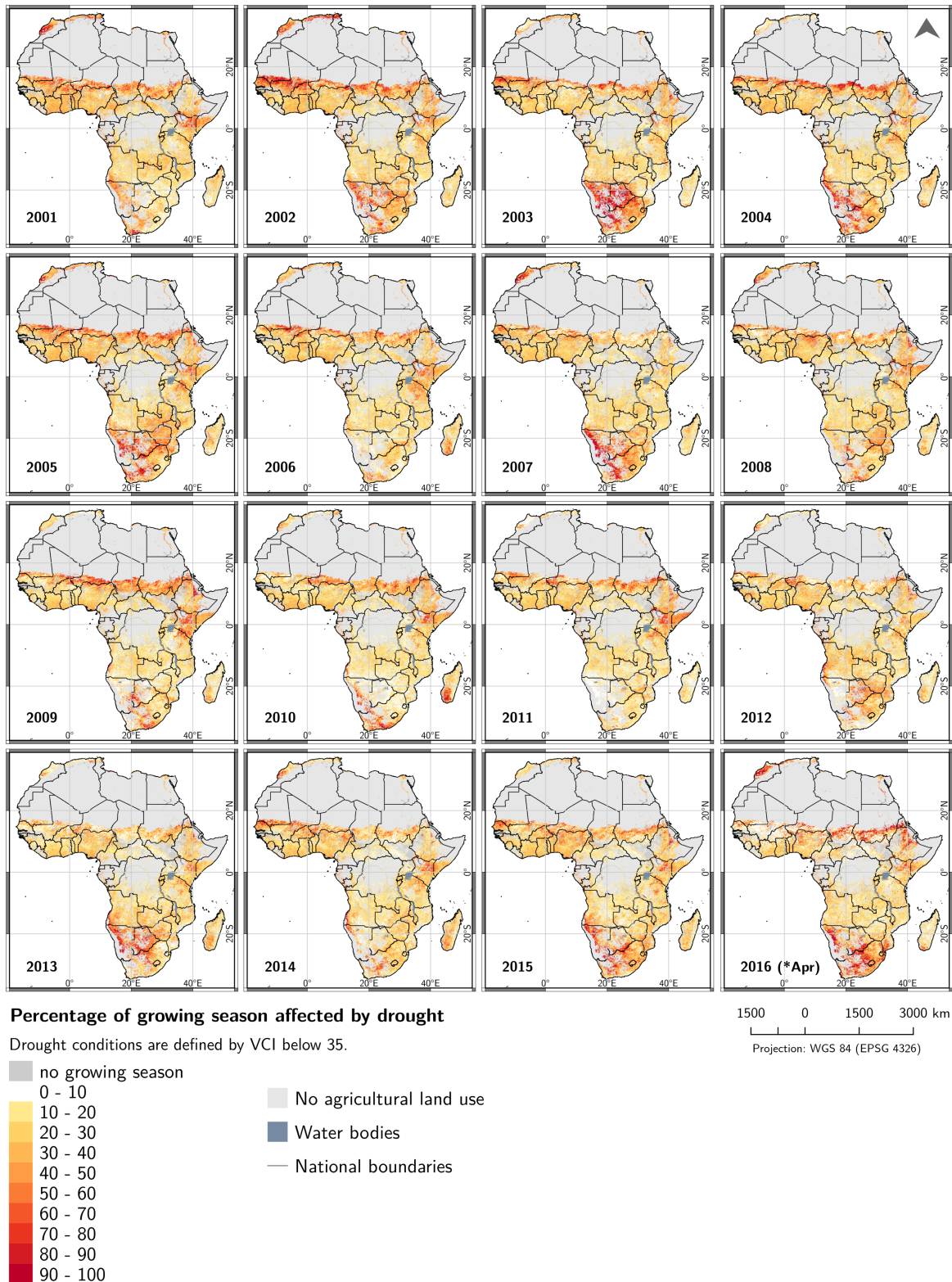
**Figure 5.5:** Relative duration of drought: Percentage of growing season affected by drought events (VCI below 35) from 2001 to 2016 (seasonal years)

during the average growing season. Figure 5.2 and 5.3 present SPI-3- and VCI-based drought severities during each growing season from 2001 to 2016, whereas Figure 5.4 and 5.5 show the temporal dimension of drought for the same period. This relative duration of droughts refers to SPI-3 below -1 and for VCI below 35, respectively. All in all, a temporally and

**Table 5.1:** Seasonal years and countries of focal regions affected by extensive agricultural droughts based on drought indices SPI-3 (Figure 5.2 and 5.4) and VCI (Figure 5.3 and 5.5)

| Region | Years | Countries* affected by drought based on: | | | |
|---|---|---|---|---|---|
| | | Mean SPI-3 | Mean VCI | Relative duration (SPI-3 < -1) | Relative duration (VCI < 35) |
| Eastern Africa | 2000/01 | SO SD SS | KE SD SO | BI SO SS | KE SD SO SS |
| | 2001/02 | ET SD | ER ET KE SD | ER ET SD | ER ET KE SD |
| | 2002/03 | BI RW TA | ER ET SD | BI ET RW TA | ET SD |
| | 2003/04 | BI KE SD TA UG | ER ET KE SD | BI RW SD TA | KE SD |
| | 2004/05 | BI KE SD SO SS TA UG | ER ET KE SD TA | BI KE SO SS TA | ER ET KE SD SO SS |
| | 2005/06 | ET KE | ER KE SD TA | BI ET KE RW SO TA | KE SD SO TA |
| | 2006/07 | ET | ET SD | | ET KE |
| | 2007/08 | ET TA | ET KE SO | ER ET | ET KE SO |
| | 2008/09 | ER ET KE SD SO SS UG | ER ET KE SO SD TA | ER ET KE SD SO SS UG TA | ER ET KE SD SO |
| | 2009/10 | BI ER RW SD SS TA UG | ER ET KE SD SO | BI ER RW SD SS UG | ER KE SD SO |
| | 2010/11 | ER ET KE SD SO SS UG | ER ET KE SD SO | ER ET KE SD SO SS UG | ER ET KE SD SO |
| | 2011/12 | SD SS UG | ER ET | BI RW SD SS UG | ER ET |
| | 2012/13 | ER SD SS UG | ER KE SD | ER SD SS | ER KE |
| | 2013/14 | KE RW SO TA UG | KE SO TA | RW UG TA | KE SD SO |
| | 2014/15 | ET RW SO SS UG | ER ET KE SD SO | ET SS UG | ER ET KE SD SO |
| | 2015/16 | ER ET RW SD SO | ER ET SD | ER ET SD | ER ET KE SD |
| Southern Africa | 2000/01 | AO MG | AO NA ZA | AO MG NA ZA | AO MG NA ZA |
| | 2001/02 | AO SZ ZM ZW | NA BW ZA ZW | AO BW SZ ZW | BW MZ NA ZA ZW |
| | 2002/03 | AO BW LS NA SZ ZA ZW | BW LS NA SZ ZA | BW LS NA SZ ZA | BW LS NA ZA ZW |
| | 2003/04 | AO ZA | AO BW MG NA ZA | AO MW SZ ZA | AO BW NA ZA |
| | 2004/05 | MW ZA ZM ZW | BW MW MZ NA ZW | MW MZ ZM ZW | BW MG MW MZ NA ZA ZM ZW |
| | 2005/06 | MG ZA | BW MG ZA | MG MZ SZ ZA | BW MG ZA |
| | 2006/07 | BW LS NA ZA | BW NA ZA | BW LS MW NA ZA | BW LS NA ZA ZW |
| | 2007/08 | MG | MW ZA ZW | MG ZW | MZ ZA ZW |
| | 2008/09 | ZA | BW NA ZA | ZA | BW MG NA ZA |
| | 2009/10 | AO MG MG LS MZ NA ZA | MG NA ZA | AO MG | AO MG NA ZA |
| | 2010/11 | MG MW MZ ZA | NA ZA | MG MZ ZA | ZA ZW |
| | 2011/12 | AO BW LS MW MZ ZA ZW | BW MZ ZW | AO BW LS MG MZ ZA ZW | AO BW LS MZ ZW |
| | 2012/13 | AO BW LS MG NA ZA ZM ZW | BW LS MG NA ZA ZW | AO BW MG NA ZM ZW | AO BW MG MW NA ZA ZW |
| | 2013/14 | LS MG MZ ZA ZM | LS MG ZA | LS MG ZM | AO LS MG NA ZA |
| | 2014/15 | AO BW LS MG MW MZ NA SZ ZA ZM ZW | BW LS MG MW NA ZA | AO BW LS MZ MW NA ZA ZM | AO BW LS MZ NA ZA |
| | 2015/16 | LS MG MW MZ NA SZ ZA ZM ZW | BW LS MG MZ NA SZ ZA | LS MW MZ NA SZ ZA ZM | BW LS MG MZ NA SZ ZA |

* Country codes: AO = Angola, BI = Burundi, BW = Botswana, ER = Eritrea, ET = Ethiopia, KE = Kenya, LS = Lesotho, MG = Madagascar, MZ = Mozambique, MW = Malawi, NA = Namibia, RW = Rwanda, SD = Sudan, SO = Somalia, SS = South Sudan, SZ = Swaziland, TA = Tanzania, UG = Uganda, ZA = South Africa, ZM = Zambia, ZW = Zimbabwe

spatially dynamic drought pattern can be revealed for the examined time period. Hereby, seasonal years of regionally widespread drought conditions, mostly located over core areas with particularly strong drought signals, are exhibited. Regarding analyses of the vegetation-related VCI, a generally larger and stronger drought signal is noticeable over Africa compared

to drought patterns of rainfall-related SPI-3. With reference to the selected focal regions of eastern and southern Africa, Table 5.1 lists countries that were affected by severe agricultural droughts in a corresponding seasonal year of the study period. This information is based on visual examination of the retrieved SPI-3- and VCI-based drought patterns. Particularly drought-affected years are framed.

With focus on eastern Africa, 2009 and 2011 stand out as years of extensive droughts based on the severity and relative duration of agricultural droughts (see Table 5.1 and figures 5.2 - 5.5). Additionally, VCI-based parameters reveal 2001, 2005 and 2006 as drought-affected seasonal years for Kenya and Somalia. Further, droughts were also detected for 2002-2003, 2008 and 2015-2016 over central Ethiopia (see also local SPI dynamics in appendix, Figure 2). In 2009, regions of major precipitation deficit were concentrated in northern Ethiopia and Eritrea as well as in southern Kenya and north-eastern Tanzania, consisting of large areas where mean SPI-3 ranges between $-1$ and $-1.5$. The vegetation-related drought index basically retraces this pattern. However, VCI-based indicators reveal strikingly stronger drought conditions over northern Ethiopia, in the Rift Valley, and across Kenya, where agricultural droughts affected a large part of the growing season. According to mean SPI-3, the seasonal year 2011 was influenced by increased drought conditions in south-eastern Sudan and west Eritrea. A "hot spot" area of severe drought (mean SPI-3 between $-1.5$ and $-2$) can be found over southern Ethiopia, as well as a moderate drought signal (mean SPI-3 between $-0.5$ and $-1$) spanning widely across Kenya and southern Somalia. Here, mean VCI drought signal is similar to SPI-3 and especially striking for Kenya and Somalia (VCI between 20 and 30 %). However, no drought indication is present over western Ethiopia and Uganda, where a precipitation deficit was persistent during the growing season. Relative VCI-based drought duration pattern retraces the SPI-related signal and particularly highlights northern Kenya and Somalia, where over 50 % of the growing season was influenced by drought.

Southern Africa is extensively affected by sever agricultural droughts during the seasonal years of 2003 and 2015/16 according to both drought severity and indicators of relative duration of droughts (see Table 5.1 and figures 5.2 - 5.5). Further drought years are 2005, 2007 and 2013, where a drought signal is revealed over parts of the focal region. For 2003, both precipitation-based drought indicators (mean SPI-3 and SPI-3-based relative duration of drought) expose drought conditions centred over north-eastern South Africa, Lesotho, eastern Botswana, west and north-eastern Zimbabwe as well as over south-eastern Namibia. The vegetative drought pattern mostly agrees with the SPI-based one, but reveals larger extents of drought-affected areas. Accordingly, nearly the complete agricultural area of Botswana and Namibia was influenced by drought, showing a mean VCI of below 20 % and relative drought durations of over 70 % of the growing season. For the seasonal year 2016, which was analysed only until April, SPI-based drought signals are centred over central South Africa/Lesotho and Namibia with mean SPI-3 as far as -1.5 and a relative drought duration of up to 100 %. Drought indications are also given in eastern South Africa and southernmost Mozambique, showing a large area of severe drought conditions with SPI-3 ranging between $-1.5$ and $-2$ and relative durations of 80-100 %. This pattern is mirrored by VCI-based indicators.

Strikingly, a core area with high drought signals situated over Mozambique, Malawi, eastern Zimbabwe and Zambia can be revealed from SPI-3. Values are below -1 with a circular pattern of SPI-3 between $-1.5$ and $-2$ and drought duration of 80-100 % of the growing season. However, no major vegetation-related drought signal is present for the mentioned region. This marks the area of strongest deviations between SPI-3- and VCI-based drought patterns.

## 5.3 Relation between ENSO and agricultural drought

### 5.3.1 Correlation between ENSO and drought index time series

The comparison of cross-correlation results between the ENSO index MEI and each of the two drought indices reveals a broadly consistent pattern. Although correlation coefficients do not exceed an absolute value of 0.6 and, thus, only weak to moderate linear relations can be suggested between ENSO and drought indices, the direction of correlation sheds light on the spatio-temporal pattern of emerging droughts in relation to ENSO events. Figure 5.6 displays the maximum correlation coefficient with its corresponding time lag for the cross-correlation between MEI and SPI-3 and VCI, respectively.
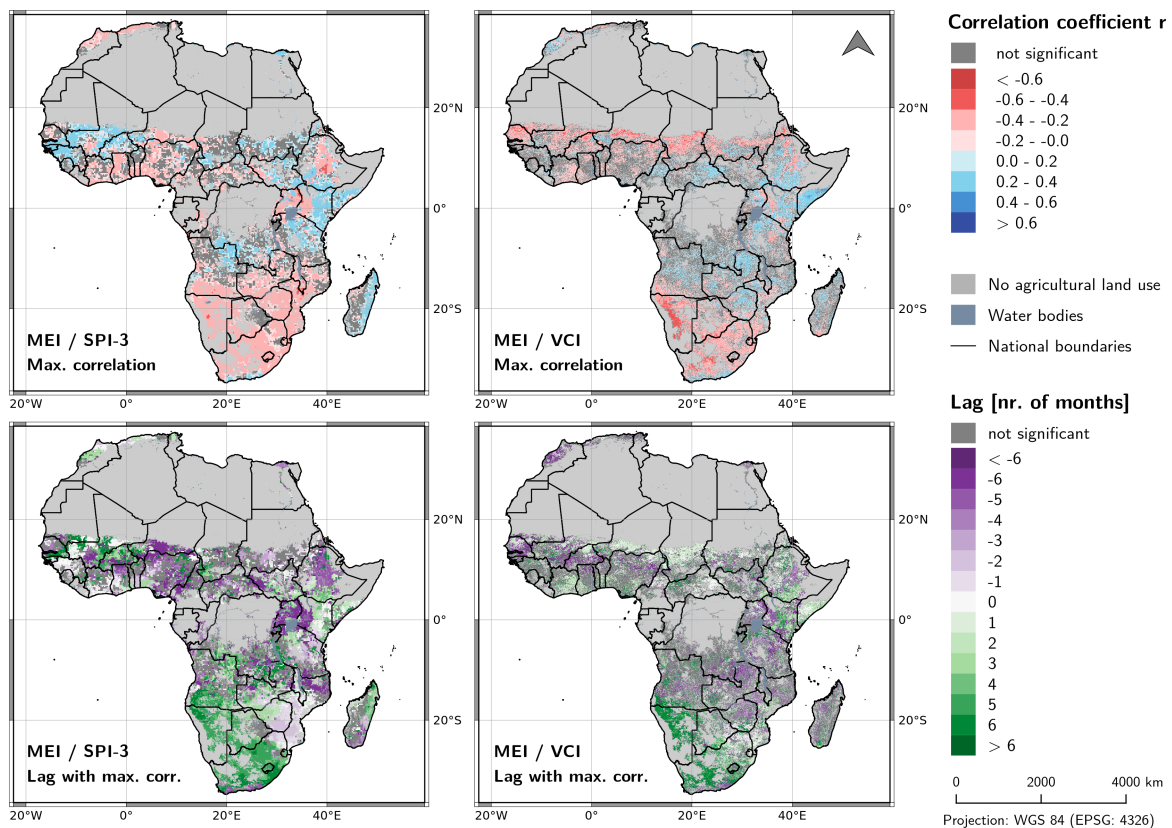


**Figure 5.6:** Maximum correlation coefficients over Africa between the ENSO index MEI and SPI-3 (top left)/ MEI and VCI (top right) and their corresponding time lags in months (bottom)

Over large areas in southern Africa, negative correlation coefficients ($-0.5 < r < -0.2$) were measured, which indicates weak to moderate negative relations between MEI and drought index time series. Consequently, the drought index tends to decrease when MEI increases,

which results in a tendency towards drought conditions over southern Africa during El Niño events. The SPI-3-based correlation pattern reveals a moderate negative correlation hot spot over Malawi, Mozambique, Zambia and Zimbabwe, whereas VCI exhibits a different, rather mixed signal for this area. The latter consists of a predominant positive correlation over Zambia, Zimbabwe and north-eastern Mozambique, whereas Malawi, central and southern Mozambique are dominated by weak negative correlation coefficients. Regarding the temporal offsets, the maximum correlation between MEI and SPI-3 over South Africa, Lesotho, Namibia and Botswana was detected for time lags of 4 to 6 months, whereas Malawi, Mozambique and Zimbabwe show the highest correlation coefficients for a time lag of -2 to 0 months. VCI-based time lags reveal a similar pattern. Although matching the arrangement of VCI-related correlation values, a diffuse pattern of time lags is present over the region of Malawi, Mozambique and Zimbabwe, where a belt of negative lags between -6 and -3 can be identified over Zimbabwe and lags of 0 to 3 months dominate Malawi and southern Mozambique. Strikingly, a meridional dipole is identified in the correlation patterns over southern Africa. This dipole between generally negative correlation coefficients in the south and positive values in the north is emergent at about 15°S for SPI-3 and 18°S for VCI. Thus, VCI reveals a positive relation to MEI over the northern parts of southern Africa, whereas SPI-3 indicates a contrary behaviour.

Eastern Africa shows a positive correlation pattern indicating weak to moderate relations to ENSO ($0.2 < r < 0.5$) over southern Ethiopia, eastern Kenya and Somalia based on both SPI-3 and VCI time series. The corresponding time lag lies between 0 and 4 months. Thus, for this region, El Niño events are associated with abnormally wetter conditions, whereas La Niña can be related with drier conditions. In contrast, a negative correlation pattern is present for both drought indices over central and northern Ethiopia (time lags between -5 and -4 months), a small strip along the coast of Somalia (time lags of about -6 months) and, secondly, north of the Victoria Lake covering Rwanda, Uganda and western Kenya (time lags of -6 to -5 months). In these areas, the SPI-3 pattern is spatially more extensive, whereas for VCI, bands of negative correlation are limited to the border region between Uganda and Kenya and the Rift Valley of Ethiopia. However, VCI-based correlation values additionally display a negative relation to ENSO over Sudan and Eritrea. Here, time lags are between -4 and -2 for Ethiopia, -6 and -5 for Uganda/Kenya as well as 0 and 4 months for Sudan/Eritrea. Hence, a drought signal is revealed for central Ethiopia and the border region of Uganda and Kenya, taking place prior to the MEI maximum, in the context of El Niño. Vegetative droughts tend to occur after the MEI peak over Sudan and Eritrea. All in all, a rought east-west dipole can be identified from the correlation patterns over eastern Africa.

## 5.3.2 Droughts during individual ENSO events

### 5.3.2.1 ENSO-related drought dynamics on a monthly scale

For the strongest El Niño and La Niña events that where registered between 2000 and 2016, the development of agricultural droughts is monitored in Figures 5.7, 5.8, 5.9 and 5.10. Hereby,
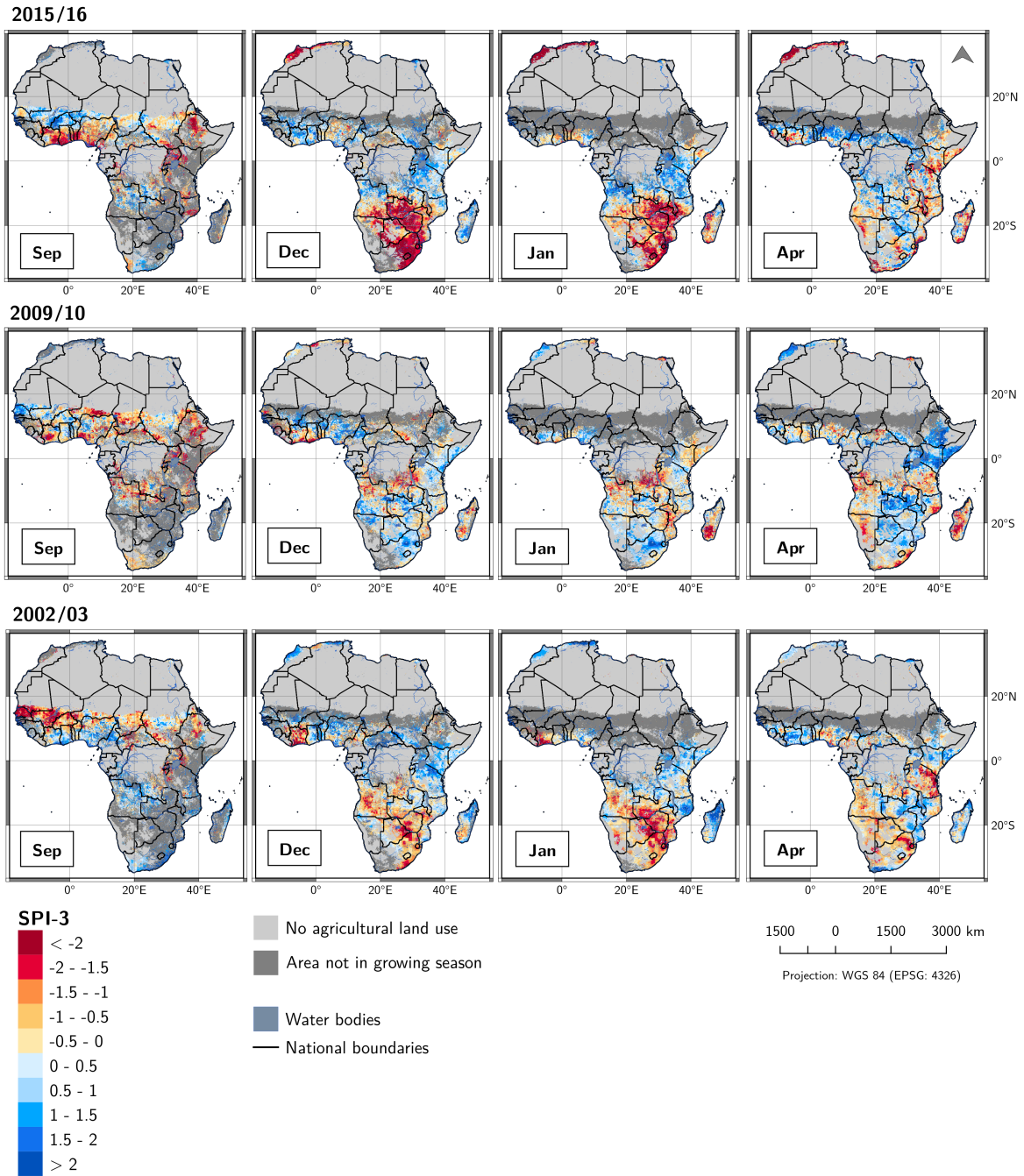
**Figure 5.7:** SPI-3 for El Niño events 2015/2016 (strong), 2009/10 (moderate) and 2002/03 (moderate) during September (Sep), December (Dec), January (Jan) and April (Apr)

drought indices are compared on a monthly scale. Firstly, September is selected as a month representing conditions during the onset of the respective ENSO event. What is more, December (Dec) and January (Jan) reflect the time where ENSO is at its highest intensity and, lastly, April (Apr) is monitored as a month during the declining ENSO event. Months were chosen according to their coincidence with major growing seasons over eastern and southern Africa. In this case, site-specific growing seasons are included, whereas all areas where the average growing season does not coincide with the selected months are excluded from the analyses (dark grey colours in maps). Figure 5.7 shows the development of SPI-3 and Figure 5.8 the monthly means of VCI during El Niño events of 2015/16, 2009/10 and 2002/03.

48
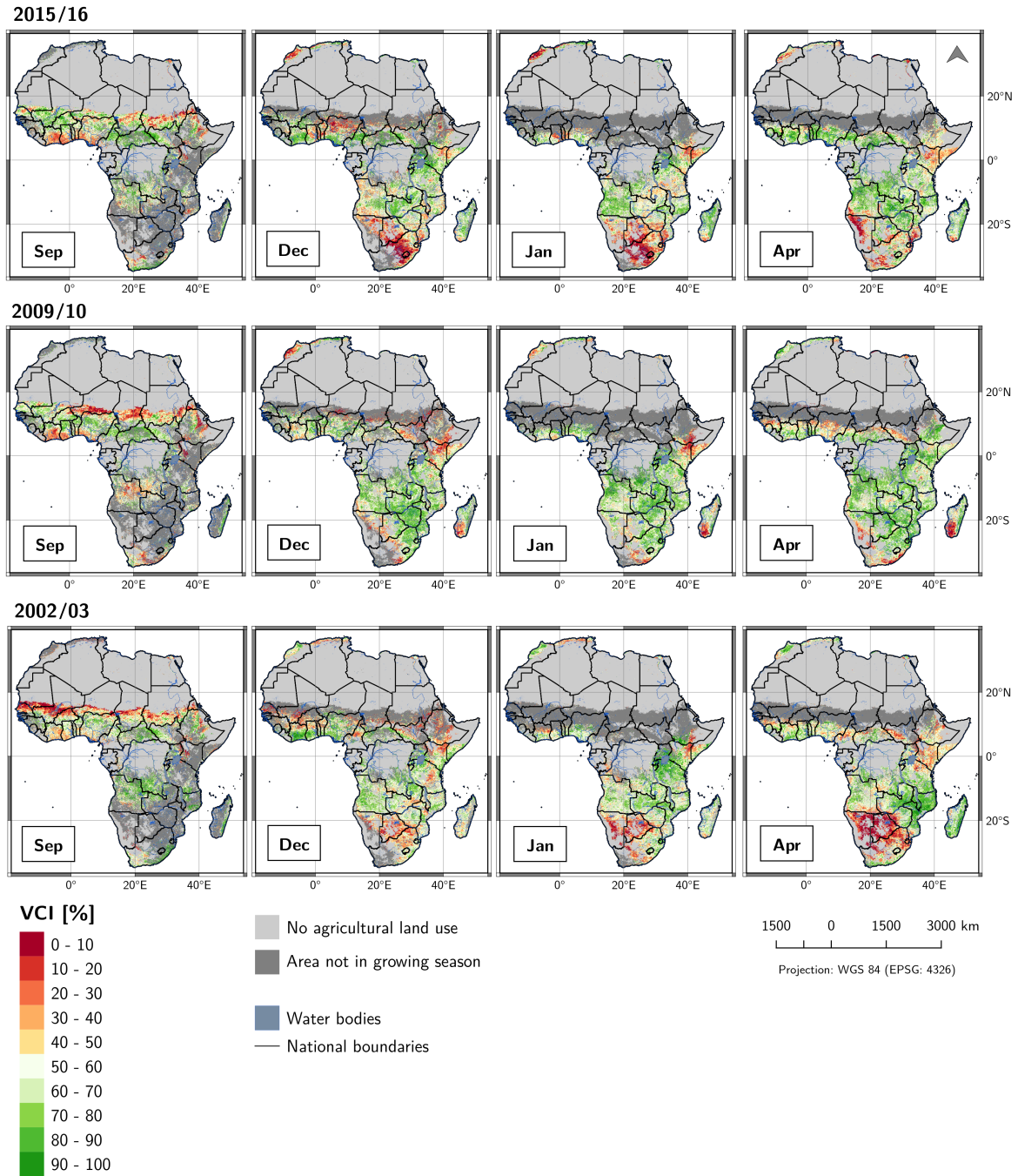
**2015/16**



**Figure 5.8:** Monthly means of VCI for El Niño events 2015/2016 (strong), 2009/10 (moderate) and 2002/03 (moderate) during September (Sep), December (Dec), January (Jan) and April (Apr)

In the ongoing El Niño 2015/16, which was categorized as strong event based on ONI, drought can be monitored over Ethiopia, Eritrea, Kenya and Uganda showing extensive, severely to extremely dry conditions based on SPI-3 (map for September 2015). Further, Sudan is affected moderately. VCI shows a similar pattern, where droughts are concentrated over Ethiopia, Eritrea, Kenya and Sudan. Though, Uganda is not affected by vegetative droughts. Further, some areas in West Africa, including the Ivory Coast, Ghana, Togo and Benin are affected by dry conditions in September based on both drought indices. The largest extent of SPI-3-based droughts are recorded in December over southern Africa. Especially, Zambia, Zimbabwe, South Africa, Swaziland and Lesotho were affected by extreme droughts, which are
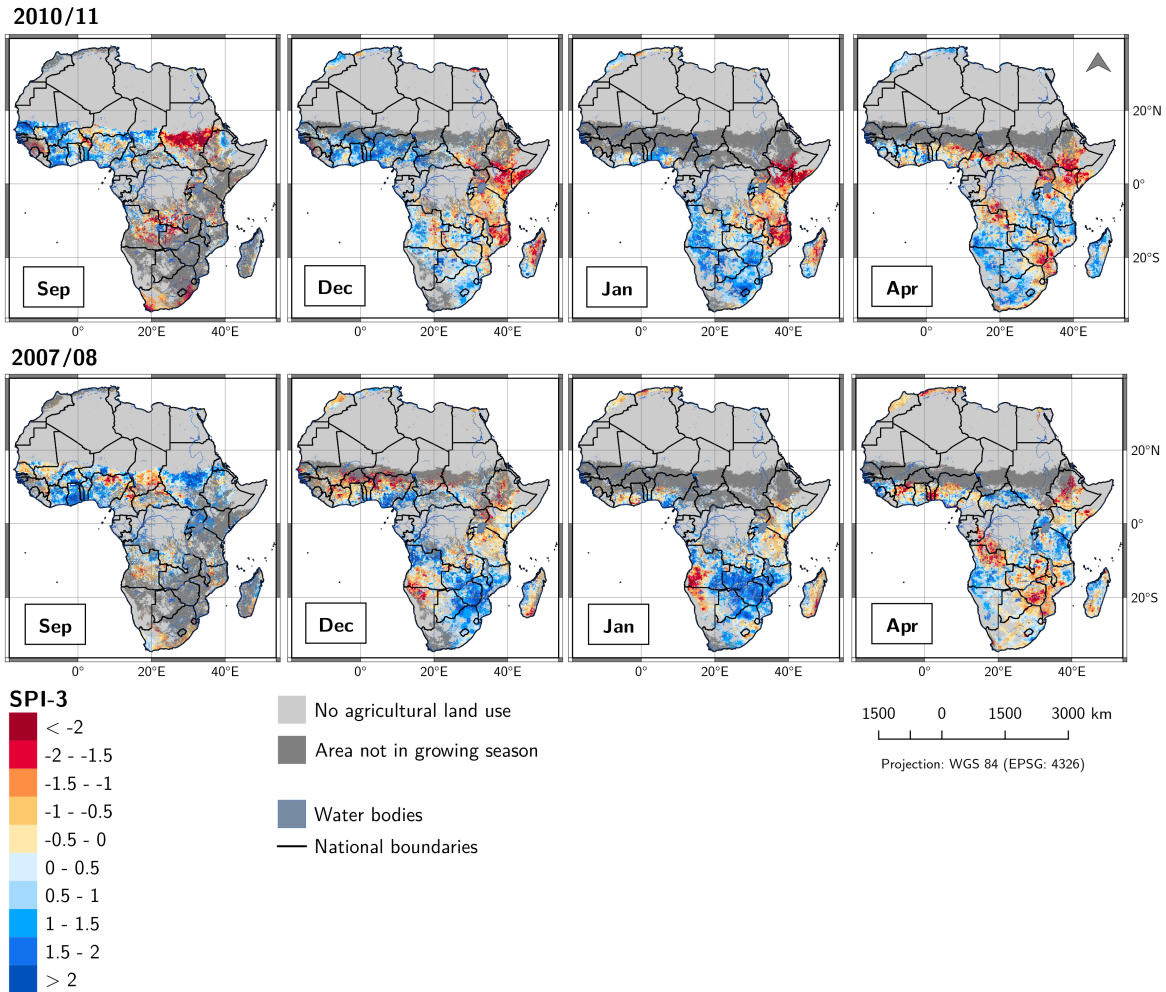
**Figure 5.9:** SPI-3 for La Niña events 2010/11 (moderate) and 2007/08 (moderate) during September (Sep), December (Dec), January (Jan) and April (Apr)

indicated by SPI-3 below -2. In the following month, the core zone of drought decreases and moves in northeastern direction towards Malawi and Mozambique. Monthly means of VCI also indicate extreme drought conditions during these months of high El Niño intensity, with large areas showing VCI values below 20. However, VCI exhibits a strikingly smaller drought extent over southern Africa than SPI-3. Here, the zone of drought over Malawi and Mozambique, revealed from SPI-3, is lacking and drought signals are in fact concentrated over Botswana, South Africa and Lesotho. During the decline of El Niño (map for April 2016), droughts are still persistent in southernmost South Africa, Namibia and southern Mozambique for both drought indices. Additionally, agricultural droughts are monitored over Kenya and Somalia for January (spot) and April 2016 (extensive area).

In comparison to 2015/16, the observation of drought indices for the moderate El Niño 2009/10 reveals a different pattern. However, a severe to extreme drought pattern is observed over eastern Africa during the onset of El Niño, resembling the situation of 2015. Differences arise from the months with the highest El Niño intensities. For southern Africa, SPI-3 exhibits a weak signal of moderate droughts over Mozambique, more pronounced during January 2010, and scattered extreme droughts in southern Madagascar. VCI indicates scattered droughts

**2010/11**



**2007/08**



**VCI [%]**

- 0 - 10
- 10 - 20
- 20 - 30
- 30 - 40
- 40 - 50
- 50 - 60
- 60 - 70
- 70 - 80
- 80 - 90
- 90 - 100

No agricultural land use

Area not in growing season

Water bodies

National boundaries

1500  0  1500  3000 km

Projection: WGS 84 (EPSG: 4326)
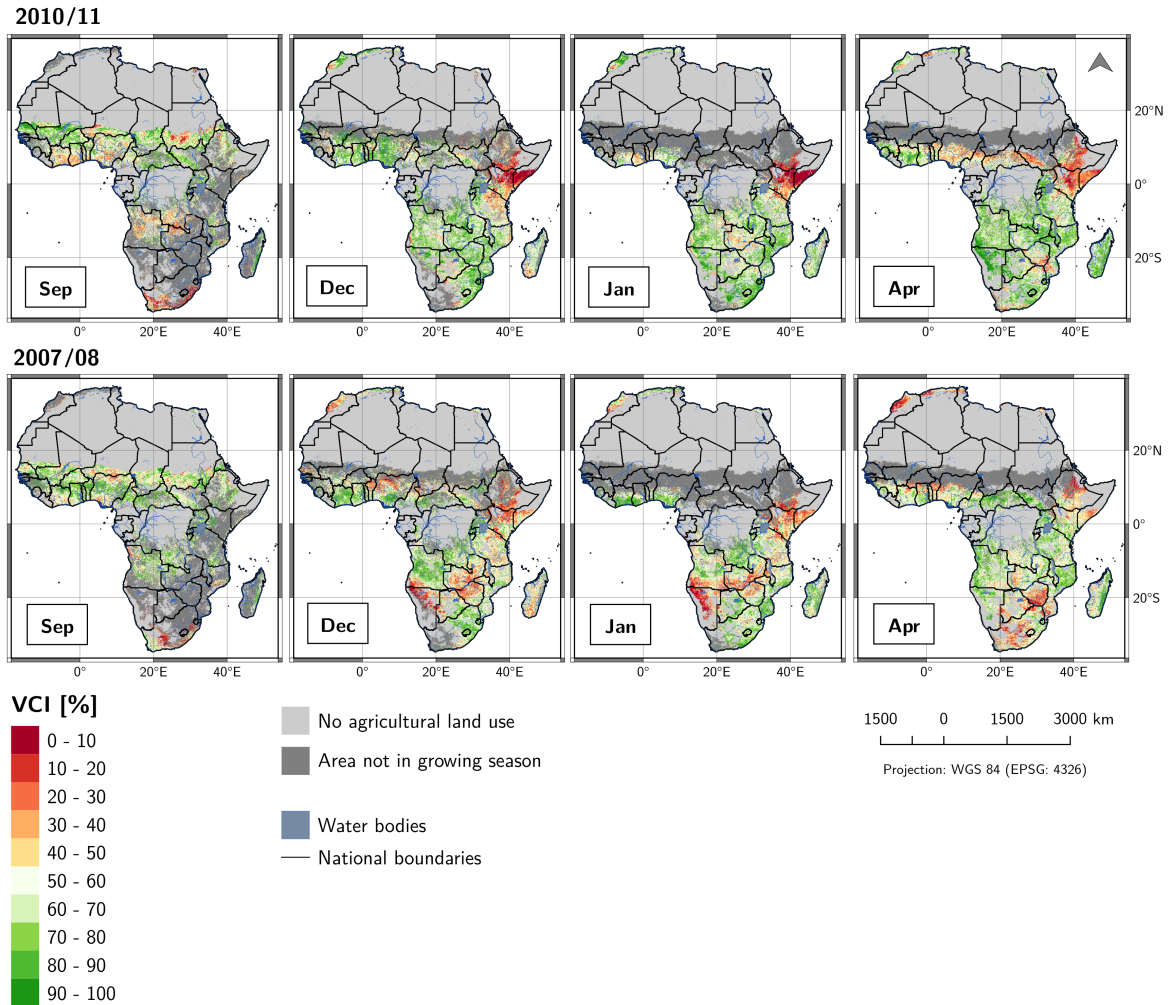
**Figure 5.10:** VCI for La Niña events 2010/11 (moderate) and 2007/08 (moderate) during September (Sep), December (Dec), January (Jan) and April (Apr)

over south-western South Africa, parts of Namibia, western Botswana and southern Madagascar. All in all, no comparable drought signal to 2015/16 is found for El Niño 2009/10. In April 2016, spots of moderately to extremely dry conditions along the southern coast of South Africa are revealed from both drought indices.

El Niño 2002/03 exhibits a drought pattern roughly similar to the 2015/16 situation. First of all, eastern Africa was affected by droughts during the onset of El Niño (September 2002). This observed pattern is similar to both the 2015/16 and 2009/10 events. Regarding the high-intensity phase of El Niño, a major drought signal can be identified over southern Africa during December and January based on both drought indices. For SPI-3, the drought-affected countries are eastern Botswana and South Africa, Zimbabwe, Lesotho and Swaziland, where dry conditions were particularly emergent during January 2003. VCI-based drought signal over southern Africa is focussed on Namibia, Botswana and South Africa, whereas Zimbabwe does not exhibit a noteworthy drought pattern. Further, a vegetation-based drought signal was still present in the declining event (April 2003). Thus, compared to SPI-3-based images, the core region of droughts is shifted more to the west and the drought signal shows a higher persistence.

Figures 5.9 and 5.10 show SPI-3 and VCI for the moderate La Niña events 2010/11 and 2007/08, respectively. During the onset of La Niña 2010/11 (September 2010), a precipitation deficit was observed over central Sudan and southern South Africa. The vegetation-based pattern retraces the drought signal in South Africa, however, indicates merely small spots of drought in Sudan. SPI-3 and VCI reveal a pronounced extensive agricultural drought in eastern Africa in December and January, when La Niña reached its highest intensity. Most affected areas are situated in Ethiopia, Kenya and Somalia with extreme SPI values of below -2 and VCI of below 10. SPI-3 exhibits other core areas of severe drought over northern Mozambique and Madagascar, which are not matched by VCI. The eastern African drought demonstrates a high persistence, since even in the declining stage of La Niña (April 2011), a severe drought signal can be observed from both indicators.

During La Niña 2007/08, a generally weaker drought pattern is monitored compared to 2010/11. For the onset of the La Niña event (September 2007), moderate drought conditions are observed along the South African coast, matching the pattern of La Niña 2010/11. With respect to December and January, drought indices reveal a slightly differing picture. Although SPI-3 only shows drought conditions over Ethiopia and does not indicate a major extensive precipitation deficit over Kenya and Somalia, VCI exhibits a moderate drought signal over the mentioned eastern African region for December and January. Both indices show droughts in Namibia, whereas the SPI-based drought pattern displays a precipitation deficit spanning to Angola (January 2008). In the subsequent declining stage of La Niña (April 2008), SPI-3 and VCI widely coincide, revealing a drought pattern focussed on Ethiopia and Somalia as well as Botswana.

#### 5.3.2.2  Response times of ENSO-related droughts

For each of the previously pictured El Niño and La Niña events, time lag analysis was carried out, individually. Hereby, the temporal offset between the month of highest ENSO intensity and the month with lowest drought index value are examined. As an example for El Niño, Figure 5.11 presents the time lag pattern of observed droughts during 2002/03. With focus on La Niña, Figure 5.12 displays the time lag of droughts during 2010/11. Negligible areas were masked. Accordingly, if the detected minimum drought index is not indicating at least moderately dry conditions (see thresholds in Table 4.2), if no significant correlation was revealed (see significance mask from correlation analysis in Section 5.3.1), or if the respective growing season was not affected by droughts (threshold of 0 %, see relative duration of drought, Figures 5.4 and 5.5), pixels are displayed in dark gray.

During El Niño 2002/03, drought-affected areas with significant correlation results are limited to large areas in southern Africa and to smaller regions of eastern Africa. Further, a zonal band of droughts with negative time lags across West Africa spanning to the Sahel zone is observed. The spatial pattern of temporal offsets is divided into two segments over southern Africa, where the west differs from the east (see Figure 5.11, left). Hence, large areas in South Africa, Namibia and western Botswana are affected by most intense droughts 4 to 6
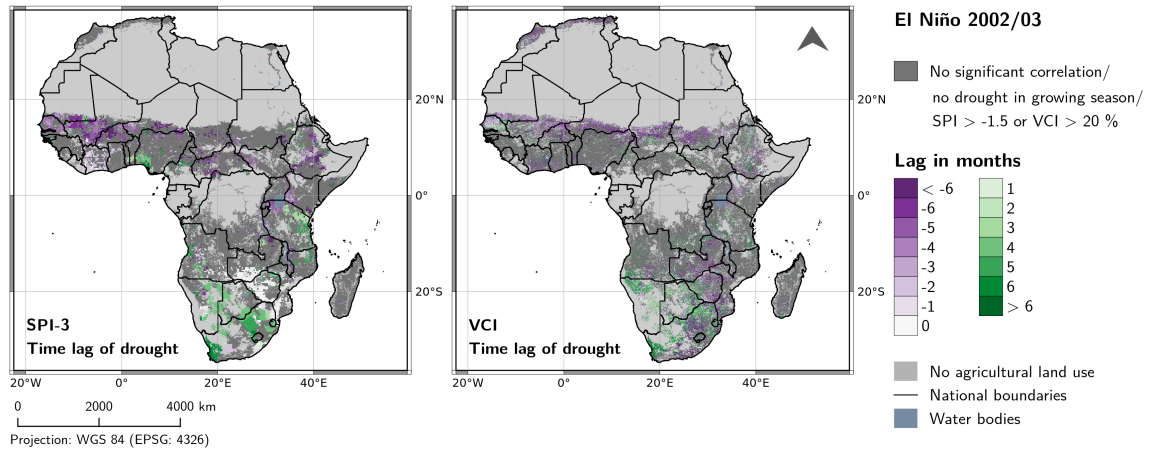
**Figure 5.11:** Temporal offset between MEI peak and drought index minimum during El Niño 2002/03 for SPI-3 (left) and VCI (right)
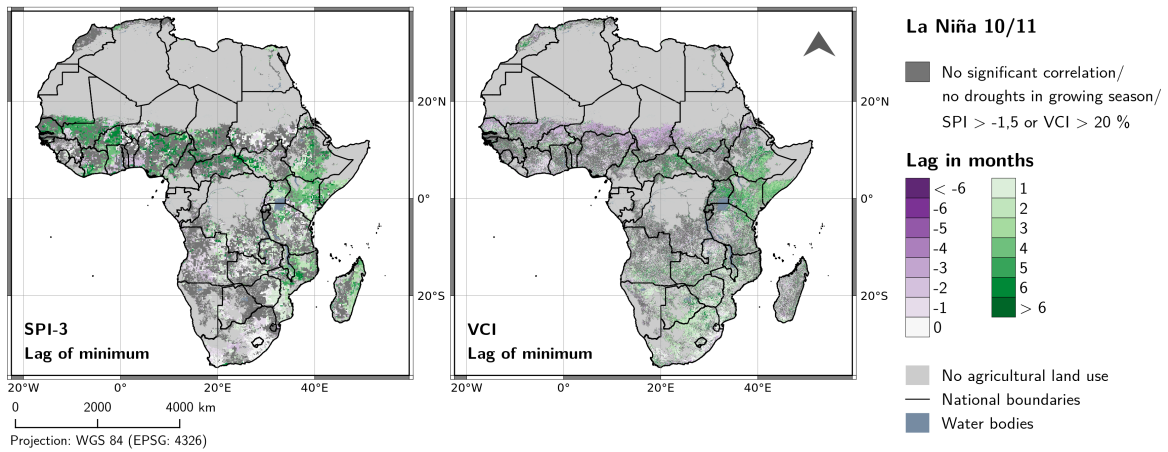


**Figure 5.12:** Temporal offset between MEI minimum and drought index minimum during La Niña 2010/11 for SPI-3 (left) and VCI (right)

months after the MEI peak, whereas strongest droughts in eastern Botswana, Zimbabwe and southern Mozambique were observed directly in the month of the highest El Niño intensity. VCI-based thresholds reveal a larger drought-affected area for time lag analysis. Temporal offset of severe and extreme droughts in southern Africa are mostly between 3 to 6 months, whereas some regions in central South Africa and especially in Botswana and Mozambique exhibit negative time lags of -7 to -3 months, which differs from the SPI-3-based pattern (see Figure 5.11, right). The resulting time lag pattern for El Niño 2002/03 over southern Africa is broadly consonant with the respective temporal offsets unfolded by correlation the time series of ENSO and drought indices (see section 5.3.1, Figure 5.6). What is more, eastern Africa contains several drought-affected areas. Central Ethiopia reveals strong droughts occurring before the El Niño peak (time lags between -3 and 0 and partly below). The negative lags in this region are consistent with both SPI-3- and VCI-related time lag images revealed from correlation analyses (see Section 5.3.1, Figure 5.6). Northwestern Ethiopia, Eritrea and Sudan are partially affected by vegetative drought in temporal coincidence with the MEI peak. This is also observed from the VCI-based lag pattern of the correlation analyses (see Section 5.3.1, Figure 5.6, right).

The time lag pattern for La Niña 2010/11 exhibits positive values for the major significantly drought-affected areas in eastern Africa, especially southern Ethiopia, Kenya, Uganda and Somalia (see Figure 5.12). Here, severe to extreme agricultural droughts arose 3 to 5 months after the month of MEI minimum that indicates the highest intensity of La Niña. In comparison, correlation-based time lag images also revealed positive offsets ranging from 0 to 4 for the mentioned region (see Section 5.3.1, Figure 5.6).

By comparing the observed occurrence of droughts during major El Niño and La Niña events, it can be concluded that no universal drought pattern exists during different ENSO events. Independently from its intensity, each warm or cold phase shows a different precipitation- and vegetation-based drought signal. These variations apply to both space and time. However, similar drought patterns were revealed for certain regions. These are consistent with the tendencies unfolded by means of the correlation analysis (see Figure 5.6), regarding the occurrence of droughts during the respective ENSO phase and its time lags. As an example, for each of the three studied El Niño years, drought could be identified in Ethiopia and western Kenya during the onset of the event and prior to the actual El Niño peak (see Figures 5.7, 5.8 and 5.11). This pattern is coherent to the respective correlation result (see Section 5.3.1, Figure 5.6), showing negative correlation coefficients with monthly lags of about -6 to -4. Further, the widely negative correlation of both drought indices to MEI over southern Africa with different positive time lags can be confirmed by drought signals for two of the three El Niño events (2015/16 and 2002/03). Likewise, this applies to La Niña, where revealed positive correlations between ENSO and drought indices for Ethiopia, Kenya and Somalia could be verified for the 2010/11 and to a weaker extent for the 2007/08 La Niña situation. These La Niña-related drought dynamics are also present in the correlation result.

## 5.4  Regional impacts of agricultural drought

The effects of particularly severe drought years on administrative areas, cropland and national agricultural production is analysed with focus on eastern and southern Africa. Hereby, the regional drought severity is expressed by means of the relative duration and the spatial extent of agricultural droughts on cropland areas.

### 5.4.1  Drought in southern Africa in 2002/03

Maps of Figure 5.13 show the relative duration of droughts during the growing season for sub-national administrative units (GADM level 1) over the focus region of southern Africa. The result is displayed both for SPI-3- (top page) and VCI-based (bottom page) thresholds of severe drought. Based on SPI-3, administrative units with highest average persistence of drought comprise all 4 regions of Swaziland (Lubombo, Shiselweni, Hhohho, Manzini), where over 50 % of the growing season was affected. Further, north-eastern provinces of South Africa (Limpopo, Mpumalanga, Gauteng), Quthing in Lesotho, Hardap in Namibia and North-East District in Botswana exhibit relative drought durations of over 40 % of the growing season. Regions with values of over 30 % are situated along a northwest-southeast directed band from

north-eastern Namibia to southernmost Zimbabwe and in the border regions between South Africa and Namibia. As indicated by VCI, the drought persistence during the growing season is especially high in nearly all Namibian regions, particularly in Hardap (over 90 %), Khomas and Omaheke (ca. 75 % each), districts of western Botswana (between 70 and 85 %) as well as in the northern provinces of South Africa, containing Northern Cape with about 70 %, North West Province and Limpopo with over 50 % each. In comparison to precipitation-based drought duration pattern, the vegetation-related signal exhibits more regions with intensively drought-affected growing seasons. Per trend, these are concentrated further in the west.

Additionally, the extent of drought-affected cropland is compared for SPI-3- and VCI-based thresholds of relative drought duration at a national scale (see thresholds in Section 4.4.2.2). The comparison is displayed in Figure 5.13 for selected countries. According to the SPI-based threshold, countries that show the highest spatial extent of drought-affected cropland in the season 2002/03 are Swaziland with 100 %, Botswana with 50 %, South Africa with 44 %, Namibia with 35 % and Zimbabwe with 32 %. VCI indicates the same most affected countries. However, it reveals a different order, comprising Botswana with 98 %, Namibia with 97 %, South Africa with 75 %, Swaziland with 72 % and Zimbabwe with 34 % of drought-affected cropland during the growing season. Here, values are strikingly higher for the core region over Botswana, Namibia and South Africa, compared to the SPI-based result.

Time series of crop production in tonnes (FAO, 2016b) is displayed on the right panel of Figure 5.13 for each of the selected drought-affected countries. Detailed values per crop type can be retrieved from Table 2 in the appendix.

Namibia does not show a decline in overall production for 2002/03, since roots and tubers, which represent the highest share of Namibian primary crops, exhibit a steady growth in production. However, cereal production slightly decreased (by about 7 %) from 2001 to 2002 to one of the lowest quantities within the recorded time span. Further, the production of pulses declined by about 39 %. For Botswana, an increase in cereal production of 50 % is visible in 2002. Thus, no clear drought impact on yields is derived from the statistics of crop production. In 2003, however, crop production was lower compared to adjacent years, with produced roots and tubers decreasing to the second lowest value from 2000 to 2013. In South Africa, the production of fruit and vegetables remained stable, whereas pulses decreased by around 38 % from 2001 to 2002. However, 22 % more cereals were produced, compared to 2001, leading to a generally high crop production. In 2003, the lowest production of roots and tubers was recorded. Further, cereal production dropped by about 9 %, which leads to a lower crop production in 2003, compared with the previous year. In Swaziland, the effect of droughts can be noticed in crop production numbers for 2002/03, although 2006/07 can be identified as the years of lowest production. In 2002, cereal production decreased by 18 % compared to 2001. The production of treenuts shows a decrease of 59 %. The amount of pulses, which declined by 19 %, came to its lowest recorded value. In 2003, the production of roots and tubers comes to a minimum. With focus on 2002/03, a striking decrease in crop production is depicted for Zimbabwe. In 2002, the quantity of produced cereals, which are the main primary crops, decreased by 51 % compared to the previous year.

**Relative duration of drought**
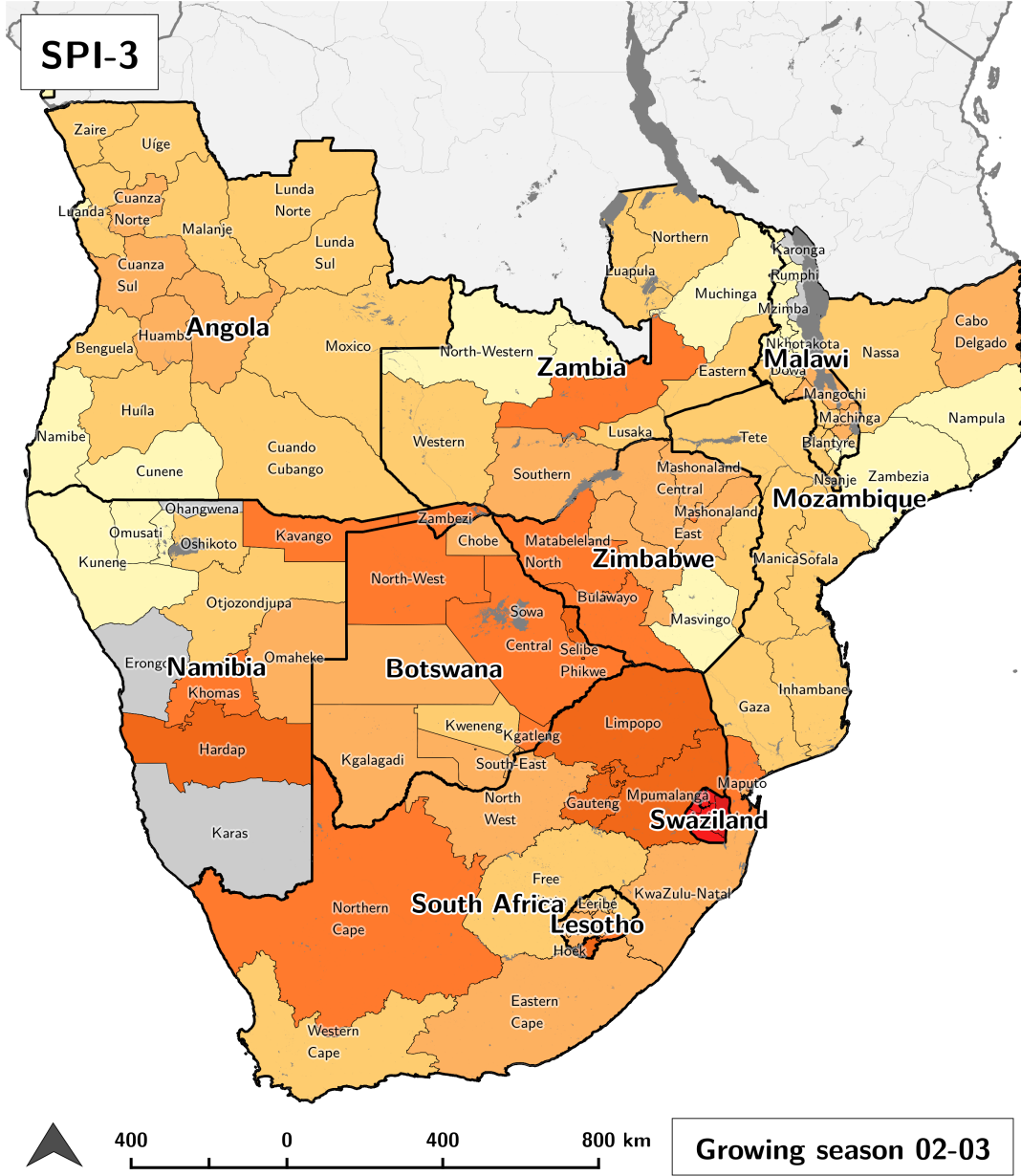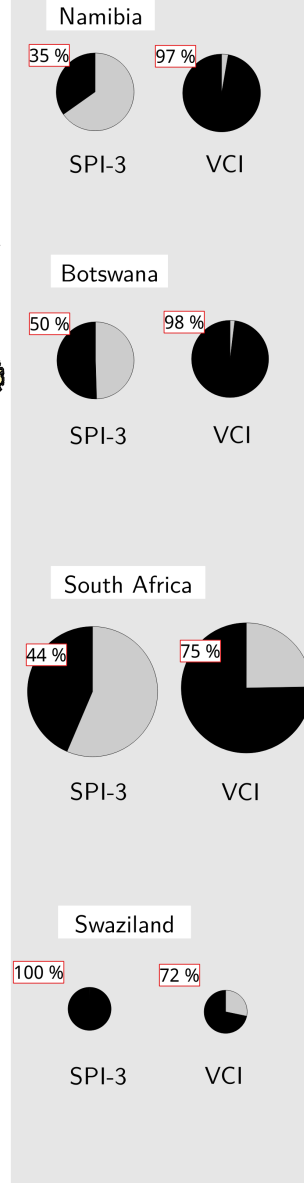
SPI-3

**Extent of drought-affected cropland**

**Statistics of crop production**

Growing season 02-03

Namibia

| 35 % | 97 % |
| SPI-3 | VCI |

Botswana

| 50 % | 98 % |
| SPI-3 | VCI |

South Africa

| 44 % | 75 % |
| SPI-3 | VCI |

Swaziland

| 100 % | 72 % |
| SPI-3 | VCI |

Namibia

Botswana

South Africa

Swaziland
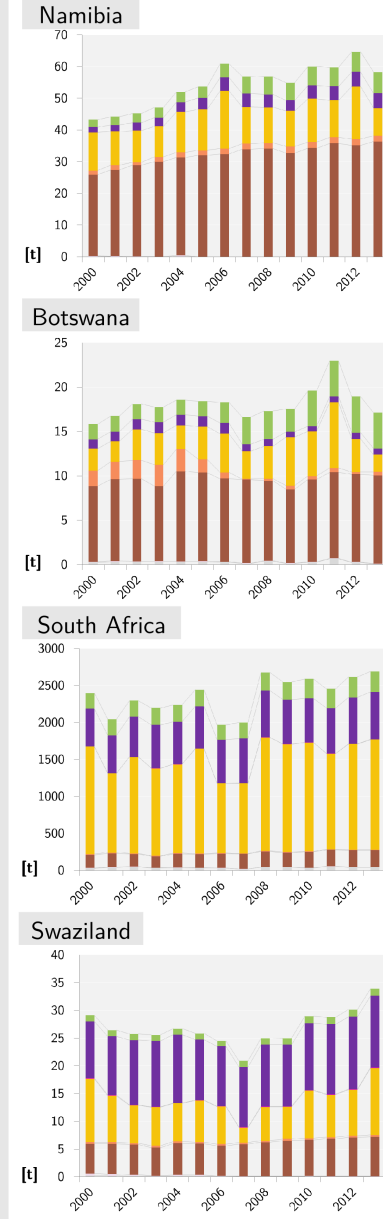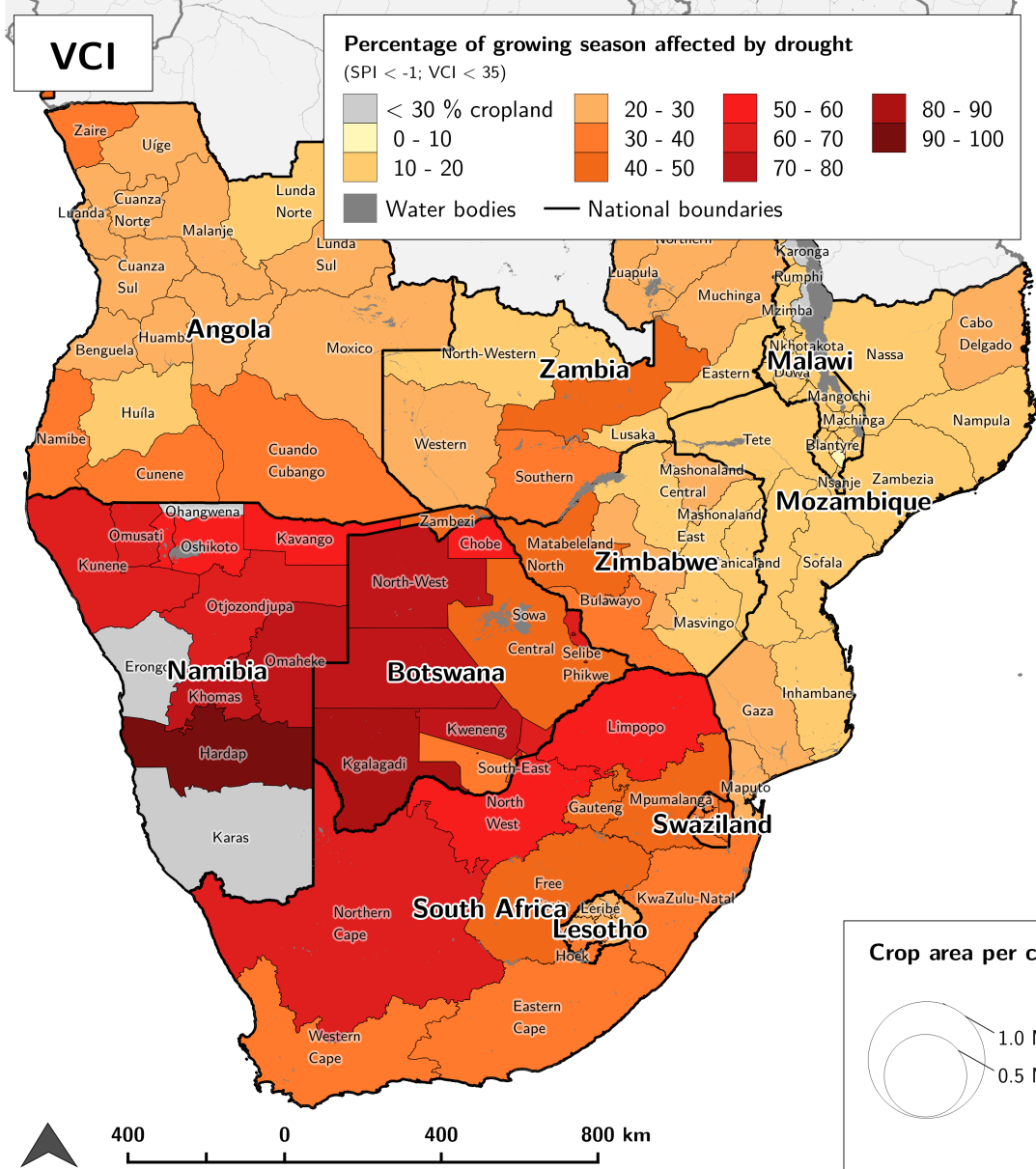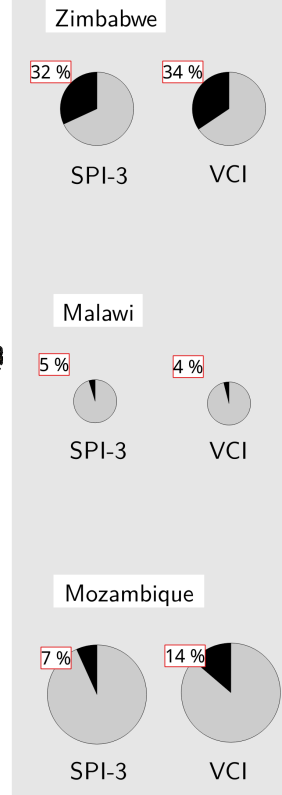
**Figure 5.13:** Agricultural droughts in southern Africa at regional level during the seasonal year 2003 based on SPI-3 and VCI: Zonal means of relative drought duration (see maps on left panel: top page for SPI-3, bottom page for VCI), drought-affected cropland area per country (pie charts on middle panel) and national statistics of crop production between 2000 and 2016 (bar charts on right panel, FAO, 2016b)

Although a further increase was measured for 2003, production still remained low. Crop production in Malawi was generally low from 2000 to 2005. In 2002, the production of roots and tubers, the main crops in Malawi, decreased about 53 % to its minimum value within the studied record and remained on a low level in 2003. Compared to 2001, when cereal production dropped about 29 %, even less cereals (-8 %) were produced in 2002. In Mozambique, 2002/03 coincides with a phase of low crop production. Cereal (-10 %) and treenuts (-13 %) production decreased from 2001 to 2002, revealing one of the lowest values within the recorded time period.

### 5.4.2   Drought in eastern Africa in 2010/11

Analogous to Figure 5.13, maps of Figure 5.14 show relative drought duration per region based on SPI-3 (top page) and VCI (bottom page) thresholds with focus on eastern Africa. According to SPI-3, regions with most persistent agricultural droughts in the seasonal year of 2011 were north-western Kenyan counties Marsabit, Wajir and Isiolo with relative drought durations of over 60 % of the growing season. Other regions with values of over 50 % are adjacent administrative units (Garissa in Kenya, Gedo in Somalia) and districts of Uganda (Nakasongola, Kampala and Nebbi). This SPI-3-based pattern of drought duration reveals a clear core zone over north-eastern Kenya, extending to Somalia, southern Ethiopia and eastern parts of Uganda, South Sudan and Sudan. VCI-based drought persistences reveal a similar pattern over eastern Africa. Here, nearly the same "hot spot" zone is identified over Kenya, though, spanning further to the northeast. Most affected counties were again Isiolo and Marsabit, showing relative drought durations of over 60 % of the growing season, as well as Turkana and Samburu with over 50 %. Other areas of strikingly high drought persistence can be identified in Somalia (Shabeellaha and Banaadir) and in the border region between Sudan and Eritrea (Al Qadarif, Sudan and Gash Barka, Eritrea), where values of over 50 % are exhibited. In contrast to the SPI-3-based pattern, VCI-derived core zones of high drought persistence does not extend into South Sudan and Uganda. However, the Ethiopian Rift Valley (Afar) and south-western Sudan is affected by prolonged drought periods in the growing season.

Regarding the extent of cropland affected by severe droughts in 2010/11, SPI-3 indicates Somalia with 75 %, Kenya with 65 % and Ethiopia with 43 % as most affected countries. According to the VCI-based threshold, even 95 % of the Somalian cropland was affected by persistent agricultural droughts during the growing seasons, whereas 67 % of agricultural areas in Kenya were struck. Sudan follows with 56 % and Eritrea with 52 %. Apart from South Sudan, VCI-related values of drought-affected cropland were higher than SPI-based ones, especially in the case of Somalia. Generally, both indices reveal a similar pattern.

Statistical data of crop production reveal low values for Sudan in 2010, showing a 36 % decline in cereal production. This cannot be compared with the depicted percentages of drought-affected cropland and drought duration, since, in the case of Sudan, the growing season of 2010 is not included in the seasonal year of 2011. In the latter, rather stable crop

production values were registered. Eritrea does not show any decline in crop production in 2011 either. However, remarkably low crop production amounts were registered from 2002 to 2004 and in 2008. Since Ethiopian crop production has generally been growing from 2000 to 2013, no clear drought impact can be retrieved for the season 2010/11. In contrast, statistical data for Somalia indicate a clear break in cereal production during 2011, showing a decrease of 67 % compared to 2010. Produced cereals came to its lowest value between 2000 and 2013. Since cereals normally account for a major part of the Somalian crop production, the overall amount of produced crops in 2011 represent the minimum of the studied time series. A decline in crop production in 2011 can be monitored for Kenya, too. Most notably, vegetable and fruit production decreased about 22 % and 20 % with respect to the previous year. Further a slight drop (-7 %) in produced cereals is visible.

Relative duration of drought

SPI-3

Growing season 10-11

Extent of drought-affected cropland

Statistics of crop production

Sudan

36 %  SPI-3    56 %  VCI

South Sudan

39 %  SPI-3    8 %  VCI

Eritrea

39 %  SPI-3    52 %  VCI

Ethiopia

43 %  SPI-3    48 %  VCI
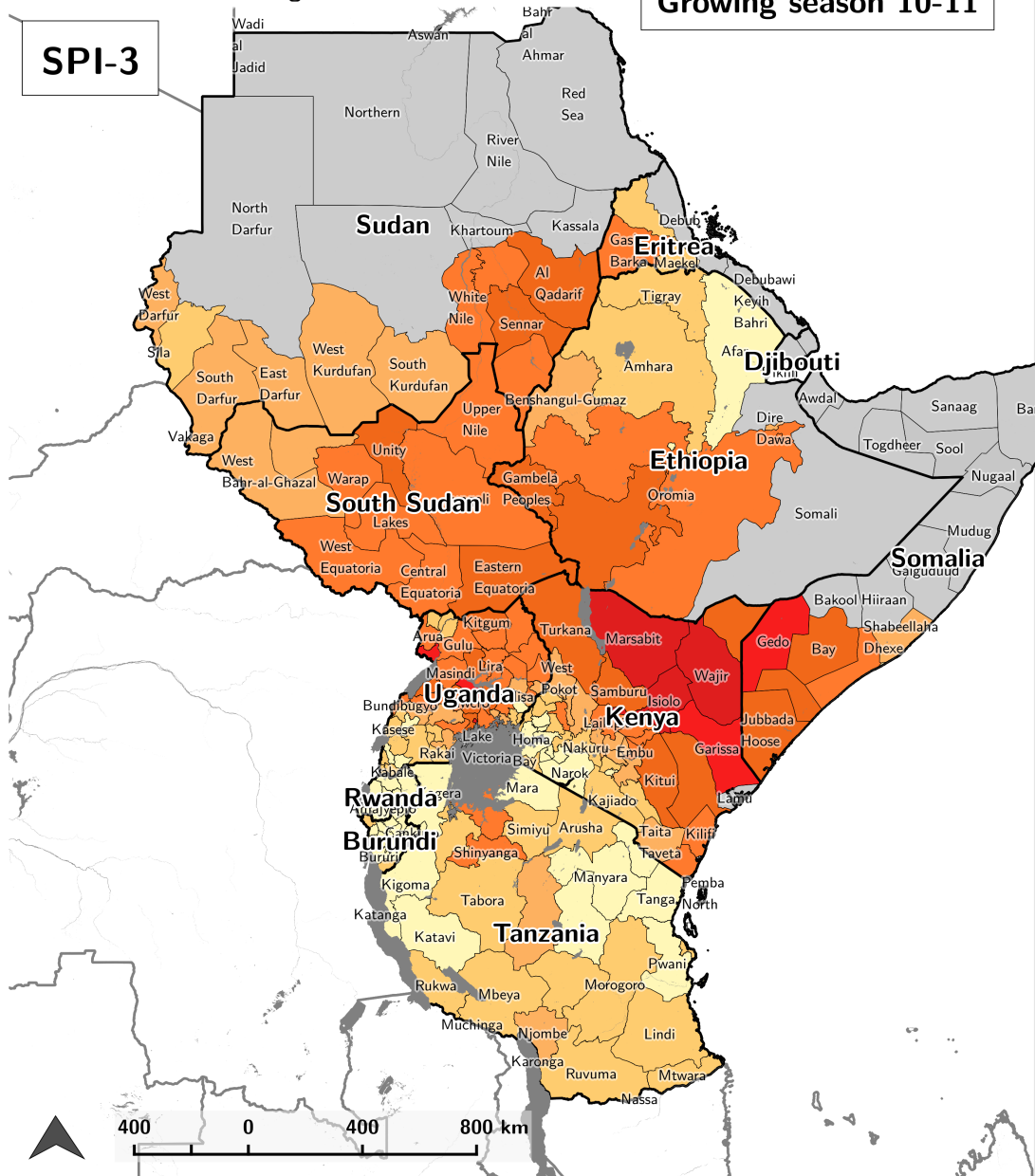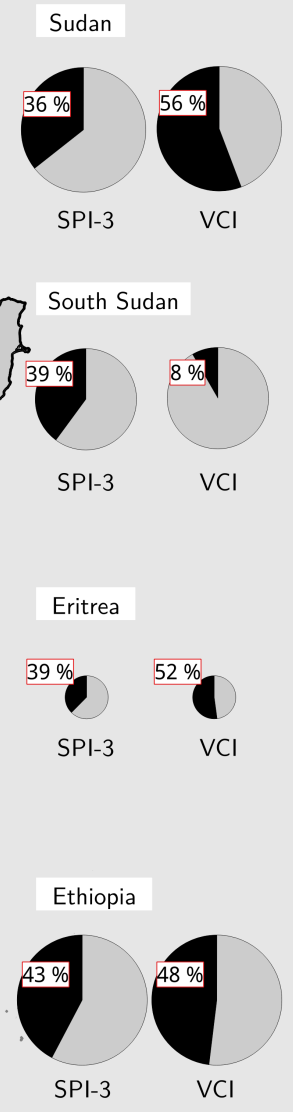
(Former) Sudan and South Sudan
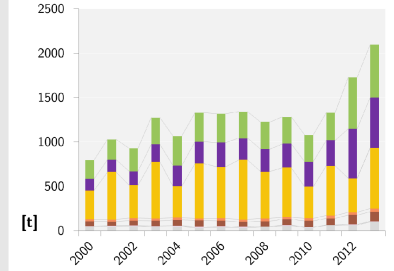
Eritrea
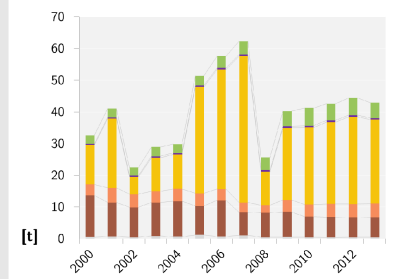
Ethiopia
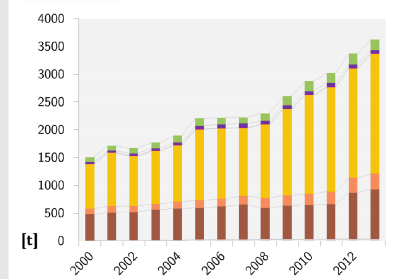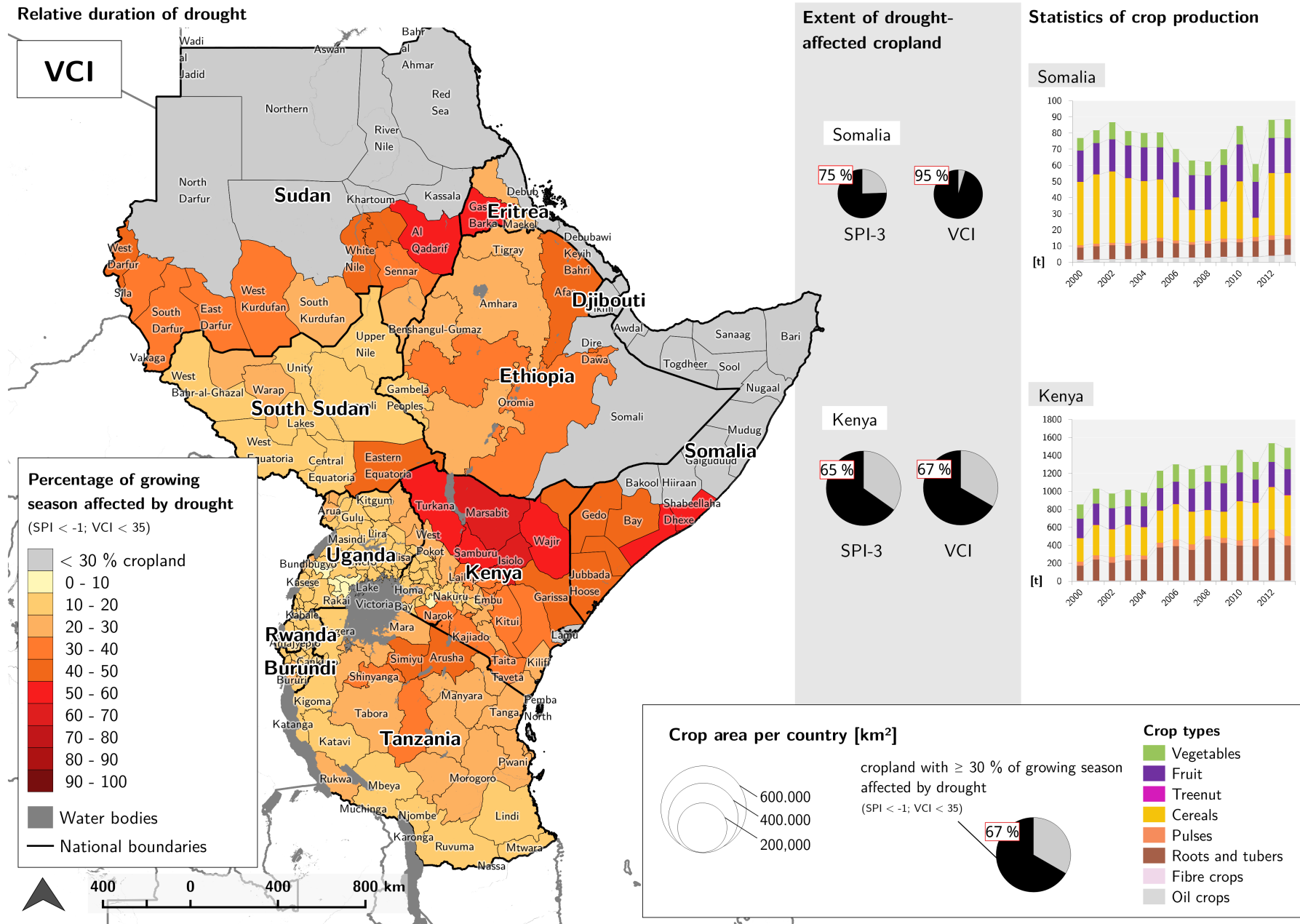
**Figure 5.14:** Agricultural droughts in eastern Africa at regional level during the seasonal year 2011 based on SPI-3 and VCI: Zonal means of relative drought duration (see maps on left panel: top page for SPI-3, bottom page for VCI), drought-affected cropland area per country (pie charts on middle panel) and national statistics of crop production between 2000 and 2016 (bar charts on right panel, FAO, 2016b)

# Chapter 6

# Discussion

## 6.1 Monitoring agricultural droughts over Africa

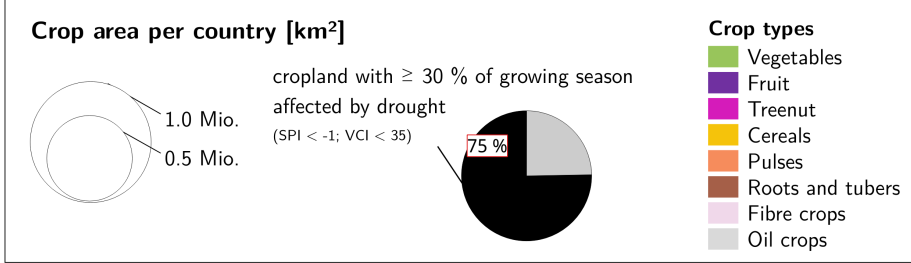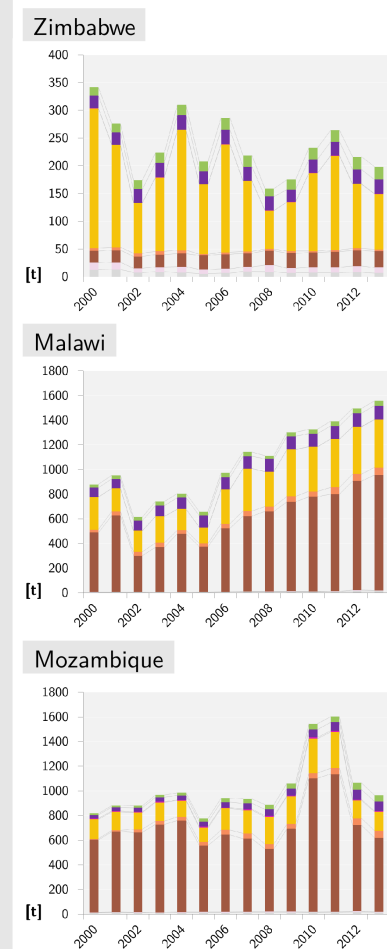**Table 6.1:** Seasonal years and countries of focal regions affected by extensive droughts according to the EM-DAT disaster database (Guha-Sapir et al., 2016). Framed years are in agreement with revealed SPI-3- and VCI-based results (see Table 5.1).

| Years | Countries* affected by drought | |
|---|---|---|
| | Eastern Africa | Southern Africa |
| 2000/01 | SD SO | AO MG MZ NA SZ ZW |
| 2001/02 | UG | LS MW MZ SZ ZW |
| 2002/03 | ET RW TA | LS MG MZ NA SZ ZW |
| 2003/04 | BI ET KE RW SO TA | SZ ZA |
| 2004/05 | BI RW UG SO | AO MW MZ ZM |
| 2005/06 | ET KE RW TA UG | MG MW MZ |
| 2006/07 | RW | SZ ZW |
| 2007/08 | ET UG SO | LS MG MZ MW ZW |
| 2008/09 | BI ER ET KE SO SS UG | MG MZ ZW |
| 2009/10 | BI ET SO SS | MG MZ ZW |
| 2010/11 | BI ET KE SO TA UG | MG ZW |
| 2011/12 | ET KE SD SO TA | AO LS MW ZW |
| 2012/13 | | MW NA ZW |
| 2013/14 | KE SO | NA |
| 2014/15 | KE SD SO | MG NA ZA ZW |
| 2015/16 | ET KE SO SS | BW LS MG MW MZ SZ ZA ZW |

\* Country codes: AO = Angola, BI = Burundi, BW = Botswana, ER = Eritrea, ET = Ethiopia, KE = Kenya, LS = Lesotho, MG = Madagascar, MZ = Mozambique, MW = Malawi, NA = Namibia, RW = Rwanda, SD = Sudan, SO = Somalia, SS = South Sudan, SZ = Swaziland, TA = Tanzania, UG = Uganda, ZA = South Africa, ZM = Zambia, ZW = Zimbabwe

The retrospective analysis of the revealed agricultural droughts over Africa shows that major drought events, which are mentioned in literature (see Section 2.3.3.2) or registered in the EM-DAT disaster database (Guha-Sapir et al., 2016), are largely mirrored in the data. Index-based

spatio-temporal drought patterns denote nearly all officially registered drought years between 2000 and 2016 (see Table 6.1). However, indices uncover a significantly higher amount of agricultural droughts over the selected regions. Here, small-scale drought areas are monitored as well, which may not have led to severe drought effects on a national level and, thus, have not been included in the drought database. All in all, major droughts mentioned in scientific studies could be monitored in this thesis. For eastern Africa, the precipitation deficit in south-eastern Ethiopia during 2009 (Viste et al., 2013), the extensive vegetative drought over Kenya and Tanzania in 2005/06 (Rulinda et al., 2012) as well as the most striking, severe 2010/11 drought period that affected large parts in the Horn of Africa, particularly Ethiopia, Kenya and Somalia (e.g. AghaKouchak, 2015; Anderson et al., 2012; Dutra et al., 2013; Meroni et al., 2014), can be identified. Southern African drought events mentioned in literature such as the prolonged and extensive drought in 2002/03 (Mussá et al., 2015; Rouault and Richard, 2005), the 2007/08 drought period in Zimbabwe (Brown and Funk, 2010; Mutowo and Chikodzi, 2014) and the 2004/05 drought in southern Malawi (Jayanthi et al., 2013) can also be affirmed from the results.

In order to test for the suitability of the presented drought index-based approach on continental drought monitoring, an accurate validation would be necessary. However, this lies beyond the scope of this thesis and, thus, requires further investigation. For this purpose, detailed statistics on agricultural yields, sampled ground truth data or measured rainfall anomalies could be utilized. Despite this lacking detailed evaluation, the general applicability of drought indices SPI-3 and VCI for large-scale drought monitoring over Africa is demonstrated.

Comparing mean drought indices (drought severity) with their respective threshold-based relative duration of droughts (drought persistence) during the average growing season at the continental scale, a good accordance is achieved. Hence, growing seasons that were affected by agricultural droughts with high persistences exhibit generally higher drought severities. However, the latter is relativized by temporal fluctuations of the drought index within the growing season, including wet periods as well. This in turn leads to local differences between drought severity and persistence, which is the case for VCI-derived parameters, where the underlying time series holds higher temporal resolutions.

Although drought patterns indicated by SPI and VCI agree to a large extent, major deviations can be found for several seasonal years. These differences can be explained by the particular characteristics of the drought indices itself. Whereas SPI measures the rainfall deficit from a primarily meteorological point of view, VCI assesses the condition of the vegetation cover. The latter is not only influenced by water availability from precipitation but is also affected by human activities in form of agricultural practices (e.g. irrigation, tillage, fertilization), land use changes (e.g. exploitation of natural resources) and by natural influences like extreme temperatures, fires, pests or plant diseases. These influencing factors can be equally responsible for variations in NDVI, which provides the basis of VCI (Du et al., 2013; Herrmann et al., 2005; Sepulcre-Canto et al., 2012). In this regard, the effect of temperature on evapotranspiration is to mention, which in turn considerably controls vegetation condition (Hayes

et al., 2012). This, however, is neglected in the application of the SPI. Another reason for deviations between the used drought indices are the accumulated effects of rainfall deficits on vegetation condition and its consecutive delayed response. In this regard, the storage of water in the soil reservoir is an important buffer between rainfall events and soil moisture availability for plants, which controls vegetation condition. The magnitude of this temporal delay depends on vegetation type and characteristics, soil conditions, and potential evapotranspiration (Hawinkel et al., 2016). Further, the SPI-3-based rainfall anomalies include events of intense rains that do not necessarily have a positive effect on vegetation condition. Hereby, infiltration to the soil reservoir is minor, since most of the water is lost due to immediate surface run-off (Philippon et al., 2014). What is more, the timing of the rainfall deficit is decisive for the occurrence of vegetative stress and the associated decrease in VCI. This involves both the phase of the growing season and the crop-specific phenological stage affected by drought. Hence, not all rainfall-derived drought events lead to a pronounced vegetation-based drought signal in the data and, vice versa, not all events of vegetative drought occur as a consequence of a rainfall deficit.

## 6.2 Relation of ENSO and agricultural droughts in Africa

### 6.2.1 Effects of ENSO on rainfall anomaly and vegetation condition

On the whole, the revealed temporal correlation patterns between ENSO index MEI and drought indices SPI-3 and VCI are not entirely capable of explaining the complex relation between ENSO and droughts over Africa. However, they rather provide directive information on the occurrence of drier conditions in connection to ENSO warm and cold phases.

A weak to moderate negative relation between MEI and 3-monthly accumulated rainfall anomalies, on the one hand, and vegetation condition, on the other hand, is identified for large parts of southern Africa ($r$ between -0.5 and -0.2). Here, the revealed trend of enhanced drought conditions during high index phases of ENSO agrees with observations from numerous scientific studies (e.g. Brown and Funk, 2010; Meque and Abiodun, 2015; Niang et al., 2014; Propastin et al., 2010; Richard et al., 2000). What is more, the good agreement between both correlation patterns in southern Africa clearly indicates that the impact of ENSO on vegetation-based droughts can mainly be explained through the effect of rainfall. For this area, a high sensitivity of vegetation to rainfall is assumed (Philippon et al., 2014). However, a striking meridional dipole at about 18°S can be observed from the MEI-VCI correlation pattern (see Figure 5.6, right) and monthly VCI images during and after the ENSO peak (see Figure 5.8). This is in accordance with the findings of Philippon et al. (2014). The dipole between a positive (north) and negative relation (south) to ENSO, however, is not matched by SPI-3, which indicates negative correlation coefficients spanning further north of 18°S. In this case, vegetation zones are likely to play a major role for vegetative drought responses to rainfall deficits, since a transition area between southern shrub- and grass-dominated vegetation and northern tree-dominated vegetation can be observed near 18°S

(see Figures 3.4 and 3.5 in Section 3.4; Philippon et al., 2014). Meque and Abiodun (2015) highlighted that the correlation between MEI and rainfall is weaker than correlation between MEI and temperature for this region. Hence, monitoring the influence of ENSO on droughts over southern Africa by only using rainfall data might underestimate the actual effect, in which an enhanced evapotranspiration might play a major role than reduced rainfall.

Eastern African rainfall anomalies and vegetation are sensitive to ENSO during both first (Ethiopian "meher", Somalian "deyr" and Kenyan "short rains" from October to December) and the beginning second growing seasons (Ethiopian "belg", Somalian "gu" and Kenyan "long rains" from February to May) over areas with bimodal rainfall cycles. This is revealed from observed positive relations of both MEI to SPI-3 and MEI to VCI ($r$ between 0.2 and 0.5) with associated positive time lags (see Figure 5.6) matching the timing of respective growing seasons (see Figure 5.1, below). These findings were affirmed by Brown et al. (2010) who identified positive relations between MEI and cumulative NDVI from March to May. A positive correlation between Niño-3.4 SST index and NDVI anomalies over eastern Africa was also proven by Anyamba et al. (2002) who, however, highlighted the additional modulating effect of the Western Indian Ocean on land surface responses to ENSO. However, Philippon et al. (2014) suggested a remarkably weaker effect of ENSO for the secondary, compared to the first growing season, based on long-term analysis of NDVI and its sensitivity to ENSO. In contrast to these large-scale positive ENSO - MEI relation, a negative response of rainfall- and vegetation-related drought indices to El Niño (negative correlation coefficients) is observed over central Ethiopia, Uganda and western Kenya prior to the MEI peak. These findings can be confirmed from Philippon et al. (2014) who identified negative correlations between NDVI and ENSO for August to November during the onset of El Niño. This in turn could directly be connected to preceding rainfall deficits during the rainy season from June to September (Indeje et al., 2000; Preethi et al., 2015). Further, these negatively related areas mainly coincide with zones of intense agricultural production (Philippon et al., 2014). Thus, in eastern Africa, drought response to ENSO is dependent on the climate zone and the corresponding rainfall regime. In this regard, areas showing a bimodal rainfall cycle are more prone to droughts during La Niña, whereas regions with unimodal rainfall distribution exhibit drier conditions in the onset stage of El Niño (Schubert et al., 2016).

As seen in the relatively weak correlation coefficients between ENSO and drought indices, it is by far not sufficient to focus on ENSO as a single explanatory variable for describing the spatio-temporal pattern of agricultural droughts in Africa. Due to the interplay between global atmospheric and oceanic circulation and its variable regional effects, various mechanisms can play an important role for drought occurrence. Funk et al. (2008) revealed a linkage between enhanced convection over the tropical Indian Ocean and a decrease in continental rainfall along the eastern seaboard of Africa based on disruptions of atmospheric circulation and moisture transport from west to east. The crucial role of the Indian Ocean in mediating the impact of ENSO on rainfall variability was further highlighted by Schubert et al. (2016). Besides, ecological characteristics and land use may influence the vegetation-based drought response to ENSO (Hawinkel et al., 2016; Philippon et al., 2014; Propastin et al., 2010).

### 6.2.2 Spatio-temporal variability of ENSO-related drought response

By comparing the impact of individual ENSO events on African rainfall anomalies and vegetation condition for selected months, it is shown that each El Niño and La Niña event leads to a different drought pattern. Thus, although the typical continental-scale teleconnection pattern is broadly confirmed from correlation analyses, no universal ENSO-induced drought effect can be derived for the African continent, since every event shows its distinct spatio-temporal drought response pattern. Accordingly, not every El Niño causes severe drought conditions over southern Africa (as during El Niño 2002/03 and 2015/16), which can be seen in the case of 2009/10. Likewise, droughts in Kenya and Somalia during La Niña are not always as pronounced and extensive as in 2010/11.

Recently, an important influencing factor for the differing effects of ENSO on drought patterns has been discussed in the scientific community, which involves different ENSO variants (Manatsa et al., 2017; Preethi et al., 2015; Ratnam et al., 2014). The so-called "Modoki" type of ENSO differs from the conventional canonical ENSO variant in its signature of SST anomalies over the equatorial Pacific. In this context, El Niño (La Niña) Modoki is associated with an anomalous warming (cooling) of SST in the central Pacific, in contrast to the canonical event that corresponds to the eastern Pacific (Preethi et al., 2015). Both Manatsa et al. (2017) and Ratnam et al. (2014) mention the weak effect of ENSO on precipitation anomalies over southern Africa during the 2009/10 El Niño, which was identified as a Modoki event. Accordingly, heat-induced tropical circulation and tropospheric stationary wave responses are different for Modoki events, which may lead to suppressed negative rainfall anomalies over southern Africa. This might be a possible reason for the revealed poor agreement between 2009/10 and the other studied El Niño events.

What is more, each ENSO event must be put in relation with its large-scale temporal placement. In this regard, Rojas et al. (2014) revealed that the effect of ENSO events differ if either El Niño or La Niña years predominate the corresponding temporal cycle. Such cycles normally consist of several years in which the influence of one ENSO phase overbalances the other. Thus, an El Niño year taking place during a cycle of La Niña dominance, as it was the case during 2009/10, shows less drought impact on agricultural areas than anticipated from previous events being related to El Niño dominance cycles. However, La Niña events during the dominance of El Niño are attributed to bring about extended agricultural droughts (Rojas et al., 2014). It was observed that vegetation-based drought response showed particularly high cumulative effects when La Niña years followed after pronounced El Niño episodes (e.g. 1999/2000 revealed from Anyamba et al., 2002), which was the case for La Niña 2010/11.

Strikingly, deviations between rainfall-based and vegetation-related drought signals were revealed for the area of Zimbabwe, Zambia, Malawi and Mozambique during the major El Niño events. Here, VCI indicates mostly wetter than normal conditions even when pronounced rainfall deficits are observed from SPI. As an explanation for these deviations, the sensitivity of vegetation to rainfall is dependent on climate zones, which in turn are controlled by latitudinal bands of mean annual precipitation. Accordingly, areas of arid and semi-arid

climate zones show higher sensitivity than more humid subtropical zones such as the mentioned regions (Hawinkel et al., 2016; Mutowo and Chikodzi, 2014). What is more, vegetation zones and biomes play an important role on land surface response to rainfall variability. Accordingly, areas with shrub- and grassland-dominated vegetation such as savannah systems or cropland exhibit higher sensitivities to rainfall anomalies than tree-dominated vegetation such as forest and woodland systems, which are located in Zambia and central Mozambique (see Figure 3.5; Hawinkel et al., 2016). Hence, the vegetation type might be a reason for the differing drought patterns for these areas. General reasons for major differences between SPI-3- and VCI-derived drought signals were discussed in section 6.1.

### 6.2.3 ENSO-induced droughts in the context of climate change

In the context of climate change and the associated warming of the atmosphere, hydrological cycles will accelerate on the globe. This likely involves an increased occurrence of hydrological extremes such as floods or droughts and reduces the reliability of water resources over the African continent (Gan et al., 2016; Niang et al., 2014). According to observations from Dai (2011), precipitation and runoff have decreased in African rivers from 1950 to 2008. Further, projections from the Intergovernmental Panel on Climate Change (IPCC) suggest an increased rainfall variability over eastern Africa and an enhanced risk to severe droughts over southern Africa during the course of the 21st century. These conditions of deficient rainfall tend to arise during El Niño events (Niang et al., 2014). Amongst the ENSO-related agricultural droughts in Africa during the past 16 years, which were assessed in this thesis, the currently registered El Niño of 2015/16 stands out as the strongest ENSO event with associated extensive and persistent agricultural droughts over large areas in Africa.

The relation of ENSO and climate change has been a challenging subject for the scientific community. Global climate models still lack the capability of adequately simulating historic ENSO events and, consequently, no consensus is reached on a projected change in frequency of ENSO events in the future (Gizaw et al., 2016). However, current studies suggested a connection between global warming and an increased occurrence of El Niño and La Niña episodes (Cai et al., 2015; Santoso et al., 2013). Accordingly, an augmented occurrence of eastward-propagating warm surface water in the tropical Pacific was projected, which is associated with extreme El Niño events. In response to the increased frequency of strong El Niño episodes, the frequency of La Niña events is expected to rise as well (Cai et al., 2015). This prospect poses new challenges for many African countries, which will be in need of enforcing adaptive measures, capacity building and drought preparedness in order to mitigate the possible impact of prospected droughts. Hereby, the implementation of stable crop pricing policies, promotion of cooperation between governmental institutions and farmers as well as the build-up of infrastructure and improved production technologies can be mentioned as practical measures (Gizaw et al., 2016).

## 6.3 Regional effects of ENSO-related droughts

The comparison of regional drought severity, based on duration and spatial extent of agricultural droughts, with national crop production reveals partial agreements for each of the focal regions. The magnitude of index-derived droughts is not always matched by the statistics of produced crops. In most cases, drought-induced declines in production can only be observed for particular crop types and dynamics of total production do not fit with revealed drought severity. The analysed drought years, however, had an impact on national crop production. The effect of the 2002/03 drought over southern Africa could be observed in anomalously low production numbers for cereals and pulses in Namibia, roots and tubers in Botswana, cereals, roots and tubers in South Africa and Swaziland, cereals in Zimbabwe, roots and tubers in Malawi as well as cereals and treenuts in Mozambique. However, regarding the overall crop production of 2002/03, distinctive slumps can only be identified for Zimbabwe and Malawi. Slight downturns of crop production in this period were observed in Botswana and Swaziland, whereas the drought-related effect on Namibian and South African crop statistics was not as apparent as expected from the presented index-based analyses (see charts in Figure 5.13).

In eastern Africa, crop statistics largely mirror the revealed results of index-based drought severity. Accordingly, droughts in 2010/11 had strong effects on cereal production of Somalia as well as on cereal, vegetable and fruit production of Kenya, where, above all, a considerable slump in total crop production was observed for the corresponding year. These countries are located in the core zone of the observed agricultural drought of 2010/2011, which affected a large portion of cropland and proved to be highly persistent during the growing seasons. Hence, statistical data and observed index-based drought severity are generally coherent during 2010/11 (see charts in Figure 5.14).

However, several factors restrict the validity of the revealed regional drought impact and its accordance with national statistics on crop production. Firstly, the used relatively coarse cropland mask (about 10 km spatial resolution) that is based on a rather permissive threshold, including all areas of more than 0 % of cropland fraction, constitutes a restriction on the examination of regional impacts of agricultural droughts. As an example, the revealed severity of the 2002/03 drought is misleading and must be treated with caution in the case of Namibia. Mixed land use systems of pasture management and small-scale farming are a common feature of Namibian agriculture (Lange et al., 2012). Here, areas containing a mixture of savannah grassland, pasture and scattered, small-scale cropland are included in the analyses. Hence, the indicated drought severity largely includes non-cropland areas, which were affected by droughts and, thus, tamper the validity of the regional impact of drought on crop production.

What is more, there is no linear relationship between agricultural droughts and crop production. The amount of produced crops in a country does not only depend on rainfall and vegetation condition but also on political and socio-economic factors. In this regard, drivers for decreased crop production can be national pricing policies, infrastructural problems, conflicts, trade-related issues, resource mismanagements or administrative changes involving taxes or land reforms (Funk and Budde, 2009; Funk et al., 2008). The interplay of natural and political

drivers for food insecurity becomes clear in the case of Zimbabwe. Here, the land reform of 2000 led to a food and economic crisis caused by the almost complete cessation of organized agricultural activity in formerly commercial farm areas. The resettlement of landless people on farms without the necessary provision of seeds, tools and know-how led to a heavy decline in agricultural production after 2000 (Brown and Funk, 2010). Thus, rainfall deficits and induced vegetative stress in 2002/03 are not the only explanatory variables for the observed downturn in crop production in 2003 (see chart for Zimbabwe on right panel of Figure 5.13, bottom page).

Vice versa, drought-induced negative effects on crop production could be mitigated by improved technology and management practices like efficient irrigation or adapted agricultural measures involving the planting of alternative crops or increases in productivity (Stige et al., 2006). As an example, Ethiopia registered a steady increase in crop production from 2000 to 2013, which is based on the continuous rise of produced cereals dominating the Ethiopian crop production (see chart for Ethiopia on right panel of Figure 5.14, top page). Due to an increasing intensification since 2000, yield growth was faster than acreage expansion for Ethiopian cereal production. Consequently, an increased productivity led to yield improvements causing production growth (Taffesse et al., 2013). This is indicated in the overall upward trend of Ethiopian cereal production, which superimposes the possible effects of agricultural droughts on crop production numbers. Further, the influence of political incentives and macroeconomic reforms on maize production in Kenya was examined by Onono et al. (2013) who revealed a lagged positive response of production numbers (1972-2008) to governance reforms and development expenditures in agriculture.

What is more, the level 1 GADM data set shows significant differences in size for each country, holding its individual administrative division. This influences the visual pattern of revealed drought severity in indirectly emphasizing large regions. Hereby, the region-specific percentages of cropland is not apparent in the displayed maps of Figures 5.13 and 5.14, leading to an inadvertent overrepresentation of larger regions compared to smaller ones. Other factors restraining the comparison of remote sensing-based indicators for drought severity with crop production numbers are uncertainties that inhere the underlying methodology of this thesis. Here, assumptions on used thresholds, the used broad-scale crop mask and a possible error propagation originating from inconsistencies in remote sensing products are to mention. Further, the relatively short reference period of 16 years, which was used for statistical multi-year analyses, could have led to errors in the extracted average growing season, which in turn was taken as a basis for the detection of agricultural droughts.

## 6.4 Potential and limitations

As demonstrated in this thesis, a comprehensive insight into the spatio-temporal dynamics of large-scale drought patterns is gained by means of the analysis of remote sensing-based drought indices. Additionally, their corresponding relation to the ENSO mechanism was illuminated in form of revealed correlation and response time patterns. On the one hand,

the applied methodology yields promising results, providing the basis for potential further research. On the other hand, it has to be considered that the used approach holds certain limitations.

As a first constraint, the suitability of the used cropland data set is to mention. The relatively coarse EarthStat 2000 data of cropland fraction per pixel (EarthStat, 2008) does not serve the purpose of accurately delimiting African cropland areas. Thus, no exclusive spatial focus on cropland but a rather broad assessment of agriculturally relevant areas was given in the presented analyses. This meets the requirement of providing a broad-scale picture of agricultural droughts, which was imposed in this thesis. However, the use of a data set with a higher spatial resolution and accuracy could improve the level of detail for further adapted studies. However, such data sets do either not cover the whole African continent or contain limitations in terms of data acquisition and accuracy (See et al., 2015). What is more, the statistical validity of the applied cross-correlation has to be discussed. Only weak to moderate linear relations between ENSO and drought indices over Africa could be revealed, whereas some proved to be non-significant. This relative weakness of the relationships could originate from conceptual and methodological limitations. Firstly, the correlation was carried out with the complete time series, regardless of the timing of ENSO events. Thus, all types of ENSO phases were included in the analyses. However, ENSO teleconnections over Africa are asymmetrical in nature (Philippon et al., 2014). This may have caused underestimations of the strengths of correlation between ENSO and drought indices over areas where rainfall anomalies or vegetation condition are more (less) sensitive to El Niño and less (more) sensitive to La Niña. For further research, partial correlation analyses are suggested, separately examining the relation of drought indices to El Niño and the relation of drought indices to La Niña events. Secondly, the study period may not be sufficiently long to serve as a reference period for multi-year statistical analyses. This limits the explanatory power of derived relationships between drought occurrence and ENSO and further bears on the significance of the used drought indices. Nevertheless, comparability of all indices is given, due to they are based on the same reference period.

Here, it must be noted that the availability of MODIS data (from February/March 2000) accounts for the relatively short study period focussed in this thesis. However, only SPOT-Vegetation (SPOT-VGT) or Proba-V satellite images can be named as alternatives similar to MODIS. SPOT-VGT data covers the same study period (available since 1998), but provides lower spatial resolutions (1 km) than the used MODIS data. Proba-V offers lower (1 km) and higher spatial resolutions (up to 100 m), but data availability is limited to the period after 2013 (Dierckx et al., 2014; Maisongrande et al., 2004). As mentioned before, AVHRR data offers a long image record beginning in the early 1980s. However consistent data over Africa is only available at course spatial resolutions, which limits its application for continental-scale drought monitoring (Townshend and Justice, 2002).

Other restrictions originate from the used remotely sensed data as proxy for rainfall- and vegetation-based droughts. The TRMM data set, which was used for calculating the SPI, includes uncertainties that lead to errors in rainfall estimates. For Africa, uncertainties are

mainly related to areas with complex topography or humid climate (Dinku et al., 2007; Naumann et al., 2012). Further, calculations of VCI are based on NDVI as an index for vegetation vigour. However, NDVI holds certain limitation. As an example, the sensitivity to soil moisture leads to soil-related effects on NDVI over sparsely vegetated areas. Other weaknesses of NDVI are its tendency of saturation in densely vegetated areas as well as observed atmospheric interferences related to aerosols and clouds (Zargar et al., 2011).

What is more, studying the relation between rainfall- and vegetation-based droughts over Africa and the underlying sensitivity of vegetation to rainfall deficits lies beyond the scope of this thesis and merits further research. Moreover, validation and an uncertainty analysis remain outstanding issues, which could possibly be assessed in a larger study framework. Furthermore, for examining the relation between ENSO and agricultural droughts over Africa, additional influencing factors should be considered. Here, multiple regression analyses and testing for non-linear relations are suggested in order to quantify the connection between ENSO and rainfall deficits.

As a strength of this work, the applicability of drought indices SPI and VCI for monitoring agricultural droughts on a continental scale was proven. Hereby, the usage of remote sensing data as a basis for rainfall- and vegetation-related drought detection accounted for consistent and comprehensive information on the dynamics of drought patterns during the average growing seasons of 2000-2016. Feasible and coherent results were revealed on a both spatial and temporal scale, showing a general agreement with recorded data and findings from related previous works. Furthermore, the usage of two different drought indices illuminated both rainfall as the main trigger and vegetation as a land surface response to drought. Therefore, agricultural droughts could be assessed from two complementary perspectives.

Moreover, the complex relation between agricultural droughts in Africa and ENSO could be illuminated in its fundamentals. For significantly correlated areas, the directions and strengths of correlation are in general accordance with previous studies. It was shown that droughts stand in relation to ENSO dynamics over certain regions of Africa. The findings and information drawn from this analyses can contribute to a better understanding of drought occurrence in connection to ENSO on the African continent. Such knowledge is crucial and forms the basis for implementing strategies of drought hazard mitigation. In particular, analyses of remote sensing time series, as carried out in this work, provide a more continuous monitoring of agricultural droughts on large scales and may contribute to improved drought prediction. The forecast of future droughts depends on accurate retrospective monitoring and becomes increasingly important for taking measures to reduce the impacts of severe droughts on society. On this basis, precautions could be made by local authorities and timely humanitarian aid can be given to drought-affected regions in case of extensive crop failures and food shortage.

# Chapter 7

# Conclusion

In the course of this thesis, the spatio-temporal evolution of agricultural droughts over Africa and their connection to ENSO events during the last 16 years were examined by applying two different drought indices. Based on remotely sensed rainfall anomalies (SPI) and surface reflectance data related to vegetation condition (VCI), large-scale patterns of agricultural droughts affecting the average growing season could be identified. Further, the relation between drought indices and ENSO could be described in its fundamentals. The analysis was based on a pixel-by-pixel cross-correlation between the time series of each drought index and the ENSO index MEI. In doing so, the response times of agricultural droughts to ENSO events were analysed.

In general, droughts are recurrent phenomena over most African regions. These were monitored in terms of drought severity, expressed as the mean drought index, and the relative duration of droughts during the average growing seasons per year. For eastern Africa, 2009 and 2011 could be revealed as major drought years, whereas southern Africa was affected by particularly severe droughts in 2003 and 2015/16. Additionally, numerous regional-scale droughts could be detected. The findings are in broad accordance with major recorded drought events, either officially registered or revealed from previous related studies. The applicability of SPI and VCI as indices for comprehensive drought monitoring on a continental scale was proven in this work. Differences between the drought signals derived from each of the used indices could be explained by the complex relationship between rainfall anomalies and vegetation condition, which by itself is influenced by multiple environmental parameters.

Regarding the connection between droughts and ENSO, revealed correlation patterns exhibit generally low to moderate relations between MEI and drought indicators over Africa. Hereby, a tendency of droughts during El Niño could be deduced from the observed negative correlation coefficients over large parts of southern Africa. A meridional dipole pattern between extensive, negatively correlated southern areas and a smaller, positively correlated northern part was identified over the region. Here, the effect of ENSO on vegetation condition could mainly be explained through the influence of rainfall. In contrast, eastern Africa exhibits a correlation pattern with an indicated east-west dipole: Zones with bimodal annual rainfall cycles over eastern Kenya, southern Ethiopia and Somalia tend to respond with droughts

to La Niña events, whereas drought tendencies during the onset of El Niño were revealed for areas with unimodal rainfall cycles in central Ethiopia, Rwanda and Uganda. In both southern and eastern Africa, major deviations between rainfall-related and vegetation-based responses to ENSO are controlled by climate and dominant vegetation cover.

By studying drought patterns for each of the major ENSO events from 2000 to 2016, it could be concluded that every El Niño and La Niña episode shows its distinct signal of rainfall- and vegetation-related droughts. All in all, no universal spatio-temporal drought response to a certain ENSO phase could be derived. In this regard, the effect of different ENSO variants (modoki and canonical events) as well as the influence of multi-year cycles with either El Niño or La Niña dominance were discussed as possible explanations for the differing drought responses.

The impact of the selected drought years 2002/03 (El Niño) and 2010/11 (La Niña) on agriculture was analysed by comparing the index-based duration of droughts and the extent of drought-affected cropland with national statistics of annual crop production in the corresponding focal regions. Thereby, the 2002/03 droughts were related to southern Africa, whereas impacts of the 2010/11 droughts were shown for eastern Africa. Decreases in production numbers of major crop types could be linked to the effect of agricultural droughts for some of the major drought-affected countries. However, crop production is also regulated by political and socio-economic factors, which limits the direct comparison of observed regional-scale drought severity with national statistical data.

To overcome the limitations of the underlying methodology, the incorporation of more accurate cropland data as well as enhancements of the correlation analysis in terms of statistical validity and a separate assessment of El Niño and La Niña periods form subjects of further investigation. Moreover, a comprehensive validation and the assessment of uncertainty would be required for derivative works in a larger framework. Studying the relation between rainfall-based SPI and vegetation-related VCI over Africa could provide a better understanding of land surface responses to rainfall deficits, which in turn influences the evolution of agricultural droughts. For accurately describing the relation between ENSO and droughts, a multiple regression analysis in consideration of additional variables and tests for non-linearity are proposed.

All in all, a comprehensive insight into spatio-temporal drought dynamics was gained through this thesis. The usage of remotely sensed input data for drought indices SPI and VCI provided a complementary perspective on agricultural droughts based on both rainfall and vegetation condition. Above all, the complex relationship between ENSO and drought evolution over Africa could be illustrated in its fundamentals. This is regarded essential for better understanding the interconnections between global climate oscillations and rainfall anomalies over Africa, illuminating dependencies of agricultural droughts. Here, the opportunities of drought monitoring provided by advanced remote sensing techniques and the increased availability of earth observation data will likely continue contributing to establish a solid knowledge base related to droughts. Altogether, this lays the foundation for decision making and capacity building to mitigate the effects of severe droughts and adapt to existent drought hazards.

# References

AghaKouchak, A. (2015). A multivariate approach for persistence-based drought prediction: Application to the 2010-2011 East Africa drought. *Journal of Hydrology*, 526:127–135.

AghaKouchak, A., Farahmand, A., Melton, F. S., Teixeira, J., Anderson, M. C., Wardlow, B. D., and Hain, C. R. (2015). Remote sensing of drought: Progress, challenges and opportunities. *Reviews of Geophysics*, 53:1–29.

Allan, R. J. (2000). ENSO and climatic variability in the last 150 years. In Diaz, H. F. and Markgraf, V., editors, *El Niño and the Southern Oscillation: Multiscale Variability, Global and Regional Impacts*, chapter 1, pages 3–56. Cambridge University Press, Cambridge.

Anderson, W. B., Zaitchik, B. F., Hain, C. R., Anderson, M. C., Yilmaz, M. T., Mecikalski, J., and Schultz, L. (2012). Towards an integrated soil moisture drought monitor for East Africa. *Hydrology and Earth System Sciences*, 16:2893–2913.

Anyamba, a. and Eastman, J. R. (1996). Interannual variability of NDVI over Africa and its relation to El Niño/Southern Oscillation. *International Journal of Remote Sensing*, 17(13):2533–2548.

Anyamba, A. and Tucker, C. (2012). Historical perspective of AVHRR NDVI and vegetation drought monitoring. In Wardlow, B. D., Anderson, M. C., and Verdin, J. P., editors, *Remote Sensing of Drought: Innovative Monitoring Approaches*, chapter 2, pages 23–49. CRC Press, Boca Raton.

Anyamba, A. and Tucker, C. J. (2005). Analysis of Sahelian vegetation dynamics using NOAA-AVHRR NDVI data from 1981-2003. *Journal of Arid Environments*, 63(3):596–614.

Anyamba, A., Tucker, C. J., and Eastman, J. R. (2001). NDVI anomaly patterns over Africa during the 1997/98 ENSO warm event. *International Journal of Remote Sensing*, 22(10):1847–1859.

Anyamba, A., Tucker, C. J., and Mahoney, R. (2002). From El Niño to La Niña: Vegetation response patterns over east and southern Africa during the 1997-2000 period. *Journal of Climate*, 15(21):3096.

Asadi Zarch, M. A., Sivakumar, B., and Sharma, A. (2015). Droughts in a warming climate: A global assessment of Standardized precipitation index (SPI) and Reconnaissance drought index (RDI). *Journal of Hydrology*, 526:183–195.

Awange, J., Schumacher, M., Forootan, E., and Heck, B. (2016a). Exploring hydrometeorological drought patterns over the Greater Horn of Africa (1979–2014) using remote sensing and reanalysis products. *Advances in Water Resources*, 94:45–59.

Awange, J. L., Ferreira, V. G., Forootan, E., Khandu, Andam-Akorful, S. A., Agutu, N. O., and He, X. F. (2016b). Uncertainties in remotely sensed precipitation data over Africa. *International Journal of Climatology*, 36:303–323.

Baldridge, A. M., Hook, S. J., Grove, C. I., and Rivera, G. (2009). The ASTER spectral library version 2.0. *Remote Sensing of Environment*, 113(4):711–715.

Barnston, A. G., Chelliah, M., and Goldenberg, S. B. (1997). Documentation of a highly ENSO-related SST region in the equatorial Pacific: Research note. *Atmosphere-Ocean*, 35(3):367–383.

Bjerknes, J. (1969). Atmospheric teleconnections from the equatorial Pacific. *Monthly Weather Review*, 97(3):163–172.

Brandt, M., Romankiewicz, C., Spiekermann, R., and Samimi, C. (2014). Environmental change in time series - An interdisciplinary study in the Sahel of Mali and Senegal. *Journal of Arid Environments*, 105:52–63.

Brown, M. E., de Beurs, K., and Vrieling, A. (2010). The response of African land surface phenology to large scale climate oscillations. *Remote Sensing of Environment*, 114(10):2286–2296.

Brown, M. E. and Funk, C. C. (2010). Early Warning of Food Security Crises in Urban Areas: The Case of Harare, Zimbabwe, 2007. In *Geospatial Techniques in Urban Hazard and Disaster Analysis*, pages 229–241. Springer.

Byun, H. R. and Wilhite, D. A. (1999). Objective quantification of drought severity and duration. *Journal of Climate*, 12(9):2747–2756.

Cai, W., Santoso, A., Wang, G., Yeh, S.-w., An, S.-i., Cobb, K. M., Collins, M., Guilyardi, E., Jin, F.-f., Kug, J.-s., Lengaigne, M., and Mcphaden, M. J. (2015). ENSO and greenhouse warming. *Nature Climate Change*, 5:849–859.

Chisadza, B., Tumbare, M. J., Nyabeze, W. R., and Nhapi, I. (2015). Linkages between local knowledge drought forecasting indicators and scientific drought forecasting parameters in the Limpopo River Basin in Southern Africa. *International Journal of Disaster Risk Reduction*, 12(2015):226–233.

Choi, M., Jacobs, J. M., Anderson, M. C., and Bosch, D. D. (2013). Evaluation of drought indices via remotely sensed data with hydrological variables. *Journal of Hydrology*, 476:265–273.

Crétat, J., Richard, Y., Pohl, B., Rouault, M., Reason, C., and Fauchereau, N. (2012). Recurrent daily rainfall patterns over South Africa and associated dynamics during the core of the austral summer. *International Journal of Climatology*, 32(2):261–273.

Dai, A. (2011). Drought under global warming: A review. *Wiley Interdisciplinary Reviews: Climate Change*, 2(1):45–65.

Database of Global Administrative Areas (GADM) (2015). Global Administrative Areas. Boundaries without limits: GADM database of Global Administrative Areas. [data file] http://gadm.org/version2 (Retrieved: 17/10/16).

Deng, M. X., Di, L. P., Han, W. G., Yagci, A. L., Peng, C. M., and Heo, G. (2013). Web-service-based Monitoring and Analysis of Global Agricultural Drought. *Photogrammetric Engineering and Remote Sensing*, 79(10):929–943.

Dierckx, W., Sterckx, S., Benhadj, I., Livens, S., Duhoux, G., Achteren, T. V., Francois, M., Mellab, K., and Saint, G. (2014). PROBA-V mission for global vegetation monitoring: standard products and image quality. *International Journal of Remote Sensing*, 35(7):2589–2614.

Dinku, T., Ceccato, P., Grover-Kopec, E., Lemma, M., Connor, S. J., and Ropelewski, C. F. (2007). Validation of satellite rainfall products over East Africa's complex topography. *International Journal of Remote Sensing*, 28(7):1503–1526.

Domenikiotis, C., Spiliotopoulos, M., Tsiros, E., and Dalezios, N. R. (2004). Early cotton yield assessment by the use of the NOAA/AVHRR derived Vegetation Condition Index (VCI) in Greece. *International Journal of Remote Sensing*, 25(14):2807–2819.

Dracup, J. A., Lee, K. S., and Paulson Jr., E. G. (1980). On the definition of droughts. *Water Resources Research*, 16(2):297–302.

Du, L., Tian, Q., Yu, T., Meng, Q., Jancso, T., Udvardy, P., and Huang, Y. (2013). A comprehensive drought monitoring method integrating MODIS and TRMM data. *International Journal of Applied Earth Observation and Geoinformation*, 23(1):245–253.

Du Bois, W. E. B. and Gates, H. (2014). *Africa, Its Geography, People and Products and Africa, Its Place in Modern History*. Oxford W. E. B. Du Bois. Oxford University Press, Incorporated.

Dutra, E., Magnusson, L., Wetterhall, F., Cloke, H. L., Balsamo, G., Boussetta, S., and Pappenberger, F. (2013). The 2010-2011 drought in the Horn of Africa in ECMWF reanalysis and seasonal forecast products. *International Journal of Climatology*, 33(7):1720–1729.

EarthStat (2008). Cropland and Pasture Area in 2000, Global Landscape Initiative, Institute on the Environment, University of Minnesota, UBC. [data file] http://www.earthstat.org/data-download/ (Retrieved: 06/08/16).

Eerens, H., Haesen, D., Rembold, F., Urbano, F., Tote, C., and Bydekerke, L. (2014). Image time series processing for agriculture monitoring. *Environmental Modelling and Software*, 53:154–162.

Eklundh, L. and Jönsson, P. (2015). TIMESAT: A Software Package for Time-Series Processing and Assessment of Vegetation Dynamics. In Kuenzer, C., Dech, S., and Wagner, W., editors, *Remote Sensing Time Series*, chapter 7, pages 141–158. Springer, Cham.

ESA Climate Change Initiative (2011). Land Cover project 2014-2017. [data file], http://www.esa-landcover-cci.org/?q=node/158 (Retrieved: 29/10/16).

Exelis Visual Information Solutions (2016). C_CORRELATE, HARRIS. http://www.harrisgeospatial.com/docs/C_CORRELATE.html (Accessed: 17/12/16).

Fontaine, B., Gaetani, M., Ullmann, A., and Roucou, P. (2011). Time evolution of observed July-September sea surface temperature-Sahel climate teleconnection with removed quasi-global effect (1900–2008). *Journal of Geophysical Research*, 116:D04105.

Food and Agriculture Organization of the United Nations (FAO) (2016a). El Niño set to have a devastating impact on southern Africa's harvests and food security. Joint statement by FAO, EC-JRC, FEWS NET and WFP. http://www.fao.org/news/story/en/item/382932/icode/ (Accessed: 10/01/17).

Food and Agriculture Organization of the United Nations (FAO) (2016b). Food and Agriculture Organization Corporate Statistical Database (FAOSTAT): Crop statistics. [data file], http://www.fao.org/faostat/en/#data (Retrieved: 29/10/16).

Funk, C. (2011). We thought trouble was coming. *Nature*, 476:7.

Funk, C. and Budde, M. E. (2009). Phenologically-tuned MODIS NDVI-based production anomaly estimates for Zimbabwe. *Remote Sensing of Environment*, 113(1):115–125.

Funk, C., Dettinger, M. D., Michaelsen, J. C., Verdin, J. P., Brown, M. E., Barlow, M., and Hoell, A. (2008). Warming of the Indian Ocean threatens eastern and southern African food security but could be mitigated by agricultural development. *Proceedings of the National Academy of Sciences of the United States of America*, 105(32):11081–11086.

Gan, T. Y., Ito, M., Huelsmann, S., Qin, X., Lu, X., Liong, S. Y., Rutschman, P., Disse, M., and Koivosalo, H. (2016). Possible climate change/variability and human impacts, vulnerability of African drought prone regions, its water resources and capacity building. *Hydrological Sciences Journal*, 61(7):1209–1226.

Gao, B. C. (1996). NDWI - A normalized difference water index for remote sensing of vegetation liquid water from space. *Remote Sensing of Environment*, 58(3):257–266.

Gebrehiwot, T., Veen, A. V. D., and Maathuis, B. (2011). Spatial and temporal assessment of drought in the Northern highlands of Ethiopia. *International Journal of Applied Earth Observations and Geoinformation*, 13(3):309–321.

GEOGLAM (2016). Crop Monitor for Early Warning: No. 1 - February 2016. *Early Warning Crop Monitor*, 1:1–4.

Ghulam, A., Qin, Q., and Zhan, Z. (2007). Designing of the perpendicular drought index. *Environmental Geology*, 52(6):1045–1052.

Gizaw, M. S., Thian, ·., and Gan, Y. (2016). Impact of climate change and El Niño episodes on droughts in sub-Saharan Africa. *Climate Dynamics*, pages 1–18.

Golden Gate Weather Service (2016). El Niño and La Niña years and intensities based on Oceanic Niño Index (ONI). http://ggweather.com/enso/oni.htm (Accessed: 10/08/16).

Guha-Sapir, D., Below, R., and Hoyois, P. (2016). EM-DAT: The CRED/OFDA International Disaster Database, Université Catholique de Louvain. www.emdat.be (Accessed: 02/11/16).

Hanley, D. E., Bourassa, M. A., O'Brien, J. J., Smith, S. R., and Spade, E. R. (2003). A quantitative evaluation of ENSO indices. *Journal of Climate*, 16(8):1249–1258.

Hao, Z., AghaKouchak, A., Nakhjiri, N., and Farahmand, A. (2014). Global integrated drought monitoring and prediction system. *Scientific Data*, 1(Nr. 140001).

Hawinkel, P., Thiery, W., Lhermitte, S., Swinnen, E., Verbist, B., Van Orshoven, J., and Muys, B. (2016). Vegetation response to precipitation variability in East Africa controlled by biogeographical factors. *Journal of Geophysical Research: Biogeosciences*, 121:2422–2444.

Hayes, M. J., Svoboda, M. D., Wardlow, B. D., Anderson, M. C., and Kogan, F. (2012). Drought Monitoring Historical and Current Perspectives. In Wardlow, B. D., Anderson, M. C., and Verdin, J. P., editors, *Remote Sensing of Drought: Innovative Monitoring Approaches*, chapter 1, pages 1–19. CRC Press, Boca Raton.

Herrmann, S. M., Anyamba, A., and Tucker, C. J. (2005). Recent trends in vegetation dynamics in the African Sahel and their relationship to climate. *Global Environmental Change*, 15(4):394–404.

Heumann, B. W., Seaquist, J. W., Eklundh, L., and J??nsson, P. (2007). AVHRR derived phenological change in the Sahel and Soudan, Africa, 1982-2005. *Remote Sensing of Environment*, 108(4):385–392.

Huete, A., Didan, K., Miura, T., Rodriguez, E. P., Gao, X., and Ferreira, L. G. (2002). Overview of the radiometric and biophysical performance of the MODIS vegetation indices. *Remote Sensing of Environment*, 83:195–213.

Huete, A. R. (1988). A soil-adjusted vegetation index (SAVI). *Remote Sensing of Environment*, 25(3):295–309.

Huffman, G. J., Bolvin, D. T., Nelkin, E. J., Wolff, D. B., Adler, R. F., Gu, G., Hong, Y., Bowman, K. P., and Stocker, E. F. (2007). The TRMM Multisatellite Precipitation Analysis (TMPA): Quasi-Global, Multiyear, Combined-Sensor Precipitation Estimates at Fine Scales. *Journal of Hydrometeorology*, 8(1):38–55.

Indeje, M., Semazzi, F. H. M., and Ogallo, L. J. (2000). ENSO signals in East African rainfall seasons. *International Journal of Climatology*, 20:19–46.

Jayanthi, H., Husak, G. J., Funk, C., Magadzire, T., Chavula, A., and Verdin, J. P. (2013). Modeling rain-fed maize vulnerability to droughts using the standardized precipitation index from satellite estimated rainfallamp - Southern Malawi case study. *International Journal of Disaster Risk Reduction*, 4:71–81.

Jones, A., Breuning-Madsen, H., Brossard, M., Dampha, A., Deckers, J., Dewitte, O., Gallali, T., Hallett, S., Jones, R., Kilasara, M., Le Roux, P., Micheli, E., Montanarella, L., Spaargaren, O., Thiombiano, L., Van Ranst, E., Yemefack, M., and R., Z., editors (2013). *Soil atlas of Africa*. European Commission, Publications Office of the European Union, Luxembourg.

Karlson, M. and Ostwald, M. (2016). Remote sensing of vegetation in the Sudano-Sahelian zone: A literature review from 1975 to 2014. *Journal of Arid Environments*, 124:257–269.

Karnieli, A., Agam, N., Pinker, R. T., Anderson, M., Imhoff, M. L., Gutman, G. G., Panov, N., and Goldberg, A. (2010). Use of NDVI and land surface temperature for drought assessment: Merits and limitations. *Journal of Climate*, 23(3):618–633.

Keyantash, J. and Dracup, J. A. (2002). The quantification of drought: An evaluation of drought indices. *Bulletin of the American Meteorological Society*, 83(8):1167–1180.

Keyantash, J. and National Center for Atmospheric Research Staff (2016). The Climate Data Guide: Standardized Precipitation Index (SPI). https://climatedataguide.ucar.edu/climate-data/standardized-precipitation-index-spi (Accessed: 19/11/16).

Klisch, A. and Atzberger, C. (2016). Operational drought monitoring in Kenya using MODIS NDVI time series. *Remote Sensing*, 8(4).

Knauer, K., Gessner, U., Dech, S., and Kuenzer, C. (2014). Remote sensing of vegetation dynamics in West Africa. *International Journal of Remote Sensing*, 35(17):6357–6396.

Kogan, F. and Sullivan, J. (1993). Development of global drought-watch system using NOAA/AVHRR data. *Advances in Space Research*, 13(5):219–222.

Kogan, F., Yang, B., Guo, W., Pei, Z., and Jiao, X. (2005). Modelling corn production in China using AVHRR-based vegetation health indices. *International Journal of Remote Sensing*, 26(11):2325–2336.

Kogan, F. N. (1990). Remote sensing of weather impacts on vegetation in non-homogeneous areas. *International Journal of Remote Sensing*, 11(8):1405–1419.

Kogan, F. N. (1995). Application of vegetation index and brightness temperature for drought detection. *Advances in Space Research*, 15(11):91–100.

Kogan, F. N. (2000). Satellite-observed sensitivity of world land ecosystems to El Niño/La Niña. *Remote Sensing of Environment*, 74(3):445–462.

Kuenzer, C., Zhao, D., Scipal, K., Sabel, D., Naeimi, V., Bartalis, Z., Hasenauer, S., Mehl, H., Dech, S., and Wagner, W. (2009). El Niño southern oscillation influences represented in ERS scatterometer-derived soil moisture data. *Applied Geography*, 29(4):463–477.

Lange, F., Schneiderat, U., and Steinbach, J. (2012). Performance, management and objectives of cattle farming on communal ranges in Namibia. *Journal of Arid Environments*, 80:65–73.

Lloyd-Hughes, B. (2014). The impracticality of a universal drought definition. *Theoretical and Applied Climatology*, 117(3-4):607–611.

Lloyd-Hughes, B. and Saunders, M. A. (2002). A drought climatology for Europe. *International Journal of Climatology*, 22(13):1571–1592.

Lott, F. C., Christidis, N., and Stott, P. A. (2013). Can the 2011 East African drought be attributed to human-induced climate change? *Geophysical Research Letters*, 40:1177–1181.

Lydolph, P. E. (1985). *The Climate of the Earth*. G - Reference, Information and Interdisciplinary Subjects Series. Roman & Allanheld.

Lyon, B. (2004). The strength of El Niño and the spatial extent of tropical drought. *Geophysical Research Letters*, 31:L21204.

Maisongrande, P., Duchemin, B., and Dedieu, G. (2004). VEGETATION/SPOT: an operational mission for the Earth monitoring; presentation of new standard products. *International Journal of Remote Sensing*, 25(1):9–14.

Manatsa, D., Mushore, T., and Lenouo, A. (2017). Improved predictability of droughts over southern Africa using the standardized precipitation evapotranspiration index and ENSO. *Theoretical and Applied Climatology*, 127:259–274.

Masih, I., Maskey, S., Mussá, F. E. F., and Trambauer, P. (2014). A review of droughts on the African continent: A geospatial and long-term perspective. *Hydrology and Earth System Sciences*, 18(9):3635–3649.

Mbow, C., Brandt, M., Ouedraogo, I., de Leeuw, J., and Marshall, M. (2015). What four decades of earth observation tell us about land degradation in the Sahel? *Remote Sensing*, 7(4):4048–4067.

McKee, T. B., Doesken, N. J., and Kleist, J. (1993). The relationship of drought frequency and duration to time scales. In *AMS 8th Conference on Applied Climatology*, pages 179–184, Anaheim.

McPhaden, M. J., Zebiak, S. E., and Glantz, M. H. (2006). ENSO as an integrating concept in earth science. *Science (New York, N.Y.)*, 314(5806):1740–1745.

Meque, A. and Abiodun, B. J. (2015). Simulating the link between ENSO and summer drought in Southern Africa using regional climate models. *Climate Dynamics*, 44:1881–1900.

Meroni, M., Verstraete, M. M., Rembold, F., Urbano, F., and Kayitakire, F. (2014). A phenology-based method to derive biomass production anomalies for food security monitoring in the Horn of Africa. *International Journal of Remote Sensing*, 35(7):2472–2492.

Meyer, S. J., Hubbard, K. G., and Wilhite, D. A. (1993). A Crop-Specific Drought Index for Corn: I. Model Development and Validation. *Agronomy Journal*, 85(2):388–395.

Mishra, A. K. and Singh, V. P. (2010). A review of drought concepts. *Journal of Hydrology*, 391(1-2):202–216.

Mussá, F. E. F., Zhou, Y., Maskey, S., Masih, I., and Uhlenbrook, S. (2015). Groundwater as an emergency source for drought mitigation in the Crocodile River catchment, South Africa. *Hydrology and Earth System Sciences*, 19:1093–1106.

Mutowo, G. and Chikodzi, D. (2014). Remote sensing based drought monitoring in Zimbabwe. *Disaster Prevention and Management*, 23(5):549–659.

Narasimhan, B. and Srinivasan, R. (2005). Development and evaluation of Soil Moisture Deficit Index (SMDI) and Evapotranspiration Deficit Index (ETDI) for agricultural drought monitoring. *Agricultural and Forest Meteorology*, 133(1-4):69–88.

National Aeronautics and Space Administration (NASA) (2016a). MODIS. https://modis.gsfc.nasa.gov/about/index.php (Accessed: 27/07/16).

National Aeronautics and Space Administration (NASA) (2016b). MODIS Characterization Support Team, Calibration Section, Parameters. [data file] http://mcst.gsfc.nasa.gov/calibration/parameters (Retrieved: 26/07/16).

National Drought Mitigation Center (2016). What is Drought? http://drought.unl.edu/droughtbasics/whatisdrought.aspx (Accessed: 29/04/16).

National Oceanic and Atmospheric Administration (NOAA) (2014). National Weather Service: Weather Impacts of ENSO. http://www.srh.noaa.gov/jetstream/tropics/enso_impacts.html (Accessed: 29/12/16).

National Oceanic and Atmospheric Administration (NOAA) (2016a). Earth System Research Laboratory, Physical Science Devision: Multivariate ENSO Index (MEI). http://www.esrl.noaa.gov/psd/enso/mei/ (Accessed: 10/08/16).

National Oceanic and Atmospheric Administration (NOAA) (2016b). Earth System Research Laboratory, Physical Science Devision: Multivariate ENSO Index (MEI). [data file] http://www.esrl.noaa.gov/psd/enso/mei/table.html (Retrieved: 10/08/16).

National Oceanic and Atmospheric Administration (NOAA) (2016c). National Centers for Environmental Information: Equatorial Pacific Sea Surface Temperatures. https://www.ncdc.noaa.gov/teleconnections/enso/indicators/sst.php (Accessed: 10/10/16).

National Oceanic and Atmospheric Administration (NOAA) (2016d). National Centers for Environmental Information: Equatorial Pacific Sea Surface Temperatures. [data file] http://www.cpc.ncep.noaa.gov/data/indices/sstoi.indices (Retrieved: 10/08/16).

National Oceanic and Atmospheric Administration (NOAA) (2016e). National Centers for Environmental Information: Outgoing Longwave Radiation (OLR). https://www.ncdc.noaa.gov/teleconnections/enso/indicators/olr/ (Accessed: 15/08/16).

National Oceanic and Atmospheric Administration (NOAA) (2016f). National Centers for Environmental Information: Southern Oscillation Index (SOI). https://www.ncdc.noaa.gov/teleconnections/enso/indicators/soi/ (Accessed: 10/08/16).

National Oceanic and Atmospheric Administration (NOAA) (2016g). National Weather Service, Climate Prediction Center: Historical El Niño/ La Niña episodes (1950-present). [data file] http://www.cpc.noaa.gov/products/analysis_monitoring/ensostuff/ensoyears.shtml (Retrieved: 10/08/16).

Naumann, G., Barbosa, P., Carrao, H., Singleton, A., and Vogt, J. (2012). Monitoring drought conditions and their uncertainties in Africa using TRMM data. *Journal of Applied Meteorology and Climatology*, 51(10):1867–1874.

Naumann, G., Dutra, E., Barbosa, P., Pappenberger, F., Wetterhall, F., and Vogt, J. V. (2014). Comparison of drought indicators derived from multiple data sets over Africa. *Hydrology and Earth System Sciences*, 18(5):1625–1640.

Niang, I., Ruppel, M. A., Abdrabo, A., Essel, C., Lennard, J., Padgham, J., and Urquhart, P. (2014). Africa. In Barros, V., Field, C., Dokken, D. J., Mastrandrea, M., Mach, K.,

Bilir, T., Chatterjee, M., Ebi, K., Estrada, Y., Genova, R., Girma, B., Kissel, E., Levy, A., MacCracken, S., Mastrandrea, P., and White, L., editors, *Climate Change 2014: Impacts, Adaptation, and Vulnerability. Part B: Regional Aspects. Contribution of Working Group II to the Fifth Assessment Report of the Intergovernmental Panel on Climate Change*, pages 1199–1265. Cambridge University Press, Cambridge and New York.

Niemeyer, S. (2008). New drought indices. *Options Méditerranéennes*, 80:267–274.

Ntale, H. K. and Gan, T. Y. (2003). Drought indices and their application to East Africa. *International Journal of Climatology*, 23(11):1335–1357.

OCHA (2011). Eastern Africa - Drought Humanitarian Report No. 3. United Nations Office for the Coordination of Humanitarian Affairs.

Onono, P. A., Wawire, N. W. H., and Ombuki, C. (2013). The response of maize production in Kenya to economic incentives. *International Journal of Development and Sustainability*, 2(2).

Palmer, W. C. (1965). Meteorological Drought. Research Paper No. 45. Technical report, U.S. Weather Bureau, Washington, D.C.

Palmer, W. C. (1968). Keeping Track of Crop Moisture Conditions, Nationwide: The New Crop Moisture Index. *Weatherwise*, 21(4):156–161.

Peel, M. C., Finlayson, B. L., and McMahon, T. a. (2007). Updated world map of the Köppen-Geiger climate classification. *Meteorologische Zeitschrift*, 15:259–263.

Philippon, N., Martiny, N., Camberlin, P., Hoffman, M. T., and Gond, V. (2014). Timing and patterns of the ENSO signal in Africa over the last 30 years: Insights from Normalized Difference Vegetation Index Data. *Journal of Climate*, 27(7):2509–2532.

Plisnier, P. D., Serneels, S., and Lambin, E. F. (2000). Impact of ENSO on East African ecosystems: A multivariate analysis based on climate and remote sensing data. *Global Ecology and Biogeography*, 9(6):481–497.

Preethi, B., Sabin, T. P., Adedoyin, J. A., and Ashok, K. (2015). Impacts of the ENSO Modoki and other Tropical Indo-Pacific Climate-Drivers on African Rainfall. *Scientific Reports*, 5:16653.

Propastin, P., Fotso, L., and Kappas, M. (2010). Assessment of vegetation vulnerability to ENSO warm events over Africa. *International Journal of Applied Earth Observation and Geoinformation*, 12S:S83–S89.

R Core Team (2013). *R: A Language and Environment for Statistical Computing*. R Foundation for Statistical Computing, Vienna, Austria. https://www.R-project.org.

Ramankutty, N., Evan, A. T., Monfreda, C., and Foley, J. A. (2008). Farming the planet: 1. Geographic distribution of global agricultural lands in the year 2000. *Global Biogeichemical Cycles*, 22:GB1003.

Ratnam, J. V., Behera, K., Masumoto, Y., and Yamagata, T. (2014). Remote Effects of El Niño and Modoki Events on the Austral Summer Precipitation of Southern Africa. *Journal of Climate*, 27:3802–3815.

Richard, Y., Trzaska, S., Roucou, P., and Rouault, M. (2000). Modification of the southern African rainfall variability/ENSO relationship since the late 1960s. *Climate Dynamics*, 16:883–895.

Rojas, O., Li, Y., and Cumani, R. (2014). *Understanding the drought impact of El Niño on the global agricultural areas: An assessment using FAO's Agricultural Stress Index (ASI)*. FAO, Rome.

Rojas, O., Vrieling, A., and Rembold, F. (2011). Assessing drought probability for agricultural areas in Africa with coarse resolution remote sensing imagery. *Remote Sensing of Environment*, 115(2):343–352.

Ropelewski, C. F. and Halpert, M. S. (1987). Global and Regional Scale Precipitation Patterns Associated with the El Niño/Southern Oscillation. *Monthly Weather Review*, 115(8):1606–1626.

Ropelewski, C. F. and Halpert, M. S. (1989). Precipitation Patterns Associated with the High Index Phase of the Southern Oscillation. *Journal of Climate*, 2(3):268–284.

Ropelewski, C. F. and Halpert, M. S. (1996). Quantifying Southern Oscillation - Precipitation relationships. *Journal of Climate*, 9(5):1043–1059.

Rosenzweig, C. and Hillel, D. (2008). *Climate Variability and the Global Harvest: Impacts of El Niño and Other Oscillations on Agroecosystems*. Oxford University Press, New York.

Rouault, M. and Richard, Y. (2005). Intensity and spatial extent of droughts in southern Africa. *Geophysical Research Letters*, 32(15):2–5.

Rouse, J. W., Hass, R. H., Schell, J., and Deering, D. (1973). Monitoring vegetation systems in the great plains with ERTS. *Third Earth Resources Technology Satellite (ERTS) symposium*, 1:309–317.

Rulinda, C. M., Dilo, A., Bijker, W., and Stein, A. (2012). Characterising and quantifying vegetative drought in East Africa using fuzzy modelling and NDVI data. *Journal of Arid Environments*, 78:169–178.

Rulinda, C. M., Stein, A., and Turdukulov, U. D. (2013). Visualizing and quantifying the movement of vegetative drought using remote-sensing data and gis. *International Journal of Geographical Information Science*, 27(8):1481–1496.

Sánchez, N., González-Zamora, Á., Piles, M., and Martínez-Fernández, J. (2016). A New Soil Moisture Agricultural Drought Index (SMADI) Integrating MODIS and SMOS Products: A Case of Study over the Iberian Peninsula. *Remote Sensing*, 8(4):287.

Sannier, C. a. D., Taylor, J. C., Du Plessis, W., and Campbell, K. (1998). Real-time vegetation monitoring with NOAA-AVHRR in Southern Africa for wildlife management and food security assessment. *International Journal of Remote Sensing*, 19(4):621–639.

Santoso, A., Mcgregor, S., Jin, F.-f., Cai, W., England, M. H., An, S.-i., Mcphaden, M. J., and Guilyardi, E. (2013). Late-twentieth-century emergence of the El Niño propagation asymmetry and future projections. *Nature*, 504:126–130.

Sarachnik, E. S. and Cane, M. a. (2010). *The El Niño-Southern Oscillation phenomenon*. Cambridge University Press, Cambridge.

Savitzky, A. and Golay, M. J. E. (1964). Smoothing and Differentiation of Data by Simplified Least Squares Procedures. *Analytical Chemistry*, 36(8):1627–1639.

Schneider, S. H., Root, T. L., and Mastrandrea, M. D., editors (2011). *Encyclopedia of Climate and Weather*. Oxford University Press, Oxford, 2nd edition.

Schubert, S. D., Stewart, R. E., Wang, H., Barlow, M., Berbery, E. H., Cai, W., Hoerling, M. P., Kanikicharla, K. K., Koster, R. D., Lyon, B., Mariotti, A., Mechoso, C. R., Müller, O. V., Rodriguez-Fonseca, B., Seager, R., Senevirante, S. I., Zhang, L., and Zhou, T. (2016). Global meteorological drought: A synthesis of current understanding with a focus on sst drivers of precipitation deficits. *Journal of Climate*, 29(11):3989–4019.

See, L., Fritz, S., You, L., Ramankutty, N., Herrero, M., Justice, C., Becker-Reshef, I., Thornton, P., Erb, K., Gong, P., Tang, H., Velde, M. V. D., Ericksen, P., Mccallum, I., Kraxner, F., and Obersteiner, M. (2015). Improved global cropland data as an essential ingredient for food security. *Global Food Security*, 4:37–45.

Senay, G. B., Velpuri, N. M., Bohms, S., Budde, M., Young, C., Rowland, J., and Verdin, J. P. (2015). Drought Monitoring and Assessment : Remote Sensing and Modeling Approaches for the Famine Early Warning Systems Network. *Hydro-Meteorological Hazards, Risks and Disasters*, pages 233–262.

Seneviratne, S., Nicholls, N., Easterling, D., Goodess, C., Kanae, S., Kossin, J., Luo, Y., Marengo, J., McInnes, K., Rahimi, M., Reichstein, M., Sorteberg, A., Vera, C., and Zhang, X. (2012). Changes in climate extremes and their impacts on the natural physical environment. In *Managing the Risk of Extreme Events and Disasters to Advance Climate Change Adaptation. A Special Report of Working Groups I and II of the Intergovernmental Panel on Climate Change (IPCC)*, pages 109–230. Cambridge University Press, Cambridge.

Sepulcre-Canto, G., Horion, S., Singleton, A., Carrao, H., and Vogt, J. (2012). Development of a Combined Drought Indicator to detect agricultural drought in Europe. *Natural Hazards and Earth System Science*, 12(11):3519–3531.

Shafer, B. A. and Dezman, L. E. (1982). Development of a surface water supply index (SWSI) to assess the severity of drought conditions in snowpack runoff areas. In *Proceedings of the Western Snow Conference*, pages 164–175, Fort Collins.

Sheffield, J., Wood, E. F., Chaney, N., Guan, K., Sadri, S., Yuan, X., Olang, L., Amani, A., Ali, A., Demuth, S., and Ogallo, L. (2014). A drought monitoring and forecasting system for sub-sahara african water resources and food security. *Bulletin of the American Meteorological Society*, 95(6):861–882.

Smakhtin, V. U. and Schipper, E. L. F. (2008). Droughts: The impact of semantics and perceptions. *Water Policy*, 10(2):131–143.

Stahl, K. (2001). Hydrological Ddrought - a study across Europe. PhD thesis. *Freiburger Schriften zur Hydrologie*, 15.

STAR – Center for Satellite Applications and Research (2008). NOAA AVHRR Spectral Response Functions. [data file] http://www.star.nesdis.noaa.gov/smcd/spb/fwu/homepage/AVHRR/spec_resp_func/index.html (Retrieved: 26/07/16).

Steinemann, A. C., Hayes, M. J., and Cavalcanti, L. F. (2005). Drought Indicators and Triggers. In Wilhite, D. A., editor, *Drought and Water Crises: Science, Technology, and Management Issues*, chapter 4, pages 71–92. Taylor & Francis, Boca Raton.

Stige, L. C., Stave, J., Chan, K.-S., Ciannelli, L., Pettorelli, N., Glantz, M., Herren, H. R., and Stenseth, N. C. (2006). The effect of climate variation on agro-pastoral production in Africa. *Proceedings of the National Academy of Sciences of the United States of America*, 103(9):3049–3053.

Strahler, A. (2011). *Introducing Physical Geography*. John Wiley & Sons, Hoboken, 5 edition.

Svoboda, M., LeComte, D., Hayes, M., Heim, R., Gleason, K., Angel, J., Rippey, B., Tinker, R., Palecki, M., Stooksbury, D., Miskus, D., and Stephens, S. (2002). The drought monitor. *Bulletin of the American Meteorological Society*, 83(8):1181–1190.

Taffesse, A. S., Dorosh, P., and Sinafikeh, A. (2013). Crop production in Ethiopia: regional patterns and trends. In Dorosh, P. A. and Rashid, S., editors, *Food and agriculture in Ethiopia: Progress and policy challenges*, chapter 3, pages 53–83. International Food Policy Research Institute (IFPRI), Washington, DC.

Townshend, J. R. G. and Justice, C. O. (2002). Towards operational monitoring of terrestrial systems by moderate-resolution remote sensing. *Remote Sensing of Environment*, 83:351–359.

Tropical Rainfall Measuring Mission (TRMM) (2011). TRMM (TMPA/3B43) Rainfall Estimate L3 1 month 0.25 degree x 0.25 degree V7, Greenbelt, MD, Goddard Earth Sciences Data and Information Services Center (GES DISC). [data files] http://disc.gsfc.nasa.gov/datacollection/TRMM_3B43_7.html (Retrieved: 06/08/16).

Tsakiris, G. and Vangelis, H. (2005). Establishing a drought index incorporating evapotranspiration. *European Water*, 9(10):3–11.

Tucker, C. J. (1979). Red and photographic infrared linear combinations for monitoring vegetation. *Remote Sensing of Environment*, 8(2):127–150.

Tucker, C. J. and Choudhury, B. J. (1987). Satellite remote sensing of drought conditions. *Remote Sensing of Environment*, 23(2):243–251.

UNCCD (1994). United Nations Convention to Combat Desertification in countries experiencing serious drought and/or desertification, particularly in Africa. Technical report, United Nations (UN).

UNEP (2008). *Africa: Atlas of Our Changing Environment.* United Nations Environment Programme, Nairobi.

Unganai, L. S. and Kogan, F. N. (1998). Drought Monitoring and Corn Yield Estimation in Southern Africa from AVHRR Data. *Remote Sensing of Environment*, 63:219–232.

Van Loon, A. F. (2015). Hydrological drought explained. *Wiley Interdisciplinary Reviews: Water*, 2(4):359–392.

Van Rooy, M. P. (1965). A rainfall anomaly index independent of time and space. *Notos*, 14:43–48.

Vecchi, G. A. and Wittenberg, A. T. (2010). El Niño and our future climate: Where do we stand? *Wiley Interdisciplinary Reviews: Climate Change*, 1(2):260–270.

Vermote, E. (2015). MOD09A1 MODIS/Terra Surface Reflectance 8-Day L3 Global 500m SIN Grid V006. NASA EOSDIS Land Processes DAAC. https://lpdaac.usgs.gov/node/804 (Accessed: 06/08/16).

Vicente-Serrano, S. M., Beguería, S., and López-Moreno, J. I. (2010). A multiscalar drought index sensitive to global warming: The standardized precipitation evapotranspiration index. *Journal of Climate*, 23(7):1696–1718.

Vicente-Serrano, S. M., Beguería, S., Lorenzo-Lacruz, J., Camarero, J. J., López-Moreno, J. I., Azorin-Molina, C., Revuelto, J., Morán-Tejeda, E., and Sanchez-Lorenzo, A. (2012). Performance of drought indices for ecological, agricultural, and hydrological applications. *Earth Interactions*, 16(10).

Vicente-Serrano, S. M., Cabello, D., Tomás-Burguera, M., Martín-Hernández, N., Beguería, S., Azorin-Molina, C., and Kenawy, A. E. (2015). Drought variability and land degradation in semiarid regions: Assessment using remote sensing data and drought indices (1982-2011). *Remote Sensing*, 7(4):4391–4423.

Viste, E., Korecha, D., and Sorteberg, A. (2013). Recent drought and precipitation tendencies in Ethiopia. *Theoretical and Applied Climatology*, 112(3-4):535–551.

Wanders, N., van Lanen, H. A., and van Loon, A. F. (2010). Indicators for Drought Characterization on a Global Scale. Technical Report 24, WATCH.

Wilhite, D. A. (2000). Drought as a natural hazard: Concepts and definitions. In Wilhite, D. A., editor, *Drought: A Global Assessment*, pages 3–18. Routledge, London.

Wilhite, D. A. and Buchanan-Smith, M. (2005). Drought as Hazard: Understanding the Natural and Social Context. In Wilhite, D. A., editor, *Drought and Water Crises: Science, Technology, and Management Issues*, chapter 1, pages 3–29. Taylor & Francis, Boca Raton.

Wilhite, D. A., Svoboda, M. D., and Hayes, M. J. (2007). Understanding the complex impacts of drought: A key to enhancing drought mitigation and preparedness. *Water Resources Management*, 21(5):763–774.

World Meteorologic Organization (WMO) (2012). Standardized Precipitation Index User Guide. (M. Svoboda, M. Hayes and D. Wood). (WMO-No. 1090), Geneva.

Wu, D., Qu, J. J., and Hao, X. (2015). Agricultural drought monitoring using MODIS-based drought indices over the USA Corn Belt. *International Journal of Remote Sensing*, 36(21):5403–5425.

Yang, X. and DelSole, T. (2012). Systematic comparison of enso teleconnection patterns between models and observations. *Journal of Climate*, 25(2):425–446.

Zargar, A., Sadiq, R., Naser, B., and Khan, F. I. (2011). A review of drought indices. *Environmental Reviews*, 19:333–349.

# Appendix
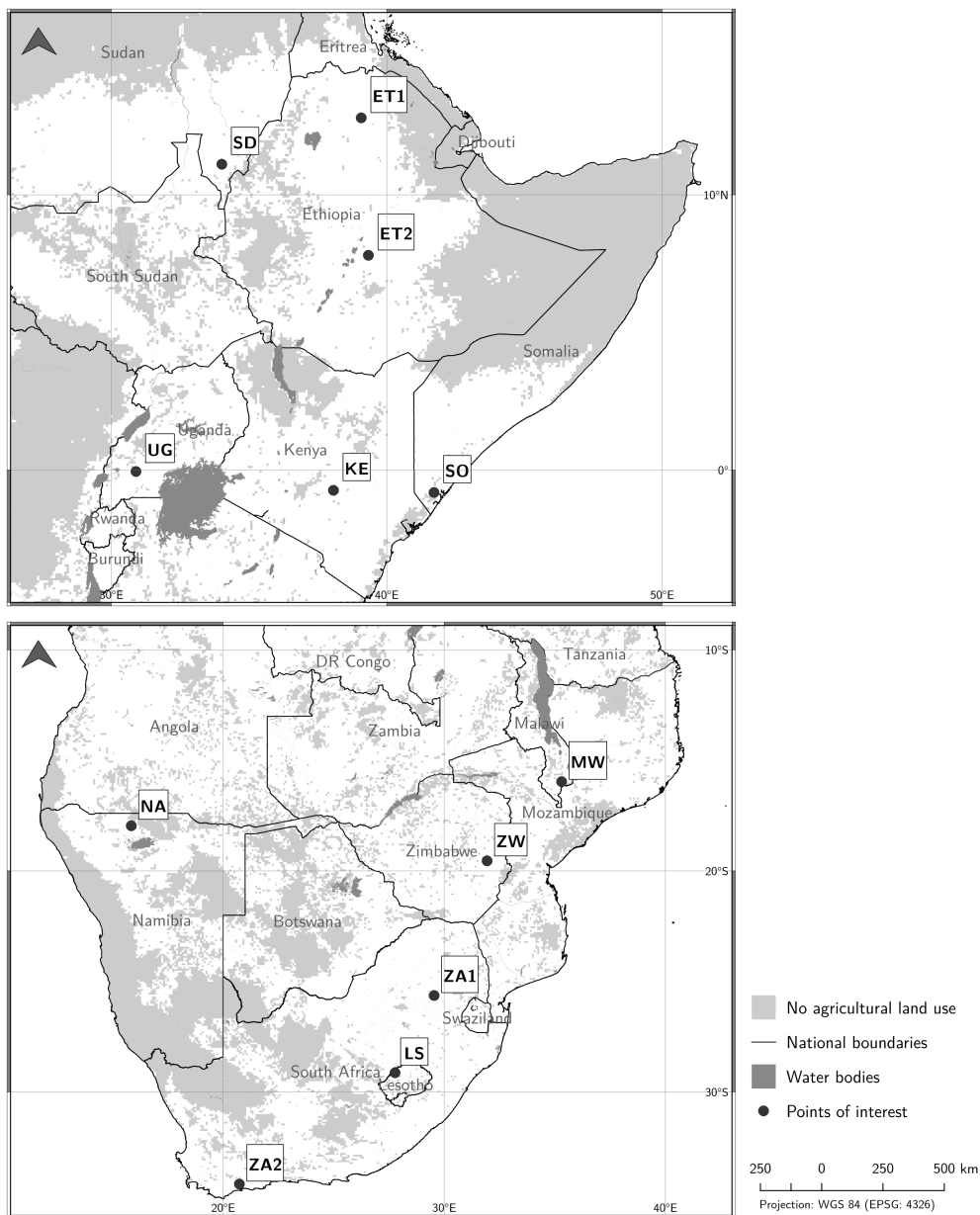


**Figure 1:** Location of selected points in focal regions for analysing SPI dynamics (see Figure 2)

**Table 1:** Overview of used IDL, Python and R scripts

| Code | File name | Short description |
| --- | --- | --- |
| CC-01 | cellstats_mmean_fromVRT.py | Arcpy script to calculate monthly means from 8-daily composites in VRT format, output in tiff (requires Python 2.7 with ArcGIS) |
| CC-02 | cropmask_to_MODIS_res_extent.pro | Extracts values from coarse cropland images and writes it to a given 500m-MODIS container – Fitting of crop mask to MODIS resolution (needed for CC-2) |
| CC-1 | correl_spi_enso.pro | Runs cross-correlation between SPI and ENSO index with significance test for different time lags – output: correlation values and significance masks for each time lag |
| CC-2 | correl_vci_enso.pro | Runs cross-correlation between VCI and ENSO index with significance test for different time lags – considers agricultural areas: exclusion of non-crop-pixels using a binary crop mask image - correlation values and significance masks for each time lag |
| CC-3 | find_lag_with_corr_max.py | Loads correlation images and binary significance masks for different time lags, stacks images, retrieves maximum correlation value and corresponding lag (Python 3.5) |
| DD-0 | seas_masks_from_SOS-EOS.pro | Creates monthly and 8-daily composite (DOY) growing season masks from Start-of-Season and End-of-Season images, (TIMESAT time steps) |
| DD-1 | droughtstats_from_SPI_per_gs.pro | SPI-based drought detection: Mean SPI and relative drought duration (threshold-based) per growing season |
| DD-2 | droughtstats_from_VCI_per_gs.pro | VCI-based drought detection: Mean VCI and relative drought duration (threshold-based) per growing season |
| PH-1 | calculate_NDVI_Median_ts.pro | Calculates multi-year median per DOY (composite) from NDVI time series (Input for TIMESAT processing) |
| PR-1 | reproject_rasters.py | Reproject raster files in tiff format to specified (e.g. MODIS) projection |
| PR-2 | TRMM_to_MOD_res_extent.pro | Extracts values from coarse TRMM images, writes it to a given 500m-MODIS container – fitting of TRMM data to MODIS resolution |
| SPI-0 | nc_to_tif.R | Converts TRMM rainfall images from netCDF to GeoTIFF format |
| SPI-1 | trmm_calculate_SPI.R | Calculates SPI for specified level of monthly aggregation – based on rainfall images |
| TR-1 | Find_lag_ts_MEI-SPI.py | Calculates temporal offset between ENSO peak and minimum drought index time series - for SPI (Python 3.5) |
| TR-2 | Find_lag_ts_MEI-VCI.py | Calculates temporal offset between ENSO peak and minimum drought index time series - for VCI, loop through folders with tile numbers (Python 3.5) |
| VCI-0 | mod09a1_calculate_NDVI_VCI.pro | Loads time series of MOD09A1 raw data - calculates NDVI from band 1 and 2 - calculates VCI from NDVI time series – output: NDVI and VCI images |
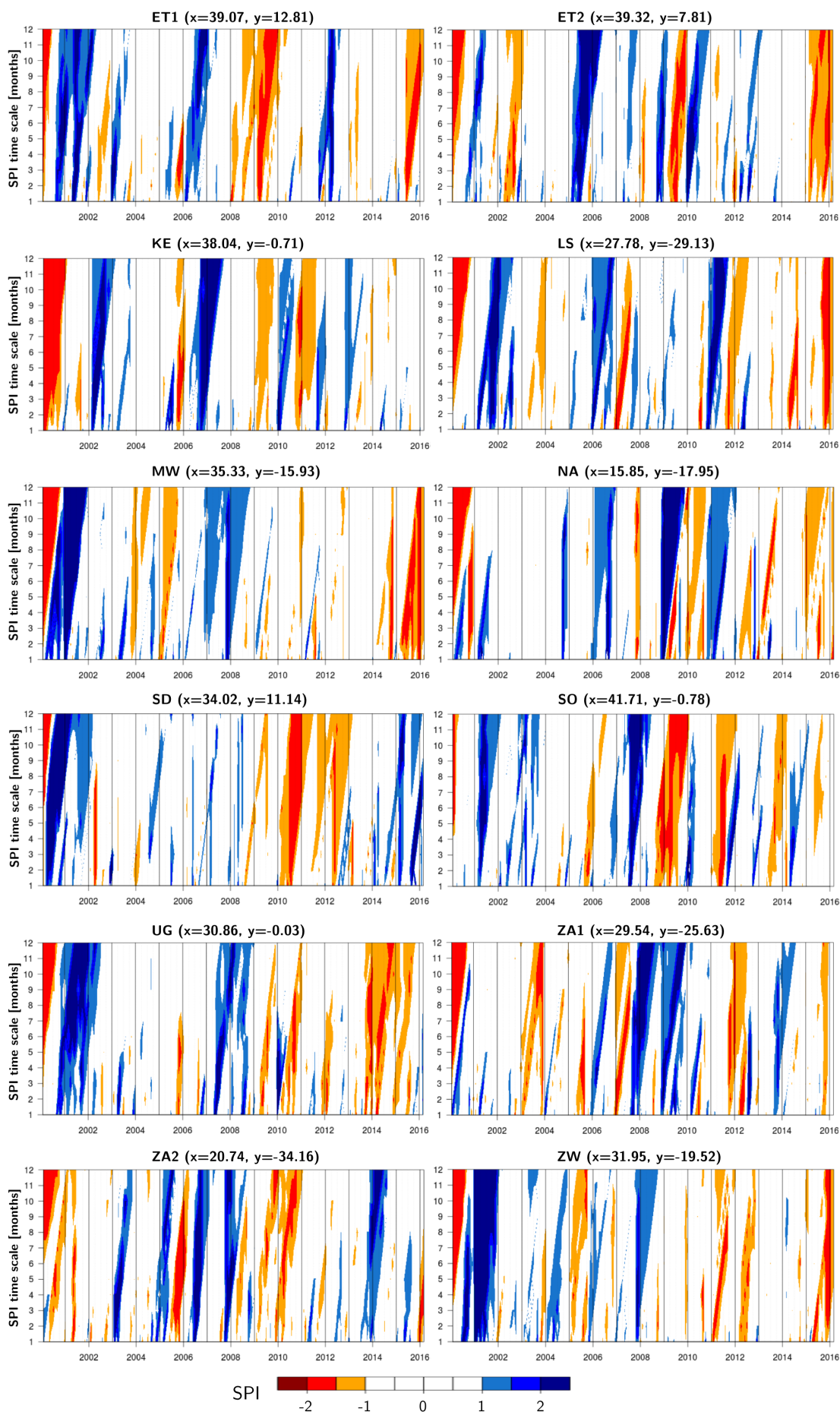
**Figure 2:** SPI dynamics for selected points (see Figure 1) during 2000-2016: Orange to red colours represent drought conditions. Transitions from meteorological (SPI scale of 1-2 months) to agricultural (3-6 months) and hydrological drought (6-12 months) are visualized.

**Table 2:** National statistics of crop production (in tonnes) from 2000 to 2013 (FAO, 2016b)

BOTSWANA

| Crop types | 2000 | 2001 | 2002 | 2003 | 2004 | 2005 | 2006 | 2007 | 2008 | 2009 | 2010 | 2011 | 2012 | 2013 |
|---|---|---|---|---|---|---|---|---|---|---|---|---|---|---|
| Cereals | 24,776 | 23,080 | 34,674 | 35,930 | 26,668 | 36,841 | 43,532 | 31,312 | 36,782 | 54,430 | 50,345 | 74,024 | 37,457 | 19,366 |
| Fibre crops | 900 | 1,191 | 770 | 693 | 732 | 783 | 664 | 499 | 590 | 450 | 400 | 300 | 300 | 300 |
| Fruit | 10,600 | 10,659 | 11,316 | 12,200 | 11,850 | 11,795 | 12,130 | 7,980 | 7,850 | 6,000 | 5,920 | 6,600 | 7,100 | 7,126 |
| Oilcrops | 2,518 | 3,040 | 3,003 | 3,249 | 3,086 | 3,269 | 2,808 | 1,327 | 3,917 | 1,313 | 2,702 | 6,837 | 2,614 | 958 |
| Pulses | 17,500 | 19,800 | 21,000 | 24,000 | 25,000 | 15,000 | 7,000 | 805 | 2,305 | 4,313 | 3,873 | 4,700 | 2,285 | 3,655 |
| Roots & tubers | 85,000 | 92,000 | 93,000 | 84,613 | 101,484 | 99,714 | 93,500 | 94,000 | 90,000 | 83,175 | 92,934 | 97,037 | 99,000 | 99,500 |
| Treenuts | - | - | - | - | - | - | - | - | - | - | - | - | - | - |
| Vegetables | 16,950 | 17,873 | 17,291 | 16,898 | 16,708 | 16,637 | 23,448 | 30,501 | 31,704 | 25,821 | 39,834 | 40,164 | 40,680 | 40,316 |

ETHIOPIA

| Crop types | 2000 | 2001 | 2002 | 2003 | 2004 | 2005 | 2006 | 2007 | 2008 | 2009 | 2010 | 2011 | 2012 | 2013 |
|---|---|---|---|---|---|---|---|---|---|---|---|---|---|---|
| Cereals | 8,019,830 | 9,585,753 | 9,000,335 | 9,532,780 | 10,140,082 | 12,749,986 | 12,672,350 | 12,235,743 | 13,259,750 | 15,534,229 | 17,761,202 | 18,809,963 | 19,651,152 | 21,575,457 |
| Fibre crops | 34,450 | 32,153 | 41,243 | 41,072 | 41,954 | 43,563 | 68,215 | 62,778 | 56,064 | 47,987 | 36,763 | 41,615 | 44,215 | 52,215 |
| Fruit | 382,902 | 351,328 | 405,470 | 429,204 | 460,943 | 648,638 | 697,125 | 740,538 | 554,781 | 642,747 | 680,543 | 729,234 | 672,293 | 671,638 |
| Oilcrops | 66,544 | 84,918 | 79,941 | 105,281 | 118,117 | 193,119 | 183,719 | 188,033 | 234,142 | 247,490 | 251,924 | 280,115 | 279,752 | 271,165 |
| Pulses | 996,051 | 1,159,794 | 1,085,221 | 982,990 | 1,248,465 | 1,340,884 | 1,373,951 | 1,572,816 | 1,774,338 | 1,890,842 | 1,965,761 | 2,268,383 | 2,690,165 | 2,784,100 |
| Roots & tubers | 4,713,277 | 4,978,778 | 5,073,421 | 5,524,423 | 5,664,210 | 5,721,405 | 5,943,760 | 6,290,408 | 5,656,357 | 6,011,286 | 6,223,422 | 6,275,069 | 8,366,131 | 8,961,256 |
| Treenuts | 70,000 | 75,000 | 72,000 | 74,000 | 69,057 | 76,000 | 54,842 | 65,314 | 72,004 | 55,968 | 53,051 | 63,194 | 64,500 | 64,500 |
| Vegetables | 846,818 | 869,602 | 968,162 | 1,009,846 | 1,210,771 | 1,334,739 | 1,213,954 | 1,090,966 | 1,390,755 | 1,669,699 | 1,802,667 | 1,787,208 | 1,929,685 | 1,889,500 |

ERITREA

| Crop types | 2000 | 2001 | 2002 | 2003 | 2004 | 2005 | 2006 | 2007 | 2008 | 2009 | 2010 | 2011 | 2012 | 2013 |
|---|---|---|---|---|---|---|---|---|---|---|---|---|---|---|
| Cereals | 124,549 | 219,052 | 54,530 | 105,944 | 108,798 | 335,563 | 377,202 | 461,996 | 105,788 | 226,899 | 243,594 | 258,135 | 275,000 | 265,000 |
| Fibre crops | - | - | - | - | - | - | - | - | - | - | - | - | - | - |
| Fruit | 3,800 | 4,000 | 4,500 | 4,757 | 5,059 | 4,770 | 5,000 | 4,953 | 4,946 | 5,323 | 5,389 | 5,296 | 5,000 | 5,000 |
| Oilcrops | 5,129 | 6,850 | 4,709 | 8,490 | 6,008 | 12,170 | 6,628 | 10,502 | 4,666 | 5,107 | 4,455 | 4,175 | 4,554 | 4,657 |
| Pulses | 34,172 | 46,005 | 41,172 | 34,763 | 38,752 | 40,423 | 34,992 | 30,362 | 23,896 | 37,654 | 37,786 | 41,559 | 42,505 | 42,590 |
| Roots & tubers | 131,431 | 107,415 | 94,246 | 105,850 | 112,196 | 90,867 | 114,674 | 73,169 | 76,798 | 79,546 | 65,150 | 64,075 | 62,150 | 63,150 |
| Treenuts | - | - | - | - | - | - | - | - | - | - | - | - | - | - |
| Vegetables | 27,000 | 27,191 | 25,000 | 29,700 | 27,000 | 30,000 | 37,576 | 41,545 | 40,051 | 47,833 | 55,774 | 52,491 | 55,000 | 48,552 |

KENYA

| Crop types | 2000 | 2001 | 2002 | 2003 | 2004 | 2005 | 2006 | 2007 | 2008 | 2009 | 2010 | 2011 | 2012 | 2013 |
|---|---|---|---|---|---|---|---|---|---|---|---|---|---|---|
| Cereals | 2,591,351 | 3,370,458 | 3,045,518 | 3,351,497 | 3,199,022 | 3,585,080 | 3,937,106 | 3,614,399 | 2,866,388 | 2,898,900 | 4,347,437 | 4,058,581 | 4,711,585 | 4,536,942 |
| Fibre crops | 23,237 | 25,175 | 30,044 | 31,091 | 31,646 | 32,449 | 33,817 | 33,071 | 27,101 | 23,978 | 27,862 | 34,804 | 31,711 | 32,200 |
| Fruit | 2,179,528 | 2,357,350 | 2,326,383 | 2,044,302 | 2,280,182 | 2,474,509 | 2,451,047 | 2,540,497 | 3,107,383 | 3,147,769 | 3,174,964 | 2,549,110 | 2,773,388 | 2,857,395 |
| Oilcrops | 40,409 | 46,396 | 36,528 | 36,812 | 41,056 | 40,335 | 41,706 | 45,266 | 42,179 | 40,782 | 36,731 | 41,512 | 48,282 | 62,132 |
| Pulses | 478,308 | 482,126 | 671,477 | 607,503 | 440,277 | 530,415 | 746,609 | 625,782 | 416,568 | 592,527 | 593,933 | 773,863 | 935,880 | 1,046,534 |
| Roots & tubers | 1,642,847 | 2,338,545 | 1,995,532 | 2,264,167 | 2,327,674 | 3,683,690 | 3,827,206 | 3,424,471 | 4,573,668 | 4,176,330 | 3,896,594 | 3,831,494 | 4,734,181 | 3,889,688 |
| Treenuts | 24,147 | 24,224 | 23,868 | 23,144 | 24,332 | 24,424 | 24,349 | 29,002 | 36,000 | 37,683 | 37,438 | 44,596 | 53,026 | 54,200 |
| Vegetables | 1,557,563 | 1,675,351 | 1,634,299 | 1,841,360 | 1,508,727 | 1,947,891 | 1,956,475 | 2,178,985 | 1,839,275 | 1,971,548 | 2,527,284 | 1,961,057 | 2,105,983 | 2,389,880 |

MALAWI

| Crop types | 2000 | 2001 | 2002 | 2003 | 2004 | 2005 | 2006 | 2007 | 2008 | 2009 | 2010 | 2011 | 2012 | 2013 |
|---|---|---|---|---|---|---|---|---|---|---|---|---|---|---|
| Cereals | 2,631,034 | 1,865,675 | 1,710,577 | 2,143,179 | 1,717,993 | 1,302,379 | 2,786,281 | 3,440,138 | 2,845,840 | 3,807,971 | 3,610,283 | 3,924,971 | 3,832,659 | 3,892,310 |
| Fibre crops | 9,790 | 9,999 | 10,107 | 10,306 | 14,762 | 14,124 | 16,128 | 18,132 | 20,633 | 19,101 | 8,019 | 14,137 | 65,137 | 42,538 |
| Fruit | 755,498 | 763,835 | 822,279 | 878,539 | 936,099 | 941,724 | 985,563 | 1,004,507 | 1,027,749 | 1,062,614 | 1,061,419 | 1,053,662 | 1,089,243 | 1,115,867 |
| Oilcrops | 42,041 | 52,350 | 53,699 | 70,699 | 62,241 | 56,235 | 79,774 | 100,778 | 95,168 | 109,500 | 109,839 | 121,667 | 160,629 | 156,554 |
| Pulses | 250,485 | 332,170 | 316,906 | 360,486 | 284,915 | 251,225 | 364,128 | 408,085 | 387,139 | 442,287 | 444,393 | 542,879 | 563,618 | 621,613 |
| Roots & tubers | 4,832,199 | 6,214,736 | 2,944,299 | 3,619,559 | 4,715,032 | 3,683,860 | 5,141,920 | 6,098,087 | 6,485,354 | 7,251,499 | 7,674,874 | 7,872,928 | 8,844,743 | 9,349,991 |
| Treenuts | 1,900 | 2,100 | 2,300 | 2,500 | 2,700 | 2,800 | 2,850 | 3,394 | 3,742 | 2,909 | 2,757 | 3,284 | 3,284 | 3,294 |
| Vegetables | 275,150 | 285,227 | 297,272 | 312,963 | 321,472 | 329,254 | 336,697 | 342,860 | 264,700 | 311,662 | 364,479 | 378,780 | 388,200 | 396,620 |

MOZAMBIQUE

| Crop types | 2000 | 2001 | 2002 | 2003 | 2004 | 2005 | 2006 | 2007 | 2008 | 2009 | 2010 | 2011 | 2012 | 2013 |
|---|---|---|---|---|---|---|---|---|---|---|---|---|---|---|
| Cereals | 1,587,548 | 1,507,208 | 1,361,336 | 1,512,504 | 1,327,853 | 1,143,200 | 1,751,507 | 1,889,656 | 2,216,414 | 2,239,000 | 2,802,582 | 1,587,548 | 1,507,208 | 1,361,336 |
| Fibre crops | 15,501 | 39,541 | 45,000 | 31,090 | 50,118 | 42,455 | 57,107 | 58,900 | 66,050 | 66,500 | 23,360 | 15,501 | 39,541 | 45,000 |
| Fruit | 290,768 | 311,428 | 337,299 | 347,500 | 359,238 | 390,486 | 446,409 | 485,404 | 529,444 | 582,982 | 647,344 | 290,768 | 311,428 | 337,299 |
| Oilcrops | 123,868 | 129,943 | 112,670 | 106,769 | 117,182 | 140,071 | 124,341 | 139,259 | 139,345 | 142,591 | 157,517 | 123,868 | 129,943 | 112,670 |
| Pulses | 100,000 | 105,000 | 255,500 | 278,600 | 302,000 | 289,500 | 390,400 | 418,500 | 381,100 | 380,000 | 415,000 | 100,000 | 105,000 | 255,500 |
| Roots & tubers | 5,877,974 | 6,520,416 | 6,475,524 | 7,131,717 | 7,421,895 | 5,386,816 | 6,257,338 | 5,928,990 | 5,084,546 | 6,723,500 | 10,845,192 | 5,877,974 | 6,520,416 | 6,475,524 |
| Treenuts | 57,894 | 58,000 | 50,177 | 63,818 | 42,988 | 104,337 | 62,821 | 74,395 | 85,000 | 64,000 | 96,558 | 57,894 | 58,000 | 50,177 |
| Vegetables | 115,282 | 131,310 | 146,529 | 192,628 | 225,354 | 250,598 | 310,749 | 343,328 | 373,798 | 405,729 | 449,650 | 115,282 | 131,310 | 146,529 |

NAMIBIA

| Crop types | 2000 | 2001 | 2002 | 2003 | 2004 | 2005 | 2006 | 2007 | 2008 | 2009 | 2010 | 2011 | 2012 | 2013 |
|---|---|---|---|---|---|---|---|---|---|---|---|---|---|---|
| Cereals | 120,979 | 106,919 | 99,949 | 97,380 | 127,535 | 129,138 | 182,684 | 116,183 | 112,580 | 111,738 | 136,500 | 117,000 | 165,800 | 87,000 |
| Fibre crops | 1,947 | 1,265 | 559 | 509 | 3,123 | 33 | 78 | 2 | - | - | - | - | - | - |
| Fruit | 16,413 | 19,718 | 24,871 | 26,543 | 30,879 | 35,607 | 42,140 | 42,416 | 39,834 | 33,342 | 42,225 | 43,772 | 45,872 | 46,922 |
| Oilcrops | 716 | 577 | 284 | 302 | 1,115 | 59 | 86 | 163 | 172 | 194 | 189 | 153 | 172 | 159 |
| Pulses | 13,010 | 15,146 | 9,287 | 15,040 | 16,060 | 15,718 | 17,100 | 17,626 | 18,063 | 21,088 | 19,130 | 18,947 | 19,620 | 18,610 |
| Roots & tubers | 256,000 | 272,000 | 288,000 | 299,000 | 309,202 | 320,201 | 323,769 | 338,822 | 341,233 | 327,136 | 342,500 | 357,569 | 351,500 | 363,000 |
| Treenuts | - | - | - | - | - | - | - | - | - | - | - | - | - | - |
| Vegetables | 23,214 | 26,332 | 29,272 | 32,065 | 32,108 | 35,644 | 43,029 | 54,172 | 56,158 | 55,734 | 60,000 | 59,927 | 63,655 | 66,614 |

SOMALIA

| Crop types | 2000 | 2001 | 2002 | 2003 | 2004 | 2005 | 2006 | 2007 | 2008 | 2009 | 2010 | 2011 | 2012 | 2013 |
|---|---|---|---|---|---|---|---|---|---|---|---|---|---|---|
| Cereals | 392,408 | 429,062 | 441,871 | 402,751 | 366,470 | 361,182 | 266,815 | 196,970 | 192,634 | 229,641 | 356,007 | 118,913 | 385,345 | 383,243 |
| Fibre crops | 1,697 | 1,680 | 1,764 | 1,764 | 1,792 | 1,848 | 1,848 | 1,848 | 1,848 | 1,904 | 1,904 | 1,904 | 1,960 | 1,960 |
| Fruit | 194,100 | 194,383 | 200,073 | 202,090 | 208,350 | 199,989 | 216,766 | 216,031 | 212,938 | 226,810 | 229,975 | 223,317 | 218,800 | 218,800 |
| Oilcrops | 12,507 | 14,894 | 15,637 | 16,373 | 21,874 | 26,906 | 25,619 | 25,324 | 27,052 | 31,257 | 32,148 | 32,200 | 38,802 | 43,127 |
| Pulses | 15,000 | 16,500 | 14,995 | 17,500 | 18,500 | 20,301 | 18,000 | 18,482 | 16,565 | 20,972 | 21,301 | 25,778 | 27,000 | 25,000 |
| Roots & tubers | 75,500 | 81,500 | 87,133 | 82,286 | 93,762 | 101,479 | 89,000 | 80,371 | 86,181 | 91,200 | 87,974 | 95,331 | 98,000 | 98,000 |
| Treenuts | - | - | - | - | - | - | - | - | - | - | - | - | - | - |
| Vegetables | 76,583 | 79,545 | 103,951 | 88,740 | 89,100 | 92,937 | 83,000 | 91,846 | 86,866 | 98,428 | 114,422 | 110,466 | 112,500 | 113,891 |

SOUTH AFRICA

| Crop types | 2000 | 2001 | 2002 | 2003 | 2004 | 2005 | 2006 | 2007 | 2008 | 2009 | 2010 | 2011 | 2012 | 2013 |
|---|---|---|---|---|---|---|---|---|---|---|---|---|---|---|
| Cereals | 14,527,340 | 10,702,651 | 13,044,712 | 11,816,396 | 12,024,567 | 14,178,936 | 9,443,591 | 9,506,948 | 15,338,396 | 14,576,685 | 14,699,306 | 12,918,562 | 14,266,240 | 14,872,900 |
| Fibre crops | 33,253 | 42,046 | 23,181 | 21,031 | 32,636 | 22,046 | 18,813 | 14,176 | 13,406 | 11,873 | 11,717 | 22,628 | 17,610 | 11,760 |
| Fruit | 5,111,405 | 5,111,422 | 5,444,040 | 5,863,420 | 5,740,129 | 5,719,016 | 5,868,886 | 6,022,571 | 6,321,493 | 6,012,953 | 5,947,691 | 6,131,595 | 6,299,879 | 6,420,778 |
| Oilcrops | 312,710 | 406,213 | 502,269 | 348,559 | 364,610 | 348,835 | 334,609 | 200,066 | 454,849 | 474,800 | 351,530 | 532,833 | 432,802 | 434,101 |
| Pulses | 108,160 | 129,950 | 80,197 | 78,498 | 90,862 | 91,073 | 88,419 | 57,226 | 83,078 | 94,487 | 73,655 | 63,430 | 71,595 | 72,400 |
| Roots & tubers | 1,773,053 | 1,849,210 | 1,699,377 | 1,546,129 | 1,854,420 | 1,822,070 | 1,909,850 | 2,022,989 | 2,092,496 | 1,929,602 | 2,155,994 | 2,251,175 | 2,306,073 | 2,308,000 |
| Treenuts | 9,500 | 10,000 | 11,500 | 12,000 | 13,000 | 13,500 | 14,000 | 14,500 | 15,985 | 15,994 | 16,500 | 18,000 | 18,000 | 18,875 |
| Vegetables | 2,108,321 | 2,216,590 | 2,156,648 | 2,279,217 | 2,243,930 | 2,236,980 | 2,006,180 | 2,162,632 | 2,453,977 | 2,363,353 | 2,619,790 | 2,607,461 | 2,746,823 | 2,764,661 |

(Former) Sudan & South Sudan

| Crop types | 2000 | 2001 | 2002 | 2003 | 2004 | 2005 | 2006 | 2007 | 2008 | 2009 | 2010 | 2011 | 2012 | 2013 |
|---|---|---|---|---|---|---|---|---|---|---|---|---|---|---|
| Cereals | 3,259,000 | 5,339,000 | 3,714,000 | 6,372,748 | 3,516,000 | 6,193,000 | 5,806,000 | 6,691,000 | 5,269,000 | 5,552,195 | 3,562,350 | 5,598,000 | 3,026,000 | 5,947,000 |
| Fibre crops | 53,280 | 78,350 | 62,120 | 68,350 | 85,090 | 111,189 | 92,550 | 88,558 | 40,650 | 62,368 | 19,200 | 19,200 | 55,616 | 26,675 |
| Fruit | 1,287,863 | 1,373,800 | 1,575,235 | 1,972,169 | 2,336,134 | 2,461,647 | 2,746,211 | 2,456,663 | 2,529,735 | 2,693,450 | 2,813,296 | 2,896,263 | 2,935,500 | 2,959,375 |
| Oilcrops | 453,200 | 487,577 | 520,005 | 447,350 | 469,306 | 342,718 | 404,352 | 349,882 | 432,528 | 561,686 | 379,011 | 605,270 | 479,350 | 836,820 |
| Pulses | 253,000 | 240,000 | 276,000 | 269,000 | 278,000 | 220,270 | 278,961 | 287,294 | 327,900 | 249,700 | 289,982 | 319,721 | 295,994 | 338,354 |
| Roots & tubers | 530,374 | 463,706 | 556,583 | 605,400 | 645,309 | 710,600 | 621,600 | 550,369 | 589,761 | 679,391 | 709,615 | 760,759 | 882,360 | 906,217 |
| Treenuts | - | - | - | - | - | - | - | - | - | - | - | - | - | - |
| Vegetables | 2,117,550 | 2,310,430 | 2,569,495 | 2,981,019 | 3,325,362 | 3,251,742 | 3,237,179 | 2,989,694 | 3,045,034 | 3,037,104 | 3,017,720 | 3,090,966 | 2,999,026 | 3,110,652 |

Swaziland

| Crop types | 2000 | 2001 | 2002 | 2003 | 2004 | 2005 | 2006 | 2007 | 2008 | 2009 | 2010 | 2011 | 2012 | 2013 |
|---|---|---|---|---|---|---|---|---|---|---|---|---|---|---|
| Cereals | 113,794 | 83,279 | 68,248 | 69,896 | 68,699 | 75,210 | 67,730 | 26,907 | 60,838 | 57,905 | 85,610 | 76,444 | 83,084 | 120,696 |
| Fibre crops | 3,700 | 3,000 | 1,900 | 600 | 1,600 | 1,560 | 480 | 360 | 350 | 370 | 590 | 590 | 558 | 558 |
| Fruit | 102,243 | 105,612 | 116,796 | 118,754 | 123,457 | 109,312 | 107,820 | 108,714 | 111,236 | 111,163 | 120,655 | 125,988 | 130,580 | 128,849 |
| Oilcrops | 2,417 | 2,190 | 1,900 | 1,425 | 1,803 | 1,785 | 1,387 | 1,016 | 1,157 | 1,214 | 1,299 | 1,006 | 1,036 | 1,046 |
| Pulses | 3,316 | 3,295 | 2,655 | 3,090 | 3,456 | 2,870 | 2,900 | 2,830 | 2,945 | 3,174 | 3,250 | 2,868 | 3,100 | 3,210 |
| Roots & tubers | 53,302 | 54,151 | 54,436 | 50,852 | 57,052 | 56,300 | 54,300 | 57,554 | 60,828 | 63,600 | 64,800 | 66,933 | 69,300 | 70,600 |
| Treenuts | 1,604 | 1,700 | 700 | 500 | 480 | 561 | 750 | 874 | 964 | 964 | 1,012 | 1,205 | 1,250 | 1,151 |
| Vegetables | 10,700 | 11,117 | 10,970 | 10,651 | 10,919 | 10,995 | 9,799 | 10,680 | 11,627 | 11,850 | 12,450 | 12,600 | 13,000 | 12,882 |

Zimbabwe

| Crop types | 2000 | 2001 | 2002 | 2003 | 2004 | 2005 | 2006 | 2007 | 2008 | 2009 | 2010 | 2011 | 2012 | 2013 |
|---|---|---|---|---|---|---|---|---|---|---|---|---|---|---|
| Cereals | 2,519,351 | 1,845,767 | 908,945 | 1,329,204 | 2,168,785 | 1,256,756 | 1,948,186 | 1,273,152 | 691,669 | 882,956 | 1,405,124 | 1,698,627 | 1,160,450 | 998,450 |
| Fibre crops | 129,630 | 130,108 | 74,623 | 86,608 | 101,695 | 76,817 | 74,150 | 82,729 | 119,660 | 81,700 | 91,995 | 92,298 | 107,500 | 97,500 |
| Fruit | 230,934 | 222,481 | 246,141 | 261,056 | 262,801 | 237,299 | 257,826 | 253,579 | 252,643 | 220,915 | 242,820 | 246,457 | 254,916 | 254,916 |
| Oilcrops | 124,633 | 131,907 | 77,779 | 90,292 | 79,221 | 54,358 | 69,200 | 96,068 | 90,028 | 72,807 | 79,336 | 77,431 | 84,370 | 69,810 |
| Pulses | 52,350 | 53,441 | 58,245 | 61,268 | 59,913 | 24,732 | 34,114 | 34,134 | 31,089 | 38,951 | 26,257 | 30,958 | 33,250 | 33,250 |
| Roots & tubers | 209,902 | 216,984 | 213,020 | 222,992 | 238,963 | 252,623 | 261,275 | 243,426 | 259,948 | 270,034 | 265,625 | 281,480 | 286,200 | 291,200 |
| Treenuts | 947 | 1,250 | 1,399 | 1,550 | 1,855 | 2,166 | 1,966 | 2,340 | 2,580 | 3,068 | 4,064 | 5,076 | 6,080 | 7,080 |
| Vegetables | 149,008 | 161,640 | 160,795 | 180,711 | 187,109 | 174,426 | 216,174 | 200,227 | 144,477 | 181,832 | 208,452 | 208,230 | 230,790 | 230,790 |

**Table 3:** Regions with highest drought severity (based on relative duration of droughts) in eastern Africa during 2010/11

| Regions with highest drought severity in eastern Africa 2010/11 | | | |
|---|---|---|---|
| **SPI-3-based** | | **VCI-based** | |
| Region | Drought severity [%] | Region | Drought severity [%] |
| Marsabit (KE) | 63.1 | Isiolo (KE) | 65.4 |
| Wajir (KE) | 63.0 | Marsabit (KE) | 63.6 |
| Isiolo (KE) | 60.7 | Shabeellaha Dhexe (SO) | 59.7 |
| Kampala (UG) | 55.3 | Samburu (KE) | 53.9 |
| Garissa (KE) | 53.8 | Shabeellaha Hoose (SO) | 53.3 |
| Nakasongola (UG) | 53.7 | Al Qadarif (SD) | 53.1 |
| Nebbi (UG) | 52.7 | Wajir (KE) | 53.0 |
| Gedo (SO) | 52.1 | Turkana (KE) | 52.1 |
| Wakiso (UG) | 49.7 | Banaadir (SO) | 51.2 |
| Hoima (UG) | 49.0 | Gash Barka (ER) | 51.0 |
| Apac (UG) | 48.8 | Al Jazirah (SD) | 48.8 |
| Tana River (KE) | 48.5 | Bay (SO) | 47.9 |
| Mandera (KE) | 47.2 | Jubbada Dhexe (SO) | 46.7 |
| Jubbada Dhexe (SO) | 47.1 | Arusha (TA) | 46.6 |
| Eastern Equatoria (SS) | 46.8 | Jubbada Hoose (SO) | 45.7 |
| Samburu (KE) | 46.7 | Afar (ET) | 45.3 |
| Bay (SO) | 46.3 | Gedo (SO) | 45.3 |
| Kitui (KE) | 45.7 | Dire Dawa (ET) | 44.0 |
| Sennar (SD) | 45.7 | Garissa (KE) | 43.9 |
| Luwero (UG) | 44.3 | Mandera (KE) | 42.1 |

**Table 4:** Regions with highest drought severity (based on relative duration of droughts) in southern Africa during 2002/03

| Regions with highest drought severity in southern Africa 2002/03 | | | |
|---|---|---|---|
| **SPI-3-based** | | **VCI-based** | |
| Region | Drought severity [%] | Region | Drought severity [%] |
| Lubombo (SZ) | 64.6 | Hardap (NA) | 90.7 |
| Shiselweni (SZ) | 59.1 | Kgalagadi (BW) | 84.0 |
| Manzini (SW) | 56.6 | Ghanzi (BW) | 79.9 |
| Hhohho (SZ) | 53.8 | Khomas (NA) | 75.3 |
| Quthing (LS) | 49.3 | Omaheke (NA) | 75.0 |
| Sowa (BW) | 44.2 | Francistown (BW) | 74.4 |
| Selibe Phikwe (BW) | 43.7 | North-West (BW) | 73.0 |
| Gauteng (ZA) | 43.0 | Sowa (BW) | 72.7 |
| North-East (BW) | 43.0 | Kweneng (BW) | 71.7 |
| Mpumalanga (ZA) | 42.2 | Northern Cape (ZA) | 69.6 |
| Limpopo (ZA) | 41.4 | Kgatleng (BW) | 69.4 |
| Hardap (NA) | 40.9 | Otjozondjupa (NA) | 68.7 |
| Khomas (NA) | 39.3 | North-East (BW) | 66.2 |
| Kgatleng (BW) | 38.5 | Omusati (NA) | 62.0 |
| Bulawayo (ZW) | 36.2 | Kunene (NA) | 61.8 |
| North-West (BW) | 35.9 | Gaborone (BW) | 61.0 |
| Francistown (BW) | 35.8 | Oshana (NA) | 59.3 |
| Northern Cape (ZA) | 33.6 | Kavango (NA) | 54.6 |
| Matabeleland South (ZW) | 33.3 | Selibe Phikwe (BW) | 54.1 |

BW = Botswana, ER = Eritrea, ET = Ethiopia, KE = Kenya, LS = Lesotho, NA = Namibia, SD = Sudan, SO = Somalia, SS = South Sudan, SZ = Swaziland, TA = Tanzania, UG = Uganda, ZA = South Africa, ZW = Zimbabwe

# Declaration of authorship

I declare that this thesis has been composed solely by myself and that it has not been submitted, in whole or in part, in any previous application for a degree.
I hereby certify that this thesis is based on my own work, unless stated otherwise. No other person's work has been used without due acknowledgement in this thesis. All references and verbatim extracts have been quoted, and all sources of information, including graphs and data sets, have been specifically acknowledged.

_____          _____

Date                             Signature